

Insight into Precipitation Polymerization of *N*-isopropylacrylamide: Reaction Mechanism, Particle Formation and Particle Structure

Von der Fakultät für Mathematik, Informatik und Naturwissenschaften der RWTH Aachen University zur Erlangung des akademischen Grades eines Doktors der Naturwissenschaften genehmigte Dissertation

vorgelegt von

Otto Lauri Johannes Virtanen, M.Sc.

aus Kuopio

Berichter: Universitätsprofessor Dr. rer. nat. Walter Richtering
Universitätsprofessor Dr. rer. nat. Sebastian Seiffert

Tag der mündlichen Prüfung: 14.11.2016

Diese Dissertation ist auf den Internetseiten der Hochschulbibliothek online verfügbar.

To Sara

Die vorliegende Arbeit wurde im Zeitraum Juli 2012 bis August 2016 am Institut für Physikalische Chemie der Rheinisch-Westfälischen Technischen Hochschule Aachen (RWTH Aachen University) angefertigt.

Versions of the following chapters have been published previously:

Chapter 3. Virtanen, O. L. J., & Richtering, W. (2014) Kinetics and particle size control in non-stirred precipitation polymerization of *N*-isopropylacrylamide. *Colloid and Polymer Science*, 292(8), 1743–1756.
<http://doi.org/10.1007/s00396-014-3208-x>

I designed the experiments with Prof. Richtering. I performed microgel synthesis, characterization and data analysis and wrote the manuscript, which was corrected, revised and edited by Prof. Richtering.

Chapter 4. Virtanen, O. L. J., Ala-Mutka, H. M., & Richtering, W. (2015) Can the Reaction Mechanism of Radical Solution Polymerization Explain the Microgel Final Particle Volume in Precipitation Polymerization of *N*-Isopropylacrylamide? *Macromolecular Chemistry and Physics*, 216(13), 1431–1440.
<http://doi.org/10.1002/macp.201500118>

I designed the experiments with Prof. Richtering. I participated in the microgel synthesis and characterization, performed the data analysis and wrote the manuscript, which was corrected, revised and edited by Prof. Richtering.

Chapter 5. Virtanen, O. L. J., Brugnoli, M., Kather, M., Pich, A., & Richtering, W. (2016) The next step in precipitation polymerization of *N*-isopropylacrylamide: Particle number density modulation by monochain globule surface charge control. *Polymer Chemistry*. <http://doi.org/DOI: 10.1039/c6py01195k>

I designed the experiments with other authors. I participated in microgel synthesis and characterization, did the data analysis, derived the Flory-Schulz expressions for chain transfer modulated radical solution polymerization and wrote the manuscript, which was corrected and revised by the other authors.

Chapter 7. Virtanen, O. L. J., Mourran, A., Pinard, P. T., & Richtering, W. (2016) Persulfate initiated ultra-low cross-linked poly (*N*-isopropylacrylamide) microgels possess an unusual inverted cross-linking structure. *Soft Matter*, 12(12), 3919–3928. <http://doi.org/10.1039/C6SM00140H>

I designed the experiments with other authors. I performed microgel synthesis and light scattering characterization, performed static light scattering data analysis and wrote the software for this purpose. I wrote the manuscript, which was corrected and revised by the other authors.

Multiple authors have contributed to the following unpublished manuscript:

Chapter 6. Virtanen, O.L.J., Meyer-Kirschner, J , Kather, M., Goetz, A., Radulescu, A., Mitsos, A., Pich, A. & Richtering W. (2016) *In situ* SANS monitoring of particle number density in precipitation polymerization of *N*-isopropylacrylamide.

I designed the experiments with other authors. I participated in neutron scattering experiments, wrote the software for automated data fitting, analyzed the results and wrote the manuscript, which was corrected and revised by the other authors.

The author has also contributed to the following publication:

Virtanen, O. L. J., Purohit, A., Brugnoli, M., Wöll, D. & Richtering, W. (2016) Synthesis and fluorescence tracking of highly uniform poly(*N*-isopropylacrylamide) microgels. *Journal of Visualized Experiments*, accepted

I designed the experiments with other authors. I participated in data analysis, writing the manuscript and coordinated the project between participating parties.

Abstract

Stimuli-sensitive microgels are soft, spherical nanoparticles composed of thermosensitive polymers, such as poly(*N*-isopropylacrylamide) (PNIPAM) and their copolymer derivatives. PNIPAM microgels are conveniently prepared by aqueous precipitation polymerization of *N*-isopropylacrylamide (NIPAM). The appeal of these particles is based on the fundamental physical aspects related to the stimuli-sensitive volume-phase transition (VPT) and interaction of the soft colloids with their surroundings, as well as specific applications enabled by the stimulus-controlled VPT behavior.

The particle formation in precipitation polymerization of thermosensitive polymers is a question of fundamental interest to colloid and polymer chemistry, although insufficiently addressed in previous work. The aim of this thesis is to recognize the important polymerization parameters that affect the particle formation, establish the polymerization mechanism in precipitation polymerization and connect the mechanism to observable particle properties such as particle volume at full conversion. All the experiments are carried out with NIPAM system.

A rapid small-scale synthesis method in conjunction with dynamic light scattering characterization is used to investigate effects of reaction conditions on PNIPAM particle volume. Other main characterization methods used are static light scattering and small-angle neutron scattering, which is used to follow the particle growth *in situ* during the polymerization. It is shown that the PNIPAM particle volume follows power laws in respect to batch monomer and initiator concentration. The power law behavior arises from charge density of PNIPAM chains generated during the particle nucleation phase early in the reaction, which determines the number density of particles in the batch. Evidence is laid out in support of the reaction likely proceeding by radical solution polymerization mechanism during the initial nucleation stage, which is the underlying factor explaining how the charge density of PNIPAM changes with reaction parameters.

In addition it is shown by static scattering analysis that commonly used peroxide initiators can have a drastic effect on the particle structure of ultra-low cross-linked microgels. These particles are shown to be hollow-like PNIPAM shells in contrast to fuzzy sphere structure commonly attributed to PNIPAM microgels. The unexpected build of the ultra-low cross-linked microgels is explained by peroxide radical induced cross-linking on the microgel surface during the reaction. Choice of initiator system and the amount of additional crosslinker therefore play a decisive role in determining the particle structure.

Kurzzusammenfassung

Bei stimuli-sensitiven Mikrogelen handelt es sich um weiche, sphärische Nanopartikel thermosensitiver Polymere, wie Poly(*N*-Isopropylacrylamid) (PNIPAM). PNIPAM Mikrogele werden in der Regel durch eine wässrige Fällungspolymerisation von *N*-isopropylacrylamide (NIPAM) hergestellt. Die Attraktivität dieser Partikel beruht auf ihren fundamentalen physikalischen Eigenschaften: dem stimuli-sensitiven Volumenphasenübergang (VPT) und der Wechselwirkung dieser weichen Kolloide mit ihrer Umgebung. Darüber hinaus machen bestimmte Anwendungen, die erst durch das stimuli-sensitive VPT-Verhalten ermöglicht werden, den Reiz dieser Partikel aus.

Die Partikelbildung bei der Fällungspolymerisation thermosensitiver Polymere ist von fundamentalem Interesse in der Polymer- und Kolloidchemie, wurde aber dennoch in früheren Arbeiten nur unzulänglich behandelt. In dieser Arbeit sollen die wichtigsten Polymerisationsparameter bzgl. der Partikelbildung ausgemacht und der Polymerisationsmechanismus der Fällungspolymerisation festgestellt werden, um diesen mit beobachtbaren Partikeleigenschaften (z.B. Partikelvolumen bei vollständigem Stoffumsatz) in Verbindung zu setzen.

Eine schnelle Synthesemethode in kleinem Maßstab wird verwendet, um den Einfluss verschiedener Reaktionsbedingungen auf das PNIPAM Partikelvolumen mit Hilfe dynamischer Lichtstreuung zu untersuchen. Außerdem finden statische Lichtstreuung und Kleinwinkelneutronenstreuung Anwendung, um das Partikelwachstum während der Polymerisation *in situ* zu beobachten. Die so erhaltenen Ergebnisse veranschaulichen, dass das PNIPAM Partikelvolumen hinsichtlich der Monomer- und Initiatorkonzentration einer Potenzfunktion folgt. Dieses Verhalten ist auf die Ladungsdichte von während der Keimbildungsphase gebildeten PNIPAM Ketten zurückzuführen. Die Zahl der Partikel im Reaktionsansatz wird durch diese Ladungsdichte bestimmt. Wie Ergebnisse dieser Arbeit zeigen, folgt die Reaktion während der Keimbildungsphase höchstwahrscheinlich dem Mechanismus einer Radikallösungspolymerisation, welcher bestimmend für die Änderung der PNIPAM Ladungsdichte mit Variation der Reaktionsbedingungen ist.

Darüber hinaus wird in dieser Arbeit mittels statischer Lichtstreuung gezeigt, dass allgemein verwendete Peroxidinitiatoren einen drastischen Einfluss auf die Partikelstruktur ultraniedrig vernetzter Mikrogele haben. Eine hohle PNIPAM Kugel anstelle einer sogenannten „fuzzy sphere“ Struktur, die PNIPAM Mikrogelen normalerweise zugeschrieben wird, scheint für diese Partikel vorzuliegen. Dieser unerwartete Aufbau der ultraniedrig vernetzten Mikrogele kann durch die Peroxidinduzierte Vernetzung der Mikrogeleoberfläche während der Reaktion erklärt werden. Die Wahl des Initiatorsystemes, sowie die Menge an zusätzlichem Vernetzer haben somit einen maßgeblichen Einfluss auf die Partikelstruktur.

Contents

1	Overview of precipitation polymerization	1
2	Methods	7
2.1	Orientation to static scattering	7
2.2	Dynamic light scattering	10
3	Polymerization kinetics by 3D-DLS	16
3.1	Abstract	16
3.2	Introduction	16
3.3	State of the art in precipitation polymerization	17
3.4	Experimental	19
3.5	Results and Discussion	21
3.6	Conclusions	31
3.7	Supporting Information	33
4	Reaction mechanism and particle volume	39
4.1	Abstract	39
4.2	Introduction	39
4.3	Experimental	42
4.4	Results & Discussion	44
4.5	Conclusions	56
4.6	Supporting information	57
5	The next step in precipitation polymerization	62
5.1	Abstract	62
5.2	Introduction	62
5.3	Experimental	65
5.4	Results and Discussion	67
5.5	Conclusions	78

CONTENTS

5.6	Supporting information	80
6	Particle concentration by <i>in situ</i> SANS	109
6.1	Abstract	109
6.2	Introduction	109
6.3	Model expression for the scattered intensity	110
6.4	Experimental	112
6.5	Results and Discussion	113
6.6	Conclusion	121
7	Structure of ULC microgels	125
7.1	Abstract	125
7.2	Introduction	126
7.3	Model expression for scattered light intensity	127
7.4	Experimental	131
7.5	Results and Discussion	134
7.6	Conclusions	144
7.7	Supporting Information	145
8	Conclusions and outlook	160
A	Symbols and abbreviations	165
B	Program FitIt!	167
B.1	General description	167
B.2	Program structure	169
B.3	Form factors relevant to microgels	169

1. Overview of precipitation polymerization

Certain polymers phase separate from homogeneous binary mixture of solvent and polymer when the temperature of the system increases beyond a certain threshold. This property is known as lower critical solution temperature (LCST) behavior and it has its origins in the temperature dependent interaction energy between the components of the binary polymer-solvent system.^[1] The phase behavior of such thermosensitive polymers is typically found to depend on the molecular weight and volume fraction of the polymer in the solution.^[2]

Radical solution polymerization of monomers that yield thermosensitive polymers above the phase separation temperature of the polymer is referred to as precipitation polymerization process. In such systems monomer and initiator are soluble in the continuous phase but the product phase separates, or precipitates, during the reaction. Archetypal thermosensitive polymer capable of undergoing controlled precipitation polymerization in aqueous solution is poly(*N*-isopropylacrylamide),^[2,3] the process first described by Chibante and Pelton.^[4] Under appropriate reaction conditions the precipitation does not lead to macroscopic aggregates but well-stabilized spherical polymer particles of narrow size distribution, in size range of tens of nanometers to some micrometers. Examples of other thermosensitive polymers capable of producing well-defined colloidal particles include poly(*N*-isopropylmethacrylamide)^[5] and poly(*N*-vinylcaprolactam).^[6]

Aqueous precipitation polymerization enables preparation of thermosensitive colloids stable over a large temperature range given that the gel point in the particles is exceeded during the reaction. In the case particles are insufficiently crosslinked, they dissolve to the continuous phase when the temperature is lowered below LCST, where the polymer is again water soluble. Gelation of the particles is usually achieved either by transfer reactions^[7] or by addition of multifunctional monomer.^[4] The basic properties of these soft colloids, so-called microgels, have been addressed in reviews.^[8,9] The most well-known of their charac-

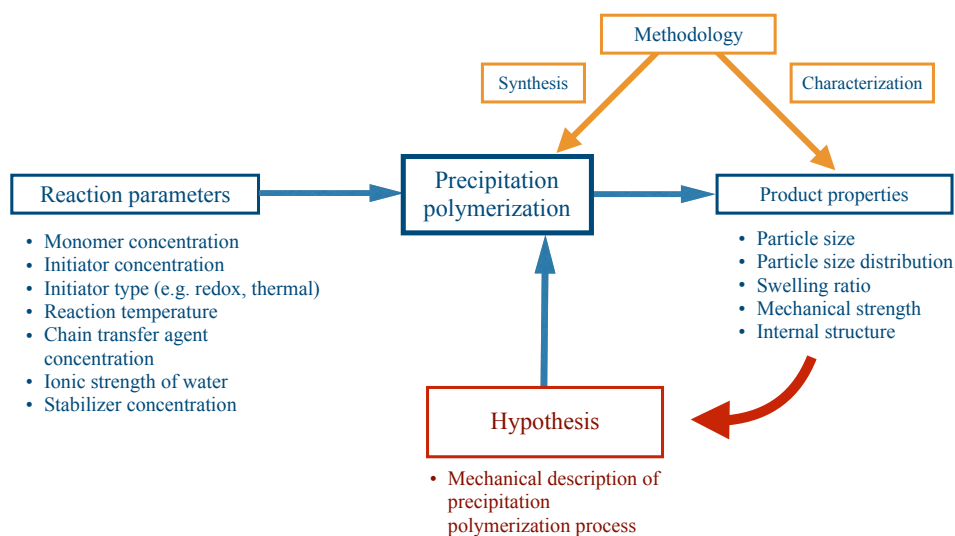


Figure 1.1: The experimental approach to understanding particle formation in precipitation polymerization of *N*-isopropylacrylamide. Systematic variation of reaction parameters is expected to lead reproducible, systematic response in product properties. Collection of sufficient amount of high quality data requires a fast and robust synthesis procedure and a reliable characterization methods that can keep up with rapid particle production. Product properties are used to deduce the underlying mechanism in precipitation process; the hypothesis is elaborated with further experiments and can be used to make informed decisions to specifically tailor particle synthesis for a given application.

teristics is the LCST related volume phase transition temperature (VPTT), which has earned the microgel particles a classification as stimuli-sensitive or "smart" materials. Consequently, microgels have been employed in various applications, such as loading and release of guest molecules,^[10,11,12] controlled emulsion stabilization,^[13,14] temperature sensitive coatings,^[15,16,17] cell culture substrates,^[18] bio-sensors^[19,20,21] and bio-catalysis^[22] as well as in fundamental research on properties of soft colloids.^[23,24,25]

Emphasis on the applications of stimuli-sensitive PNIPAM microgels might explain why research on the fundamentals of precipitation polymerization has been limited in the past 30 years.^[4] Early work started from the assumption of compartmentalized polymerization,^[26,5] but later it was recognized that particles likely form by precipitation of the thermosensitive polymer on itself.^[8,27] Even though it has been known that the particles are stabilized by charges^[26,28,29] and typical polymerization parameters such as monomer and initiator concentration should affect the amount of charged initiator fragments in the particles,^[7,30] the connection between particle size and polymerization mechanism was not comprehensively addressed in mid-2012 when the current investigation began.

Figure 1.1 gives a visual overview of experimental approach to investigation of the mechanism of precipitation polymerization. The approach towards this complex problem can be divided broadly into two complementary aspects: First, one needs a comprehensive, high quality dataset on the effects of polymerization conditions on the particle size. This is not easily achieved by the conventional batch polymerization used in the original work on PNIPAM microgel synthesis and properties,^[4,29,28,26] as polymerization of hundreds of batches under different reaction conditions would be unfeasible time-wise. The challenge is overcome by small-scale non-stirred test tube batch synthesis.^[31] This method yields particles of narrow size distribution, enables roughly an order of magnitude higher throughput in comparison to conventional batch synthesis and is highly reproducible. The non-stirred polymerization is combined with dynamic light scattering characterization of particles in collapsed state to obtain information about the effect of reaction conditions on the mass and number of the particles in the reactor during the synthesis.

Second, the experimental work has to be guided by a hypothesis on the inner workings of the precipitation polymerization process. Given the abundant solubility of *N*-isopropylacrylamide (NIPAM) and initiator to water, the notion of non-compartmentalized polymerization, i.e., radical solution polymerization mechanism for the reaction has been adopted in this work. Kinetic measurements in Chapter 3 "Kinetics of precipitation polymerization" and in Chapter 5 "The next step in precipitation polymerization" show that the power law exponents of polymerization rate in respect to NIPAM and initiator concentration support this hypothesis. The high throughput polymerization and characterization process plays

an important part in discovery of scaling law dependency of particle volume on total monomer and initiator concentration, introduced in Chapter 4 "Final particle volume in precipitation polymerization of *N*-isopropylacrylamide." The scaling laws are connected to radical solution polymerization mechanism in Chapter 5, where it is shown that experimentally observed particle volume can be explained by the number of stabilizing initiator fragments in the particles, which in turn is regulated by polymerization kinetics. Many assumptions and deduced aspects of the reaction are empirically supported by the *in situ* PNIPAM particle growth monitoring by small-angle neutron scattering, described in Chapter 6.

A further aspect in precipitation polymerization of NIPAM is the cross-linking density and distribution inside the gel particles. The amount of multifunctional comonomer affects the swelling ratio of microgels^[28] as well as the amount non-attached polymer, the sol fraction.^[5] In typical preparations the cross-links are concentrated in the core of particles^[32] due to higher reactivity of the most common crosslinker *N,N'*-methylenebisacrylamide (BIS) in comparison to NI-PAM.^[26] Less well understood cross-linking mechanism is persulfate initiator induced transfer reactions,^[28,7] which has been lately used in synthesis of ultra-low cross-linked highly deformable microgels.^[33] Chapter 7 "Structure of ultra-low cross-linked microgels" shows that persulfate radicals induce cross-links primarily on the periphery of the particles, resulting in hollow-like structures after removal of the sol fraction.

In summary, the current work presents an arc of experimental work carried out over four years on the fundamentals of precipitation polymerization of *N*-isopropylacrylamide. The main results encompass the discovery of power law behavior of PNIPAM particle volume, explanation of the particle volume by the radical solution polymerization mechanism and discovery of unexpected cross-linking structure of cross-linker free, persulfate initiated PNIPAM microgels. A prerequisite for these discoveries was the development of a rapid small-scale synthesis method, which enables highly reproducible polymerization with an order of magnitude higher throughput in comparison to traditional batch polymerization process. Throughout the investigation *N*-isopropylacrylamide has emerged as remarkably well-behaving model system, which serves to enlighten the particle formation in precipitation polymerization of thermosensitive polymers in general.

Bibliography

- [1] M. Rubinstein and R. H. Colby, *Polymer Physics*, Oxford University Press, 2003.
- [2] A. Halperin, M. Kröger and F. M. Winnik, *Angew. Chem.*, 2015, **127**, 15558–15586.
- [3] H. G. Schild, *Progress in Polymer Science*, 1992, **17**, 163–249.
- [4] R. H. Pelton and P. Chibante, *Colloids and Surfaces*, 1986, **20**, 247–256.
- [5] D. Duracher, A. Elaissari and C. Pichot, *Journal of Polymer Science Part A Polymer Chemistry*, 1999, **37**, 1823–1837.
- [6] M. Eisele and W. Burchard, *Die Makromolekulare Chemie*, 1990, **191**, 169–184.
- [7] J. Gao and B. J. Frisken, *Langmuir*, 2003, **19**, 5212–5216.
- [8] R. Pelton, *Advances in Colloid and Interface Science*, 2000, **85**, 1–33.
- [9] A. Pich and W. Richtering, *Advances in Polymer Science*, 2010, **234**, 1–37.
- [10] T. Hoare and R. H. Pelton, *Macromolecules*, 2004, **37**, 2544–2550.
- [11] S. Berger, H. Zhang and A. Pich, *Adv. Funct. Mater.*, 2009, **19**, 554–559.
- [12] T. Kureha, T. Sato and D. Suzuki, *Langmuir*, 2014, **30**, 8717–8725.
- [13] W. Richtering, *Langmuir*, 2012, **28**, 17218–17229.
- [14] S. Wiese, A. C. Spiess and W. Richtering, *Angew. Chem. Int. Ed.*, 2012, **52**, 576–579.
- [15] S. Schmidt, H. Motschmann, T. Hellweg and R. von Klitzing, *Polymer*, 2008, **49**, 749–756.
- [16] S. Schmidt, M. Zeiser, T. Hellweg, C. Duschl, A. Fery and H. Möhwald, *Adv. Funct. Mater.*, 2010, **20**, 3235–3243.
- [17] A. Burmistrova, R. Steitz and R. von Klitzing, *Chemphyschem*, 2010, **11**, 3571–3579.
- [18] Y. Xia, X. He, M. Cao, C. Chen, H. Xu, F. Pan and J. R. Lu, *Biomacromolecules*, 2013, **14**, 3615–3625.

- [19] J. P. Hervás Pérez, M. Sánchez-Paniagua López, E. López-Cabarcos and B. López-Ruiz, *Biosensors and Bioelectronics*, 2006, **22**, 429–439.
- [20] L. V. Sigolaeva, S. Y. Gladyr, A. P. H. Gelissen, O. Mergel, D. V. Pergushov, I. N. Kurochkin, F. A. Plamper and W. Richtering, *Biomacromolecules*, 2014, **15**, 3735–3745.
- [21] L. V. Sigolaeva, O. Mergel, E. G. Evtushenko, S. Y. Gladyr, A. P. H. Gelissen, D. V. Pergushov, I. N. Kurochkin, F. A. Plamper and W. Richtering, *Langmuir*, 2015, **31**, 13029–13039.
- [22] O. Kudina, A. Zakharchenko, O. Trotsenko, A. Tokarev, L. Ionov, G. Stoychev, N. Puretskiy, S. W. Pryor, A. Voronov and S. Minko, *Angew. Chem. Int. Ed.*, 2013, **53**, 483–487.
- [23] P. J. Yunker, K. Chen, M. D. Gratale, M. A. Lohr, T. Still and A. G. Yodh, *Rep. Prog. Phys.*, 2014, **77**, 056601–29.
- [24] M. A. Lohr, T. Still, R. Ganti, M. D. Gratale, Z. S. Davidson, K. B. Aptowicz, C. P. Goodrich, D. M. Sussman and A. G. Yodh, *Phys. Rev. E*, 2014, **90**, 062305–7.
- [25] R. Dreyfus, Y. Xu, T. Still, L. A. Hough, A. G. Yodh and S. Torquato, *Phys. Rev. E*, 2015, **91**, 012302–12.
- [26] X. Wu, R. H. Pelton, A. E. Hamielec, D. R. Woods and W. McPhee, *Colloid and Polymer Science*, 1994, **272**, 467–477.
- [27] K. Chan, R. Pelton and J. Zhang, *Langmuir*, 1999, **15**, 4018–4020.
- [28] W. McPhee, K. C. Tam and R. Pelton, *Journal of Colloid and Interface Science*, 1993, **156**, 24–30.
- [29] R. H. Pelton, H. M. Pelton, A. Morphesis and R. L. Rowell, *Langmuir*, 1989, **5**, 816–818.
- [30] J. Gao and B. J. Frisken, *Langmuir*, 2005, **21**, 545–551.
- [31] O. L. J. Virtanen and W. Richtering, *Colloid and Polymer Science*, 2014, **292**, 1743–1756.
- [32] M. Stieger, J. S. Pedersen, W. Richtering and P. Lindner, *Journal of Chemical Physics*, 2004, **120**, 6197–6206.
- [33] H. Bachman, A. C. Brown, K. C. Clarke, K. S. Dhada, A. Douglas, C. E. Hansen, E. Herman, J. S. Hyatt, P. Kodlekere, Z. Meng, S. Saxena, M. W. Spears Jr, N. Welsch and L. A. Lyon, *Soft Matter*, 2015, **11**, 2018–2028.

2. Methods

2.1 Orientation to static scattering

A scattering experiment is a diffraction experiment that provides information on the geometry and structure of colloidal particles in dispersion. A good elementary introduction to scattering is provided by Colby and Rubinstein.^[1] In depth introductions to scattering experiments relevant to colloid and polymer science are provided by Pusey, Lindner and Glatter;^[2] this section aims to provide only a rudimentary introduction to the basic principle of the method. A typical scattering geometry used to investigate a dispersion of colloidal particles is depicted in Figure 2.1 A. An incident beam of radiation, described by the wave propagation vector \mathbf{k} , passes through a sample positioned at point \mathbf{O} . Incident particles (photons or neutrons) are scattered quasi-elastically from the sample and detected by a detector in the far field positioned at point \mathbf{D} . The circular detector has an area A_d and subtends a solid angle Ω at distance L from the scattering volume. The scattering angle θ is the angle between \mathbf{k} and scattered radiation wave propagation vector \mathbf{k}_s ; the scattering vector \mathbf{q} is defined as the difference of the two vectors $\mathbf{k} - \mathbf{k}_s$ and has the magnitude

$$q = |\mathbf{q}| = \frac{4\pi n_0}{\lambda_0} \sin\left(\frac{\theta}{2}\right) \quad (2.1)$$

where n_0 is the refractive index of the dispersion of particles and λ_0 the wavelength of the incident beam in vacuum. Vector \mathbf{q} has the property

$$\mathbf{q} \cdot \mathbf{R} = \varphi \quad (2.2)$$

That is, the inner product of \mathbf{q} with a distance vector \mathbf{R} between any two scattering centers in the scattering volume V_{sc} yields the phase shift φ of the two waves scattered from these centers when they arrive at the detector position \mathbf{D} (Figure 2.1 B). As the scattered intensity measured by the detector is proportional

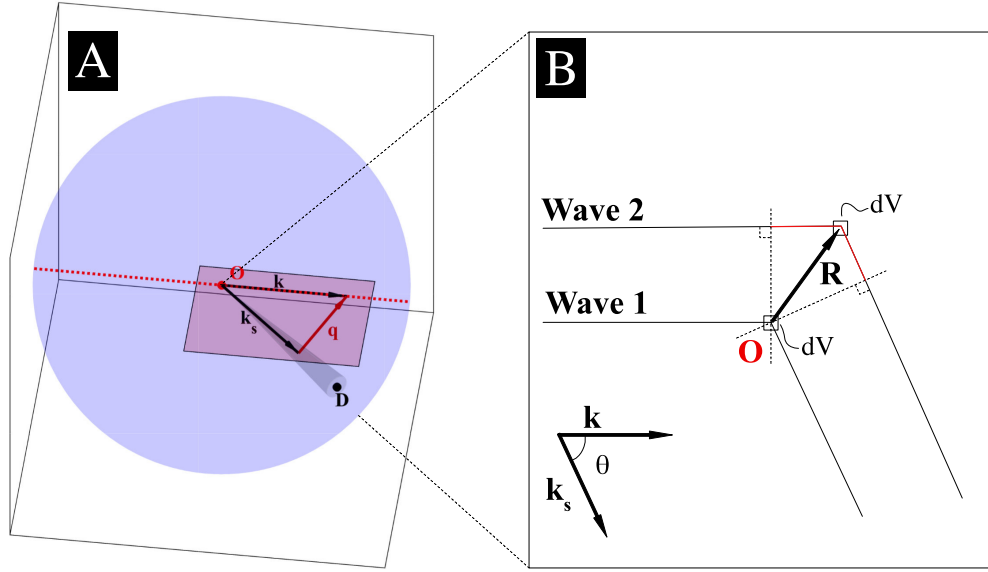


Figure 2.1: **A:** A typical geometry in a static scattering experiment. Vector \mathbf{k} denotes the propagation vector of the incident beam (red dashed line), vector \mathbf{k}_s the propagation vector of scattered light towards circular detector positioned at point \mathbf{D} , and \mathbf{q} the scattering vector. Red plane denotes the scattering plane, in which the detector is positioned. The incident beam is typically polarised perpendicular to the scattering plane. The blue sphere denotes the full solid angle. **B:** Wave 2 scattered from volume element at position \mathbf{R} travels additional distance (red) in comparison to Wave 1, which is scattered from volume element at the origin, resulting in phase shift $\mathbf{q} \cdot \mathbf{R} = \varphi$ between the waves when they arrive at the detector \mathbf{D} . The scattering angle is denoted by θ .

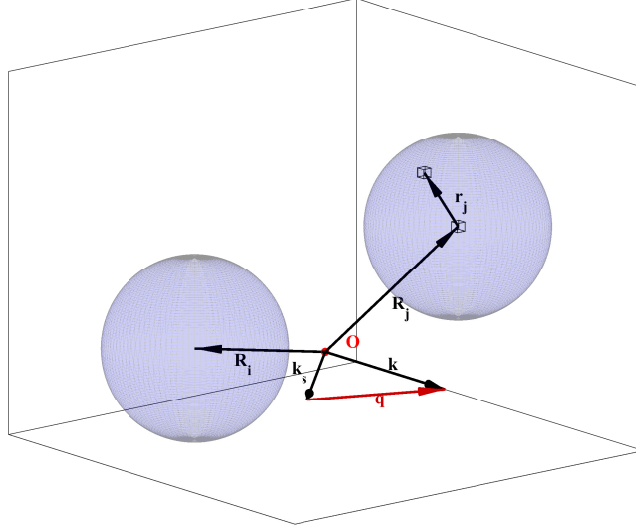


Figure 2.2: Two identical spherical particles in the scattering volume at positions \mathbf{R}_i and \mathbf{R}_j . Vector \mathbf{r}_j denotes the volume elements inside the particle j .

to the square of the magnitude of the electric field, $I(q) \propto |\mathbf{E}(q)|^2$, the specific distribution of material in the scattering volume results in a characteristic interference pattern and explains why the scattered intensity generally varies with the scattering angle. Having measured this angle dependent pattern, one then hopes to solve the inverse problem, i.e, deduce the structures that created the specific interference pattern. This is the basic proposition of a diffraction experiment.

For a dispersion of monodisperse colloidal particles, the scattered intensity in absolute units, or the differential scattering cross section of a sample per unit sample volume

$$\frac{1}{V_{sc}} \frac{d\sigma}{d\Omega}(q) = I(q) = \rho_p \Delta\rho^2 V^2 S(q) P(q) \quad (2.3)$$

has the units cm^{-1} and gives the sample specific probability that a particle from the incident beam is scattered towards point \mathbf{D} from a unit sample volume. The number density of particles is denoted by ρ_p , the scattering contrast between solvent and particles by $\Delta\rho$, scattering weight of the particles by V , structure factor by $S(q)$ and form factor by $P(q)$. Integrating Eq. 2.3 over full solid angle results in scattering cross section per unit sample volume σ/V_{sc} , the probability that a particle from the incident beam is scattered anywhere on the blue sphere in Figure 2.1 A.

Figure 2.2 depicts two identical spherical particles in the scattering volume at positions \mathbf{R}_i and \mathbf{R}_j . If the dispersion is dilute and the interactions between the

particles are weak, the phase differences due to random diffusion of the particles change randomly with time and average out in a static measurement, which measures the average scattered intensity. That is

$$\langle \mathbf{q} \cdot (\mathbf{R}_i - \mathbf{R}_j) \rangle = 0 \quad (2.4)$$

Above, brackets denote time average. Under these circumstances the contribution of correlated particle positions to the scattered intensity vanishes, i.e. $S(q) \rightarrow 1$. What remains is the interference pattern due to distribution of material inside the particle, known as the form factor

$$\frac{I(q)}{I(0)} \equiv P(q) = \left[\frac{\int_{V_j} \Delta\rho(\mathbf{r}_j) \exp(-i\mathbf{q} \cdot \mathbf{r}_j) dV_j}{\int_{V_j} \Delta\rho(\mathbf{r}_j) dV_j} \right]^2 \quad (2.5)$$

The last term of Eq. 2.5 applies only to a dilute dispersion of weakly interacting, identical, spherically symmetric particles. Other geometries need to be averaged over all possible orientations, which they can adopt in dispersion. Here dV_j is the volume element at \mathbf{r}_j and the integration runs over the volume of the particle. As the particles are identical, and $P(q)$ is a normalized quantity, it suffices to consider only one particle. Complex exponential notation is used to describe the phase term of a wave emanating from the scattering center \mathbf{r}_j . Power of two arises from the fact that intensity is measured, which is proportional to the square of the amplitude of the wave.

$P(q)$ provides one possible starting point for evaluation of the geometry, size and structure of colloidal particles. Analytical solutions exist for certain geometries.^[3] For a more general approach, see Glatter on indirect inverse Fourier transformation^[4] and deconvolution techniques.^[5,6] Further necessary aspects of scattering experiments are elaborated in subsequent chapters; Chapters 3 and 6 describe how particle size distribution can be accounted for in Eq. 2.3 and Chapter 7 shows how the internal particle structure can be deduced from $P(q)$ by regularized inversion techniques.

2.2 Dynamic light scattering^a

Comprehensive descriptions of dynamic light scattering (DLS) theory are available in the literature, e.g. by Pusey^[2] and Berne and Pecora.^[9] The basic proposition is that Brownian motion (or any other motion) of a collection of particles in dispersion can be tracked by rapidly sampling the signal scattered by the particles.

^aThis section has been recompiled and modified from supporting information published previously.^[7,8]

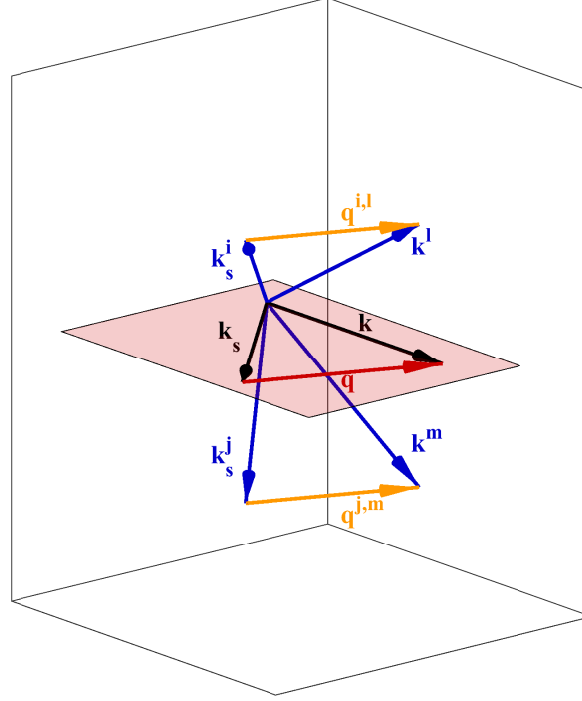


Figure 2.3: Scattering vector arrangements for a typical planar dynamic light scattering experiment (red plane) and 3D cross-correlation experiment. Vectors \mathbf{k} denote the propagation vectors of the incident beams, vectors \mathbf{k}_s the propagation vectors of scattered light (detector positions), and \mathbf{q} the scattering vectors. Superscripts refer to two different incident beams and detectors used in a 3D experiment, see Eq. 2.6 for details.

In static light scattering the scattered signal is integrated over a period of time so that the phase terms due to instantaneous particles positions average out (Eq. 2.4); in a dynamic experiment one is specifically interested in this contribution.

In other words, the scattered fields emitted by the particles interfere, and movement of the particles causes the interference pattern at the detector to (rapidly) change with time, which can be measured as fluctuating scattered intensity signal. The signal, or signals in a 3D experiment, can be then analyzed mathematically by auto or cross-correlation, respectively; the decay rate of the correlation function is related to the diffusion speed of the particles in the dispersion.

Multiple tau correlation algorithms^[10] employed for numerical computation of intensity correlation function are typically implemented in hardware. The normalized intensity correlation function measured in a dynamic light scattering experiment is defined as^[11]

$$g_{i,j}^{(2)}(q, \tau) = \frac{\langle I_i^l(q, \tau_0) I_j^m(q, \tau) \rangle}{\langle I_i^l(q) \rangle \langle I_j^m(q) \rangle} \quad (2.6)$$

where i, j denote the two detectors and l, m the two intersecting laser beams in 3D configuration, q is the modulus of the scattering vector and τ the lag time with reference point τ_0 . For autocorrelation experiment $i = j$ and $l = m$; for 3D cross-correlation experiment $i \neq j$ and $l \neq m$. Brackets denote time averaging. 3D-DLS configuration is depicted in Figure 2.3 along with a typical planar scattering geometry for reference.

Schätzel^[11] has shown that the electric field 3D cross-correlation and autocorrelation functions are similar in respect to the single-scattering contributions but higher order scattering is greatly suppressed in the 3D cross-correlation experiment. The difference in the correlation functions of single scattered photons in auto and cross-correlation experiment lies in the maximum amplitude factor β , which is theoretically 1 for autocorrelation and 1/4 for 3D cross-correlation. The decreased maximum amplitude in 3D-cross-correlation experiment is due to the fact that both detectors can register photons scattered from both intersecting beams and therefore contribute to the baseline of the cross-correlation function. In turbid samples, where multiple scattering becomes significant, autocorrelation approach fails but cross-correlation scheme produces accurate results. 3D cross-correlation approach has been employed in particle growth rate measurements presented in Chapter 3, which also contains an example comparing 3D cross-correlation and normal autocorrelation experiment for turbid samples.

The intensity auto or cross-correlation functions are converted to electric field autocorrelation functions using the Siegert relation

$$\sqrt{\beta} g_{ij}^{(1)}(q, \tau) = \sqrt{g_{ij}^{(2)}(q, \tau) - 1} \quad (2.7)$$

where β is the amplitude parameter, which depends on the alignment and correlation scheme, and $g^{(1)}$ is the electric field auto or cross-correlation function, depending on the experimental setup.

The electric field correlation function $g^{(1)}$ at any given scattering vector magnitude q (or angle) is a linear combination of exponentials, where each particle size fraction contributes one exponential weighted by the scattering weight, the form factor and number of particles in that particle size fraction^[12]

$$g^{(1)} = \int_0^\infty dD P(D) \exp(-Dq^2 \tau) \quad (2.8)$$

Above, $P(D)$ is the intensity weighted distribution function of diffusion coefficients D and τ the lag time of the correlation function. Because the intensity weighting ($P(D)$) changes with q (or angle) due to the nature of the scattering

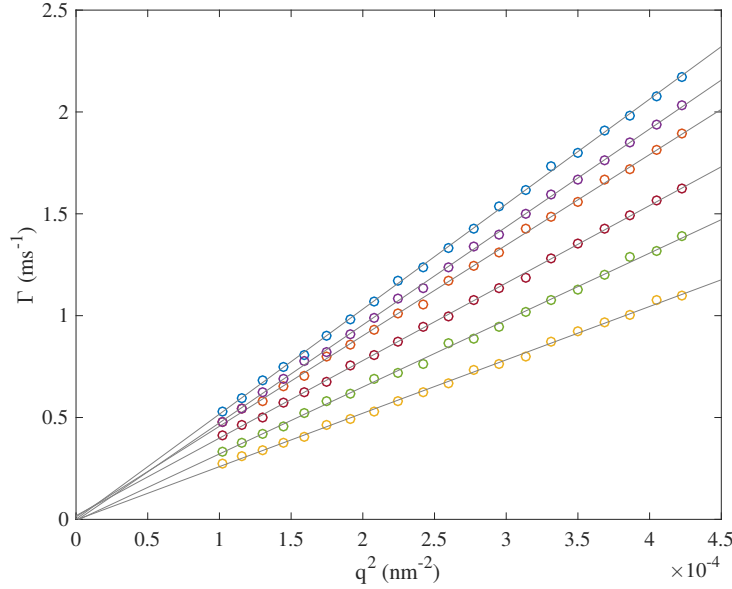


Figure 2.4: Decay rate from second order cumulant fit Γ with q^2 for six microgel batches of different size. Solid lines are linear fits to the data.

process, one can obtain severely biased results if the dynamic light scattering experiment is performed only at one angle. Real world problems arise, e.g., if one measures in a form factor minimum of particles that have dimensions comparable to the wavelength of the laser.

There are two primary methods to analyze the translational diffusion of particles. First, noting that Eq. 2.8 is Laplace transform of the intensity weighted diffusion coefficient distribution function, one can attempt a regularized inverse Laplace transformation to obtain an estimate of $P(D)$.^[13,14,15] The inversion is however an ill-conditioned problem^[16] and can lead to misleading results if the basics of numerical inversion are not understood.

Alternatively, in the case the particle size distribution is monomodal and not overtly broad, one can expand $g^{(1)}$ in terms of cumulants

$$\ln g^{(1)} = \ln \sqrt{\beta} - \Gamma \tau + \frac{\mu_2}{2} \tau^2 - \frac{\mu_3}{6} \tau^3 + \dots \quad (2.9)$$

where Γ is the intensity-weighted average decay rate of the exponential, and μ_2 and μ_3 are expansion factors. The mean diffusion coefficient is obtained from the relationship

$$\Gamma = \bar{D} q^2 \quad (2.10)$$

where the decay rate obtained from the second order cumulant fit is typically

used. This is the preferred approach throughout this work. Typical experimental data from six well behaving samples is shown in Figure 2.4. The average hydrodynamic radius of the particles can be calculated from the diffusion coefficient using the Stokes-Einstein equation

$$R_h = \frac{k_B T}{6\pi\eta\overline{D}} \quad (2.11)$$

where k_B is the Boltzmann constant, T the measurement temperature and η the viscosity of the dispersion. The standard deviation of the hydrodynamic radius can be estimated by propagating the estimated standard deviation from the linear regression (Eq. 2.10) by Gaussian error propagation.

Bibliography

- [1] M. Rubinstein and R. H. Colby, *Polymer Physics*, Oxford University Press, 2003.
- [2] *Neutrons, X-rays and Light: Scattering Methods Applied to Soft Condensed Matter*, ed. P. Lindner and T. Zemb, Amsterdam: North Holland Delta Series, 2002.
- [3] J. S. Pedersen, *Advances in Colloid and Interface Science*, 1997, **70**, 171–210.
- [4] O. Glatter, *J Appl Crystallogr*, 1977, **10**, 415–421.
- [5] O. Glatter, *J Appl Crystallogr*, 1981, **14**, 101–108.
- [6] O. Glatter and B. Hainisch, *J Appl Crystallogr*, 1984, **17**, 435–441.
- [7] O. L. J. Virtanen and W. Richtering, *Colloid and Polymer Science*, 2014, **292**, 1743–1756.
- [8] O. L. J. Virtanen, M. Brugnoni, M. Kather, A. Pich and W. Richtering, *Polymer Chemistry*, 2016.
- [9] B. J. Berne and R. Pecora, *Dynamic Light Scattering with Applications to Chemistry, Biology and Physics*, Dover Publications Inc., Mineola. New York, 2000.
- [10] M. J. Culbertson and D. L. Burden, *Rev. Sci. Instrum.*, 2007, **78**, 044102.
- [11] K. Schätzel, *Journal of Modern Optics*, 1991, **38**, 1849–1865.
- [12] P. N. Pusey, *Neutrons, X-rays and Light: Scattering Methods Applied to Soft Condensed Matter*, Amsterdam: North Holland Delta Series, 2002.
- [13] S. W. Provencher, *Computer Physics Communications*, 1982, **27**, 213–227.
- [14] S. W. Provencher, *Computer Physics Communications*, 1982, **27**, 229–242.
- [15] S. W. Provencher and P. Stepanek, *Particle & Particle Systems Characterization*, 1996, **13**, 291–294.
- [16] P. C. Hansen, *Discrete inverse problems: insight and algorithms*, Society for Industrial and Applied Mathematics, Philadelphia, 2010.

3. Polymerization kinetics by 3D-DLS

3.1 Abstract

A novel non-stirred precipitation polymerization for rapid small-scale synthesis of monodisperse temperature-sensitive poly(*N*-isopropylacrylamide) microgels is introduced. In situ 3D-DLS method is used to determine the kinetic rate law of the precipitation polymerization of *N*-isopropylacrylamide. The power law exponents for the reaction are determined to be 0.94 ± 0.08 and 0.46 ± 0.05 for the monomer and the initiator concentration, respectively. In conjunction with other evidence, it is suggested that the reaction follows conventional radical polymerization kinetics and takes place in the continuous phase. Number concentration of particles in the batch is recognized to be the determining factor for the final particle volume of the microgels.

3.2 Introduction

Microgels are spherical cross-linked polymer particles in the approximate diameter range of hundred nanometers to few microns. Since the first report of these particles, prepared by precipitation polymerization by Pelton and Chibante^[1], the focus in the stimuli-sensitive microgel field has shifted from the basic properties of the particles to applications and sophisticated modifications. The effect of reaction conditions on the reaction kinetics and final particle properties, however, is still left only qualitatively understood. For instance, we are not aware of any group reporting an empirically verified rate law for the reaction.

The purpose of this contribution is to improve our knowledge on how the reaction conditions influence the polymerization kinetics in precipitation polymerization of *N*-isopropylacrylamide (NIPAM), which is the most researched monomer for stimuli-sensitive particles. Our motivation to understand these aspects of the microgel synthesis arises from the need to better explain the working principle of

novel synthesis approaches such as semi-batch methods^[2,3] and the temperature-programmed synthesis by Meng et al.,^[4] to upscale the reaction for possible industrial scale production and to tailor the particle properties for the numerous applications envisioned by different authors. These include, e.g., stabilizers for smart emulsions,^[5] drug delivery,^[6] biosensors,^[7] and microlenses.^[8]

3.3 State of the art in precipitation polymerization

For polymers with lower critical solution temperature (LCST) in readily accessible range, such as poly(*N*-isopropylacrylamide) (PNIPAM),^[9] a convenient synthesis method for stimuli-responsive microgels is precipitation polymerization. In this approach, the monomer dissolved in water heated over PNIPAM LCST ($\approx 34^\circ\text{C}$) is initiated by a thermal radical source.^[1] Active centers propagate until they undergo coil-to-globule transition and collapse on each other to form microgel nuclei, i.e., precursor particles. The rest of the monomer is polymerized on these nuclei to give monodisperse polymer particles. In the absence of crosslinker, such as *N,N'*-methylenebisacrylamide (BIS), in the reaction mixture, loosely self-cross-linked polymer particles are formed due to transfer reactions.^[10] In this case, when the reaction temperature is cooled below PNIPAM LCST, the large non-covalently attached fraction of the polymer detaches from the particles and dissolves in the continuous phase.

The reviews by Pelton^[11] and Pich and Richtering^[12] largely summarize the current knowledge of microgel synthesis and properties. Briefly, the PNIPAM microgels exhibit the reversible temperature responsive behavior characteristic of linear PNIPAM. In the collapsed state above the microgel volume phase transition temperature (VPTT), the particles remain stable due to electrostatic repulsion emanating from the ionic initiator fragments.^[13] The reaction in the presence of ionic stabilizer such as sodium dodecyl sulfate (SDS) results in smaller particles, presumably because of earlier stabilization of the microgel nuclei.^[14,15] The volume of the particles in the collapsed state shows a linear dependence on the monomer conversion,^[16] which implies that the number of the particles remains constant during the reaction. The same authors also showed that BIS is consumed faster than NIPAM and that the final particle size increases with the fraction of BIS in the reaction mixture. Acciari et al.^[17] have shown that transparent microgels of homogeneous cross-linker density can be prepared by feeding monomer and cross-linker solution into the reactor in a regulated way. Duracher et al.^[18] showed that for *N*-isopropylmethacrylamide, the fraction of uncross-linked polymer increases with the synthesis temperature and decreases with the increasing cross-linker fraction in the reaction mixture. Recently, Meng et al.^[4] have shown that initial low-synthesis temperature in combination with a steady temperature

ramp to the final reaction temperature can lead to increased microgel particle size. The mechanism for the temperature-programmed synthesis is, however, poorly understood.

It is necessary to separate two possibly interrelated aspects in precipitation polymerization: (1) the effect of reaction parameters on the rate of the reaction and (2) the effect of reaction parameters on the final particle volume. The reaction parameters in the precipitation polymerization typically are reaction temperature (T), total initial monomer concentration (c_{tot}), initiator concentration (c_I), cross-linker fraction (x_B), and the ionic strength of water (I). If one assumes that (a) the polymer network in the collapsed state (the case during the reaction) has uniform density, (b) the particles are monodisperse, and that (c) all the monomer is polymerized on a given number of nuclei, the average final particle volume then reflects the microgel number density under given reaction conditions. This idea is sketched in Eq. 3.1

$$\langle V_{MG} \rangle = \frac{V_{M,N} + x_B \Delta V_M}{\rho_p(c_{tot}, c_I, x_B, T, I)} \cdot c_{tot} \quad (3.1)$$

Here, $\langle V_{MG} \rangle$ is the average particle volume in the collapsed state, $V_{M,N}$ is the molar volume of polymer N in the collapsed state polymerized from $(1 - x_B)c_{tot}$ monomers, ΔV_M is the difference between the molar volumes that the cross-linker and the main constituent occupy in the collapsed particle, and ρ_p is the number density of microgels (see Supporting information for details). Given that the mean particle volume can be measured by dynamic light scattering and total initial monomer concentration in the batch is known, plotting Eq. 3.1 should provide an idea how the particle number density changes with reaction parameters. The validity of the assumptions made here is discussed later.

It is a fair assumption that the mechanism of the reaction and final particle volume are interrelated, e.g., through the accumulation rate of the stabilizing initiator fragments into the network in the early stages of the reaction. Several features for this sort of heterogeneous polymerization reaction can be expected. Given that the monomer is abundantly soluble in water, propagation can take place in the continuous phase and follow radical polymerization kinetics.^[19] In this case, the reaction rate, defined as the consumption rate of the monomer, would be proportional to monomer and initiator concentration in accordance to $R \propto [M][I]^{1/2}$. Another viable possibility is that the locus of polymerization is in or on the polymer particles as in emulsion polymerization,^[20] leading to the reaction rate being dependent on the number of particles and the local monomer concentration $R \propto \rho_p [M]_p$.

Given that precipitation polymerization is a heterogeneous polymerization, useful analogues can be found in previous work. Typically, the rate laws differ clearly from that of radical solution polymerization, e.g., in the case of acrylonitrile in bulk $R \propto [I]^{0.75-0.82}$ ^[21], α -fluoroacrylamide in dimethyl sulfoxide $R \propto$

$[M]^{1.1}[I]^{0.95}$ [22] or N-methylmethacrylamide in benzene $R \propto [M]^{1-2}[I]^{0.63-0.68}$ [23]. In the latter two cases, it was demonstrated by electron spin resonance spectroscopy (ESR) that long-lived radicals accumulated in the system during the reaction, apparently due to hindered termination between collapsed macroradicals. This sort of hindered termination could also take place in precipitation polymerization of NIPAM. Balancing factor is the fact that collapsed PNIPAM is known to contain significant amount of water^[24,25], which is expected to increase the mobility of the PNIPAM chains in comparison to dry globules which many polymers form in non-solvents.

From these considerations, one would expect the power law dependence of polymerization rate on monomer and initiator concentration to be a good first indicator for the reaction mechanism of precipitation polymerization of NIPAM and a starting point for further analysis. The experimental part of this article is laid out as follows: We shall first proceed to discuss the polydispersity and homogeneity of our particles in order to validate assumptions made in regard to Eq. 3.1, and subsequently investigate the rate law of the polymerization to gain insight into the polymerization mechanism. The dependence of final particle volume on the reaction conditions is addressed in detail in Chapter 4.

3.4 Experimental

3.4.1 Reagents

All reagents are available commercially. *N*-isopropylacrylamide (NIPAM) was purchased from Acros Organics and recrystallized from *n*-hexane. *N,N'*-methylenebisacrylamide (BIS) and potassium persulfate (KPS) were acquired from AppliChem GmbH and Acros Organics, respectively, and used as received. The reaction was carried out in bidistilled MilliQ water with conductivity of 0.9 $\mu\text{S}/\text{cm}$.

3.4.2 Non-stirred microgel synthesis

A typical master solution was prepared by dissolving 0.5169 g (4.568 mmol) of NIPAM (monomer) and 0.294 g (0.1088 mmol) of KPS (initiator) in 35 ml of water. If cross-linker (BIS) was used, the amount was calculated so that the desired mole fraction was achieved and the overall monomer concentration (NIPAM+BIS) stayed constant at 0.1305 mol dm^{-3} . The master was diluted with water to the desired concentration; 1 ml was filtered through 0.2 μm filter to a 10 mm diameter glass test tube and sealed with rubber septum. The tubes were purged with nitrogen for 30 min through the septum to remove oxygen and then immersed in an oil bath equilibrated to the desired reaction temperature. Two setups were used:

An ordinary oil bath and stirring plate, where the temperature oscillated approximately $\pm 2^\circ\text{C}$ around the nominal temperature, and an oil-filled double walled glass vessel connected to a Julabo refrigerated circulator capable of keeping the temperature in the oil bath stable to $\pm 0.1^\circ\text{C}$. In the latter case, custom-made platform accommodating six reactor tubes was used to transport tubes in and out of the vessel. The reactors were typically let to stay in the bath overnight (minimum 15 h), after which full conversion was assumed and transferred immediately to an oven at 70°C in order to prevent dissolution of the polymer to the continuous phase at temperatures below the VPTT of PNIPAM.

3.4.3 Light scattering characterization

For static light scattering experiments, highly diluted dispersions were prepared to prevent multiple scattering. Samples were not filtered. Measurements were performed on a sealed construction laser goniometer apparatus FICA using a laser light source of 633 nm (SLS-Systemtechnik GmbH). The average scattered intensity $I_s(q)$, where q is the magnitude of the scattering vector, was measured from 15° to 145° with 1° steps at 20 or 50°C . To obtain quantitative information about polymer particles, the average scattered intensity traces were fitted with the microgel model by Stieger et al.^[25]

$$I_s(q) = \rho_p \Delta\rho^2 \int_0^\infty D(R, \langle R \rangle, \sigma) V_p(R)^2 P(q, r) dR + I_{BG} \quad (3.2)$$

Here, ρ_p is the number density of particles, $\Delta\rho$ is the difference of the scattering length density between polymer and solvent, $D(R, \langle R \rangle, \sigma)$ is a Gaussian distribution of radii R with mean $\langle R \rangle$ and standard deviation, σ , $V_p(R)$ is the volume of polymer within a particle, and I_{BG} is the background scattering. The form factor is given by

$$P(q, R) = \left[\frac{3(\sin qR - qR \cos qR)}{(qR)^3} \exp\left(-\frac{\sigma_s q^2}{2}\right) \right]^2 \quad (3.3)$$

where σ_s is a parameter describing the gradual decay of the particle density due to decreasing cross-linking density towards the periphery of the particle. Equation 3.3 does not include the structure factor $S(q)$, as we measure highly diluted samples, and the network fluctuation term $I_{fluct}(q)$ because the length scales at which this contribution is significant is beyond the q range of our instrument.

An LS instruments AG supplied goniometer in 3D-configuration with the laser wavelength of 633 nm was used for all the dynamic measurements. The two detectors were coupled to a 4 channel ALV 7004 hardware correlator to enable simultaneous recording of auto- and cross-correlation data. For our instrument, the

correlogram intercept term β is approximately 0.95 for autocorrelation and 0.11 for 3D-crosscorrelation configuration.

For the final particle size determination, the index match bath was equilibrated at 50 °C. The polymer particles were not allowed to cool down below the PNIPAM VPTT between synthesis and characterization; hot-filtered water was used to prepare dilutions from the reaction mixture to prevent multiple scattering. Typically, 20 points per sample were acquired throughout the available q range. All correlogram analyses were performed in a custom MATLAB program. The cumulant fit was performed on the electric field autocorrelation function from 1 μ s lag time to the point where the amplitude had decayed to 20 % of the experimental maximum. The diffusion coefficient was obtained from the slope of the decay rate of the field correlation function vs. lag time plot.^[26] The 95 % confidence bounds were determined by assuming normal distribution for the error and, thus, multiplying the standard error of the slope by 1.96. Hydrodynamic radius (R_h) was obtained from the Stokes-Einstein relation. The hydrodynamic volume of the polymer particles was calculated by assuming the particles to be hard spheres with radius of R_h ; standard error was propagated from that of the R_h determination.

For kinetic measurements, the scattering angle was arbitrarily chosen to be 90° and 3D scheme was employed. A degassed sample was inserted into the index match bath equilibrated at desired reaction temperature, and the measurement was immediately started. Acquisition times of 90 s to 180 s were used for the experiments. The electric field cross-correlation functions were fitted from 0.1 μ s onwards. Shorter lag times could be used because detector afterpulsing is not a problem in cross-correlation between two detectors. To compensate for the poor statistics due to the lower number of single-scattered photons in turbid samples, the fit range of the cumulant fit was shortened. The fit on the cross-correlation functions was limited between the maximum amplitude of the correlation function and the point where the amplitude had decayed to 60 % of the maximum. This approach leads to the loss of information on polydispersity to the apparent diffusion coefficient. We have shown, however, by static light scattering that the non-stirred reaction produces highly monodisperse particles. For each point, the apparent diffusion coefficient D_a was obtained from the second order decay rate $\bar{\Gamma}_2 = D_a q^2$ and the hydrodynamic radius and volume as described above.

3.5 Results and Discussion

3.5.1 Monodisperse particles without stirring

In situ kinetic measurements by dynamic light scattering do not allow the reaction mixture to be agitated during the acquisition. Several 1 ml batches of varying total

Table 3.1: Form factor fit parameters for microgel batches in Figures 3.1, Supporting Figure 3.7, and Supporting Figure 3.8

Figure	$T(^{\circ}\text{C})$	$[\text{M}]$ (mM)	x_B	R (nm)	σ
3.1	50 ± 2	66	0.050	377	0.086
3.1	50 ± 2	44	0.050	347	0.073
3.1	50 ± 2	33	0.050	305	0.071
3.1	50 ± 2	33	0.050	299	0.049
3.1	50 ± 2	16	0.050	261	0.061
3.1	50 ± 2	11	0.050	234	0.039
S3.7	50 ± 2	66	0.025	368	0.066
S3.7	50 ± 2	66	0.075	400	0.050
S3.7	60 ± 2	66	0.050	267	0.065
S3.7	70 ± 2	66	0.050	257	0.052

T is the synthesis temperature, $[\text{M}]$ is the total monomer concentration, x_b is the cross-linker fraction, R is the mean radius from form factor fit, σ is the polydispersity index. Supporting figures are denoted by S.

monomer concentration and cross-linker fraction in different temperatures were synthesized to examine the effect of not stirring the reaction mixture during the synthesis.

The preferable way to examine the size polydispersity of the particles in this size range is static light scattering, as it is more sensitive towards the width of the size distribution than dynamic light scattering.^[26,27] The form factors have to be fitted with an appropriate model expression to quantify the polydispersity. We use the expression for microgels of inhomogeneous cross-link density suggested by Stieger et al.^[25] The model assumes normal distribution for the size distribution and expresses the polydispersity in terms of σ index, the standard deviation of the particle size distribution divided by its mean.

The effect of total monomer concentration, cross-linker fraction, and synthesis temperature on the form factors of the particles in swollen state and the corresponding fits are shown in Figure 3.1, Supporting Figure 3.7, and Supporting Figure 3.8, respectively. Fit results are summarized in Table 3.1. The fit quality is generally good; deviations are typically observed at high q regime where intensities of the background scattering, cylindrical lens effects and cuvette back reflection are of the same order of magnitude as the scattering from the particles.^[28] The σ values for all the preparations given in Table 3.1 are consistently smaller than 0.1, which demonstrates that the particle size distribution is narrow.^[29]

Further interpretation of data shown in Figure 3.1 (and Supporting Figure 3.7 and Supporting Figure 3.8) is complicated by the fact that the batches were let to cool down below PNIPAM VPTT after the synthesis and characterized in swollen state. As shown by Duracher et al., 5 % to 30 % of the polymer mass dissolves to the continuous phase upon cooling,^[18] which decreases the final particle size. Furthermore, the size of the particles in the swollen state is determined not only by the mass of the particles but also by the swelling ratio, which is affected by the cross-linking density and distribution. These considerations complicate the influence of reaction conditions on the final particle size, and therefore, here, we wish to focus on the fact that a monodisperse product is formed under various reaction conditions without stirring, as can be seen from the distinguished form factor minima and corresponding σ values.

The feasibility of non-stirred preparation for monodisperse particles is beneficial in two ways. First, the test tube polymerization enables rapid experimentation under various reaction conditions. Second, it allows us to exclude the effect of stirring the mixture, which is known to induce aggregation in colloidal systems.^[30] In the subsequent sections, we further simplify our system by excluding the cross-linker from the reaction mixture.

3.5.2 Particle homogeneity

Wu et al. have reported the microgel volume in the collapsed state to increase linearly with the conversion.^[16] In addition to the implication that the particle number density stays constant for most of the reaction, this result also suggests that the collapsed polymer has constant density. This notion is supported by the scaling model of linear macromolecules.^[31] In a poor solvent, the polymer molecule collapses locally to a series of thermal blobs whose size is determined by the balance of thermal energy and the excluded volume attraction. At length scales larger than the thermal blob, the attraction energy overcomes the thermal energy, and the blobs adhere together to spherical arrangement to minimize the unfavorable interaction between the globule and the bulk solvent. The radius of the globule

$$R \sim \frac{b_k^2}{|v_e|^{1/3}} N^{1/3} \quad (3.4)$$

is proportional to the Kuhn length b_k , excluded volume v_e , and cube root of number of units in the chain N . At length scales larger than the thermal blob, the volume of such a globule is therefore directly proportional to the number of units, which translates to the result of Wu et al.

Further empirical reassurance for the particle structure can be obtained from the ρ quantity^[32] defined as

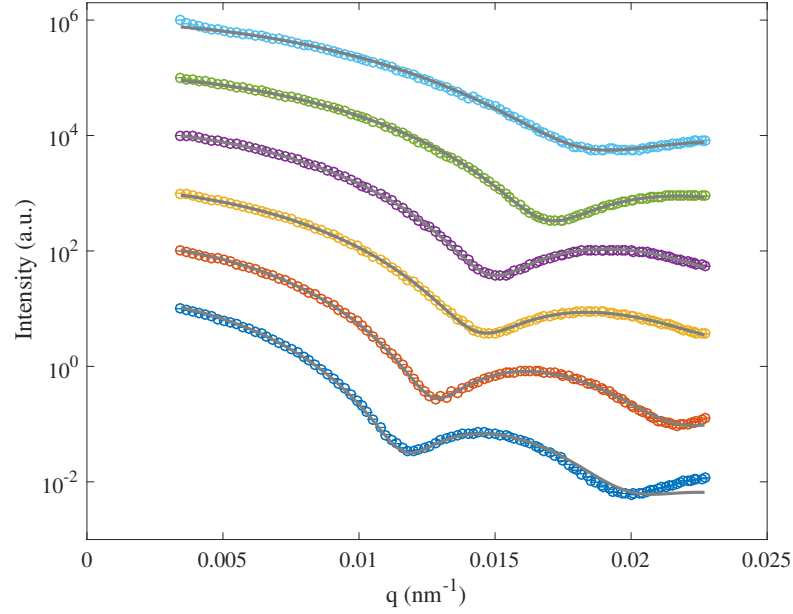


Figure 3.1: Effect of the total reagent concentration on polydispersity. Form factors of batches with $x_B = 0.050$ synthesized at 50 °C with different total monomer and initiator concentration. Measurements performed with FICA goniometer of diluted samples in swollen state at 20 °C. From top down: 11, 16, 22, 33, 44, and 66 mmol dm⁻³ NIPAM. Mole fraction of monomer to initiator is 42 in each batch. Error bars are typically in the size range of the symbols.

$$\rho = \langle R_g^2 \rangle^{1/2} / R_h \quad (3.5)$$

The parameter is sensitive for the geometry of the scatterer, as R_h reflects the outer dimensions of the geometry and radius of gyration R_g its distribution of mass. For homogeneous spheres and swollen microgel values of 0.79 and 0.35 to 0.55 are expected, respectively.^[33,34] The z-average mean-square radius of gyration can be obtained from the linear part of the low q regime using the Guinier expression and hydrodynamic radius from dynamic light scattering measurement.

Three batches without cross-linker were prepared at 50, 60, and 70 °C for the ρ determination (see Figure 3.9 for form factors). The batches were characterized at 50 °C without letting them cool down below PNIPAM VPTT between preparation and characterization to avoid the ambiguities discussed earlier. Due to the smaller dimensions of the collapsed particles, only the minimum of the largest particles synthesized at 50 °C is visible, others being beyond the q range of our instrument. The fit indicates narrow size distribution of $\sigma = 0.018$ also for this preparation. The radii of gyration, hydrodynamic radii, and the ρ parameters for

Table 3.2: Fit parameters for microgels in batches in Supporting Figure 3.9.

Figure	$T(^{\circ}\text{C})$	$[\text{M}]$ (mM)	x_B	R (nm)	σ	R_g	R_h	ρ
S3.9	50 ± 0.1	66	0	222	0.018	174	203	0.86
S3.9	60 ± 0.1	66	0	-		140	166	0.84
S3.9	70 ± 0.1	66	0	-		101	127	0.80

T is the synthesis temperature, $[\text{M}]$ is the total monomer concentration, x_B is the cross-linker fraction, R is the mean radius from form factor fit, σ is the polydispersity index, R_g is the radius of gyration, R_h is the hydrodynamic radius. Supporting figures are denoted by S.

the batches are given in Table 3.2 (see Supporting Figure 3.10 for Guinier fits). The obtained ρ values of 0.80 to 0.86 are close to the theoretical value for homogeneous sphere, as expected for collapsed polymer particles. Based on these theoretical and empirical considerations, we rest assured that the particle density can be considered constant for collapsed PNIPAM particles.

3.5.3 *In situ* kinetic measurements

Dynamic light scattering can be used to monitor the particle growth in the reactor tube during the polymerization. The reaction proceeds rapidly at conventional reagent concentrations and reaction temperatures. Results by Wu et al.^[16] indicate that the final particle size is reached in 20 min at monomer concentration of 0.12 mol dm^{-3} at 70°C which is too fast for a DLS instrument to follow. To sidestep this issue, we use approximately one order of magnitude lower concentrations and lower temperatures for the kinetic measurements on the premise that the rates of radical polymerizations typically depend on some power of the monomer and initiator concentration and exponentially on temperature. An additional problem is that the enhanced multiple scattering with increasing turbidity of the reaction mixture invalidates the assumptions the dynamic light scattering theory is based on, rendering the conventional DLS unreliable for *in situ* measurements. At the early stages of the reaction, the multiple scattering is negligible, but the challenge is to tell how long the obtained diffusion coefficients are reasonable reliable. 3D-DLS^[35] overcomes this issue by using cross-correlation between two optical paths, each defining exactly the same scattering vector, in direction and magnitude, to suppress the multiple scattering. This allows us to follow the reaction for a longer time.

The synthesis parameters for our kinetic determinations are given in Table 3.3. Figure 3.2 compares the particle volumes obtained from the autocorrelation

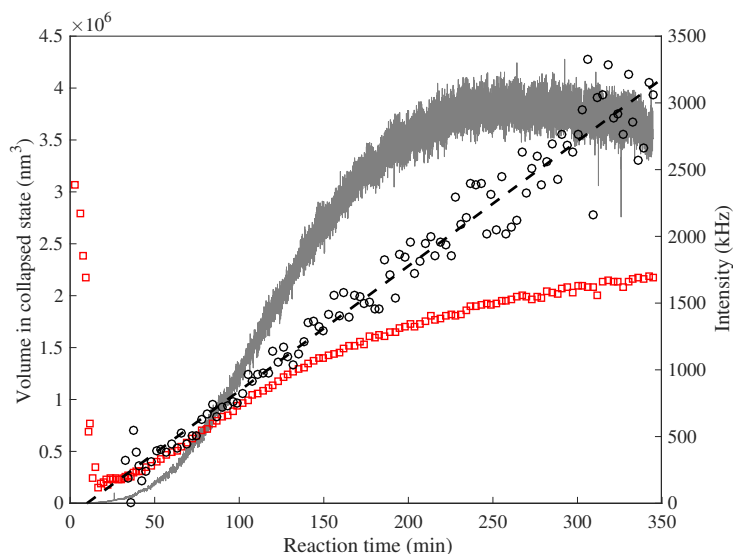


Figure 3.2: Hydrodynamic volume and scattered intensity with reaction time. Red squares and black circles denote volumes calculated from the autocorrelation and cross-correlation functions, respectively. Gray trace is the scattered intensity with time. Dashed black line is a linear fit to the cross-correlation volumes. Preparation DLS-0.0-50C-t-1 m-1/2i. Reaction temperature was 50 °C, NIPAM concentration 16 mmol dm⁻³, initiator concentration 0.19 mmol dm⁻³ and x_p 0.

to those of 3D-crosscorrelation experiment and shows the scattered intensity trace for the preparation DLS-0.0-50C-t-1 m-1/2i. The particle growth rate is greatly reduced in comparison to that of Wu et al.^[16] At early reaction times, the more sensitive autocorrelation is dominated by the background scattering of the impurities in the continuous phase, which translates to high apparent particle volumes. The scattered intensity at this stage is too low to obtain reliable crosscorrelation functions. After initiation, the scattering is dominated by the growing polymer particles due to their increasing concentration, molecular weight, and high refractive index contrast to the solvent. The limitation of the autocorrelation approach becomes evident as the apparent volumes start to deviate from those calculated from the crosscorrelation functions. At late stages of the polymerization, also the error in the crosscorrelation measurements increases substantially as the single-scattering contribution to the signal vanishes.

As seen from the cross-correlation volumes in Figure 3.2, an interesting property of the reaction is that the particle volume grows linearly with time close to the region where the final particle volume is approached. This convenience allows us to determine the particle growth rate from the linear portion of the volume trace by simple linear regression.

Table 3.3: Reaction rates and final hydrodynamic radii with initiator and monomer concentration

Batch	$[M] \times 10^2$ (mol dm ⁻³)	$[I] \times 10^4$ (mol dm ⁻³)	R_h (nm)	Error ^a (nm)	Rate (% min ⁻¹)	Error ^a (% min ⁻¹)	Intercept
DLS-0.0-50C-t-1 m-2i	1.63	7.77	118	1.4	0.43	0.04	-0.91
DLS-0.0-50C-t-1 m-3/2i	1.63	5.83	117	1.1	0.35	0.04	-1.69
DLS-0.0-50C-t-1 m-1i	1.63	3.94	114	1.3	0.29	0.03	-1.08
DLS-0.0-50C-t-1 m-1/2i	1.63	1.92	111	0.7	0.217	0.002	-2.18
DLS-0.0-50C-t-5 m-1/2i	7.77	1.92	212	4.6	-	-	-
DLS-0.0-50C-t-2 m-1/2i	3.32	1.92	148	1.2	0.46	0.04	-13.39
DLS-0.0-50C-t-3/2 m-1/2i	2.42	1.92	133	1.6	0.34	0.03	-9.48
DLS-0.0-50C-t-1 m-1/2i	1.64	1.92	111	0.7	0.217	0.007	-2.18
DLS-0.0-50C-t-3/4 m-1/2i	1.23	1.92	105	0.8	0.179	0.006	-1.30
DLS-0.0-50C-t-1 m-1/2i-SDS	1.64	1.92	49	1.1	0.21	0.02	-2.20

The first and second groups show the effect of initiator and monomer concentration on the rate, respectively. The last input shows the effect of SDS on the reaction rate.

^a95 % confidence bounds

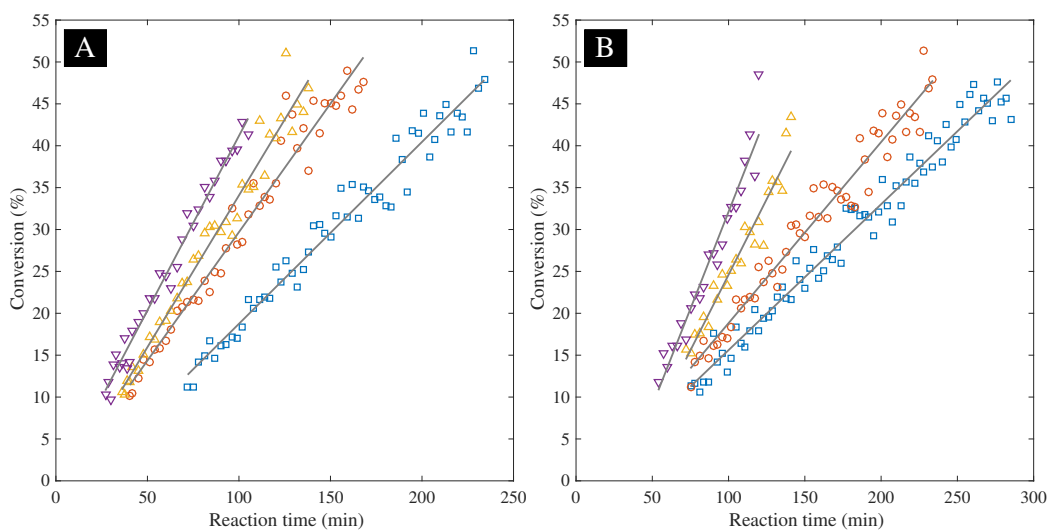


Figure 3.3: **A:** Conversion with time for different initiator concentrations. From fastest to slowest, preparations DLS-0.0-50C-t-1 m-2i, -3/2i, -1i, and -1/2i. **B:** Conversion with time for different monomer concentrations. From fastest to slowest preparations DLS-0.0-50C-t-2 m-1/2i, -3/2 m, -1 m, and -1/2 m.

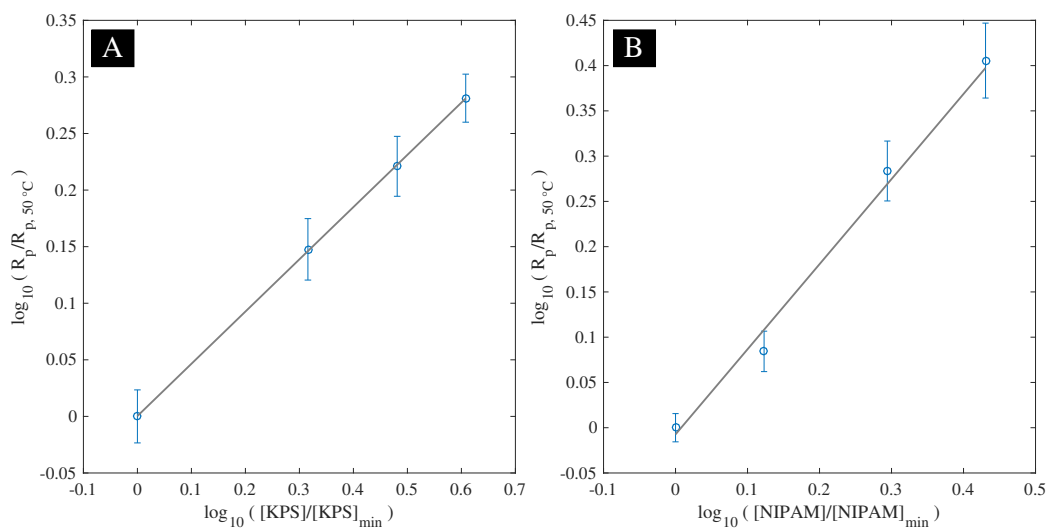


Figure 3.4: **A:** Reaction rate against the initiator concentration on log-log scale. The slope of the linear fit is 0.46 ± 0.05 . **B:** Reaction rate against the monomer concentration on log-log scale. The slope of the linear fit is 0.94 ± 0.08 . Error bars represent the 95 % confidence intervals calculated from the standard deviation of the linear fit for each point

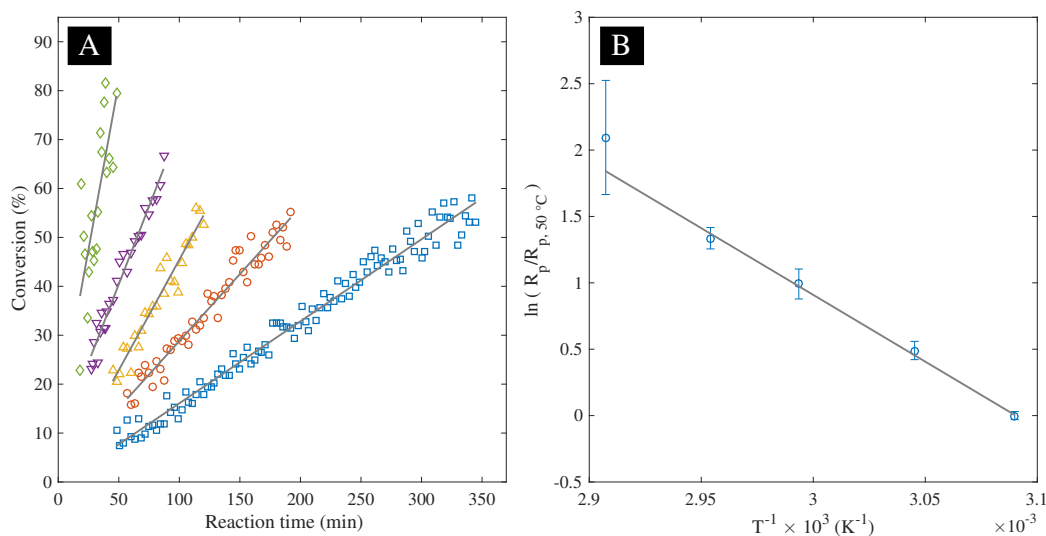


Figure 3.5: **A:** Conversion with time for various synthesis temperatures. From the fastest to slowest 71 °C, 66 °C, 61 °C, 55 °C and 50 °C. **B:** Corresponding Arrhenius plot. NIPAM concentration was $8.21 \text{ mmol dm}^{-3}$ and initiator concentration $0.19 \text{ mmol dm}^{-3}$ for each sample. No cross-linker was used.

Given that particle volume shows linear dependence to conversion,^[16] we would expect the particle growth rate to translate to monomer consumption rate. Obviously, for two preparations with the same monomer consumption rate but different particle number density, the particle growth rate is not equal. However, if we assume the final collapsed particle volume measured after the allocated reaction time to be the indicator for 100 % conversion, the intermediate volumes normalized to the final volume should translate to conversion at any given instant. Therefore, we interpret the constant particle growth rate shown in Figure 3.2 as a constant reaction rate to high conversions, an observation that has also been made for other heterogeneous polymerizations.^[21,23]

Growth traces were measured for different reagent concentrations and normalized to the final collapsed particle volume in order to investigate the monomer and initiator concentration dependence of the reaction rate. A maximum range from 10 % to 50 % conversion was chosen for fitting. Linear regression was applicable to all the preparations. The kinetic traces in Figure 3.3 immediately show that the polymerization rate is sensitive to the initiator and monomer concentrations, the reaction rate increasing with the amount of reactants (Table 3.3). The polymerization rates in logarithmic presentation with the appropriate reagent concentration reveal the power law exponent for the initiator concentration to be 0.46 ± 0.05 (Figure 3.4A) and for the monomer concentration 0.94 ± 0.08 (Figure 3.4B).

Table 3.4: Final particle size and reaction rate with temperature. Monomer and initiator concentrations were $8.21 \text{ mmol dm}^{-3}$ and $0.19 \text{ mmol dm}^{-3}$, respectively. No cross-linker.

$T(\text{K})^a$	$R_h \text{ (nm)}$	Std (nm)	Rate ($\% \text{ min}^{-1}$)	Error ($\% \text{ min}^{-1}$) ^b	Intercept
323.6	98	1.7	0.168	0.005	-0.68
328.4	84	0.4	0.27	0.02	1.43
334.1	78	0.5	0.45	0.05	0.26
338.5	71	0.5	0.64	0.05	8.52
344.0	59	1.8	1.4	0.6	13.49

^aAverage from all the measurement points for the linear fit

^b95 % confidence bounds

Uncertainties are reported as 95 % confidence intervals. These exponents are very close to the theoretical exponents of $1/2$ and 1 for the conventional radical polymerization and do not resemble other heterogeneous polymerizations discussed earlier.

The rate of homogeneous radical polymerization initiated by thermally decomposing initiator typically shows strong dependence on reaction temperature. Figure 3.5A shows the conversion traces for a constant composition batch at various temperatures. The substantial increase in the reaction rate with temperature makes the acquisition challenging for DLS measurement. Fortunately, the particle volume also decreases strongly with synthesis temperature, reducing the multiple scattering at high conversions. The fit range was therefore chosen to be the maximum accessible linear range for each reaction. Final hydrodynamic radii and reaction rates with temperature are tabulated in Table 3.4, and the respective Arrhenius plot is shown in Figure 3.5B. Solving the composite activation energy from the slope according to

$$\frac{\partial \ln R_p}{\partial T^{-1}} = -\frac{E_R}{R} \quad (3.6)$$

where E_R is the composite activation energy and R is the gas constant gives the value of $92 \pm 6 \text{ kJ mol}^{-1}$. This is close to the typical value of 88 to 90 kJ mol^{-1} for many homogeneous radical polymerizations with thermal initiator, such as many peroxides and AIBN.^[36]

The effect of the particle number density on the reaction rate was explicitly tested by adding sodium dodecyl sulfate (SDS) to the reaction mixture. SDS is expected to increase the number density of the particles due to the earlier stabilization of the particle nuclei but otherwise retain the reaction conditions the same. In the case that the propagation takes place in the polymer particles, one

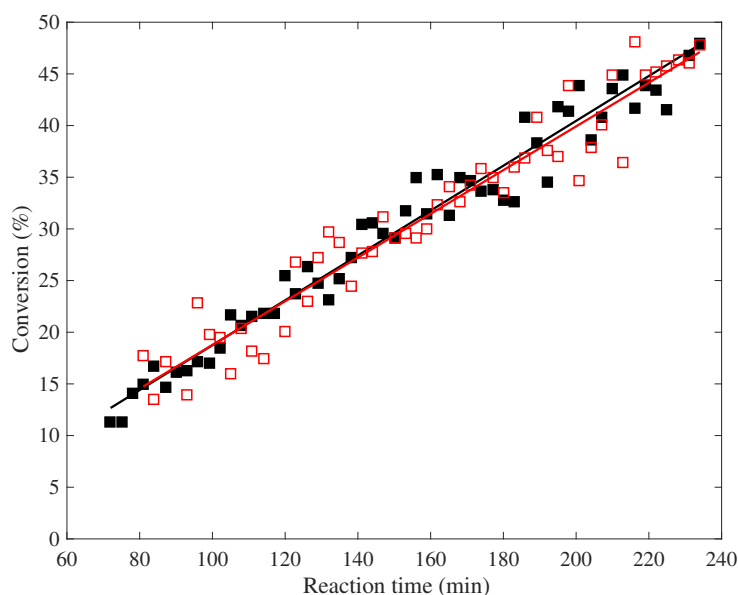


Figure 3.6: Conversion with time for the batch DLS-0.0-50C-1m-1/2i with and without SDS. Reaction temperature was 50 °C.

would then expect the rate to increase in a preparation with SDS in contrast to one without. Batch DLS-0.0-50 C-t-1 m-1/2i was synthesized with and without SDS. Despite the fact that the final particle volume is significantly reduced by SDS, indicating significantly higher number density, the fit from the 10 to 50 % conversion range gives essentially identical reaction rate (Table 3.3, Figure 3.6). The independence of the polymerization rate on the number of particles, the rate law exponents, and the typical value of composite activation energy for conventional radical polymerization supports the notion that the locus of the polymerization in precipitation polymerization of NIPAM is not in the polymer particles as in emulsion polymerization, but in the continuous phase from where the polymer globules eventually diffuse to the existing particles.

3.6 Conclusions

In this work, we have demonstrated that non-stirred precipitation polymerization is a viable method for microgel particle synthesis. In contrast to conventional batch synthesis, our approach enables rapid experimentation with different reaction conditions.

We have used a novel empirical approach to determine the kinetic rate law of the reaction in the dilute regime. Our evidence is in conflict with the original

notion of precipitation polymerization being surfactant-free emulsion polymerization. On the contrary, the results shown here suggest that the reaction takes place in the continuous phase and follows radical solution polymerization kinetics. This observation is of prime importance for the control of the reaction and further development of novel microgel synthesis methods. Whether transfer reactions or acceleration phenomena affect the reaction kinetics at higher reagent concentrations, have to be determined by other means than 3D-DLS.

3.7 Supporting Information

3.7.1 Expression for the particle concentration

PNIPAM chains are expected to collapse into dense globules of constant density above the lower critical solution temperature.^[31] If we assume that all the monomer ends up in particles we then expect to be able to polymerize total amount of collapsed polymer from the given amount of monomer in the batch

$$V_{\text{MG,tot}} = [V_{M,N}(1 - x_B) + V_{M,B}x_B] n_{\text{tot}}$$

Here $V_{\text{MG,tot}}$ is the total collapsed volume of all the microgels, $V_{M,N}$ is the molar volume of collapsed main monomer, $V_{M,B}$ is the collapsed volume of the cross-linker and x_B the fraction of the cross-linker of the total monomer amount n_{tot} . If we assume that the particles have a monomodal and narrow size distribution (so that we can determine the average particle size by DLS reliably), then the number of particles n_p is

$$\frac{V_{\text{MG,tot}}}{\langle V_{\text{MG}} \rangle} = n_p = \frac{[V_{M,N}(1 - x_B) + V_{M,B}x_B]}{\langle V_{\text{MG}} \rangle} n_{\text{tot}}$$

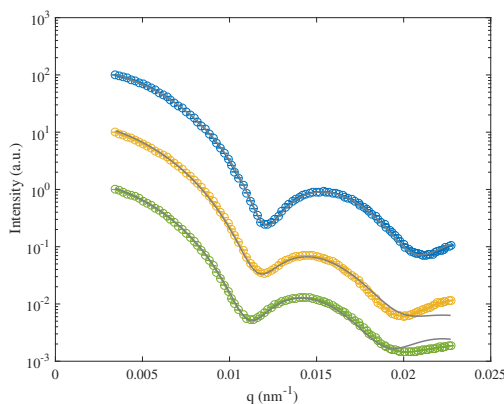
where $\langle V_{\text{MG}} \rangle$ is the mean volume of the collapsed particles. Given that we deal with dispersions, the concentration of the particles is then

$$\frac{n_p}{V} = \rho_p = \frac{[V_{M,N}(1 - x_B) + V_{M,B}x_B]}{\langle V_{\text{MG}} \rangle} c_{\text{tot}}$$

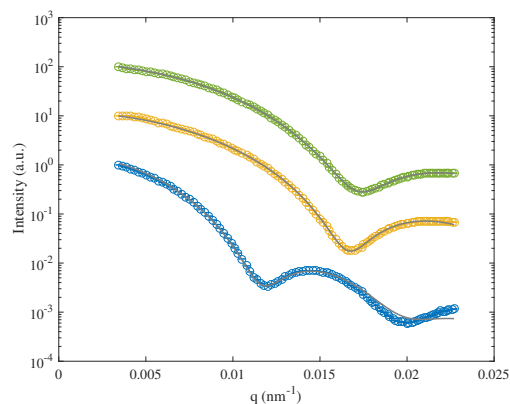
We can express the volume of cross-linker units in the polymer by their excess volume $\Delta V_M = V_{M,N} - V_{M,B}$, which gives the expression in the form of Eq. 3.7

$$\langle V_{\text{MG}} \rangle = \frac{V_{m,N} + x_B \Delta V_M}{\rho_p} \cdot c_{\text{tot}} \quad (3.7)$$

In the case we don't lose monomer in side reactions and there are no additional contributions to the volume of the collapsed particles, we would expect the number density of particles to determine the final particle volume.



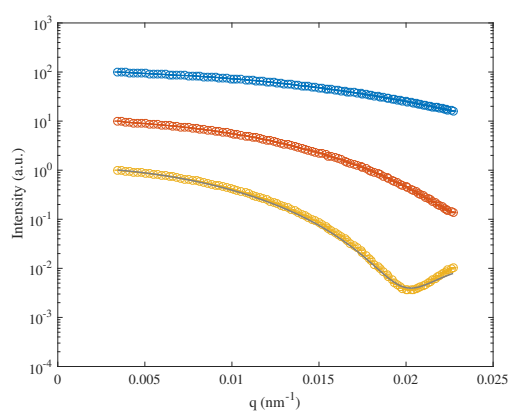
Supporting Figure 3.7: Effect of the crosslinker fraction on polydispersity. Form factors of batches with total monomer concentration of 66 mM synthesized at 50 °C. Mole fraction of monomer to initiator is 42. Characterization in swollen state at 20 °C. From top down: 2.5 mol – %, 5.0 mol – % and 7.5 mol – % crosslinker. Error bars are typically in the size range of the symbols.



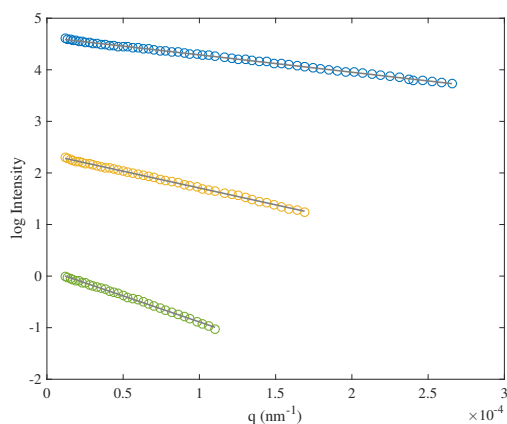
Supporting Figure 3.8: Effect of the reaction temperature on polydispersity. Form factors of batches with total monomer concentration of 66 mM, monomer to initiator mole fraction of 42 and 5.0 mol – % crosslinker. Characterization in swollen state at 20 °C. From top down synthesis temperatures of 70 °C, 60 °C and 50 °C. Error bars are typically in the size range of the symbols.

3.7.2 Particle homogeneity

Particle structure, size and size distribution were investigated by static light scattering. Supporting Figure 3.7 shows *swollen state* form factors of particles prepared with 2.5 mol – %, 5.0 mol – % and 7.5 mol – % crosslinker polymerized at 60 °C. Supporting Figure 3.8 shows *swollen state* form factors of 5.0 mol – % crosslinker particles prepared at 70 °C, 60 °C and 50 °C. Supporting Figure 3.9 shows *collapsed state* form factors of particles prepared at 70 °C, 60 °C and 50 °C. Supporting Figure 3.10 shows the Guinier fits for these batches.



Supporting Figure 3.9: Form factors of uncross-linked collapsed particles prepared at different temperatures. Total monomer concentration 66 mM, monomer to initiator mole fraction of 42. Characterization in collapsed state at 50 °C. From top down synthesis temperatures of 70 °C, 60 °C and 50 °C. Error bars are typically in the size range of the symbols.



Supporting Figure 3.10: Guinier plots of uncross-linked collapsed particles prepared at different temperatures. Total monomer concentration 66 mM, monomer to initiator mole fraction of 42. Characterization in collapsed state at 50 °C. From top down synthesis temperatures of 70 °C, 60 °C and 50 °C. Error bars are typically in the size range of the symbols.

Bibliography

- [1] R. H. Pelton and P. Chibante, *Colloids and Surfaces*, 1986, **20**, 247–256.
- [2] S. Meyer and W. Richtering, *Macromolecules*, 2005, **38**, 1517–1519.
- [3] T. Still, K. Chen, A. M. Alsayed, K. B. Aptowicz and A. G. Yodh, *Journal of Colloid and Interface Science*, 2013, **405**, 96–102.
- [4] Z. Meng, M. H. Smith and L. A. Lyon, *Colloid and Polymer Science*, 2009, **287**, 277–285.
- [5] S. Wiese, A. C. Spiess and W. Richtering, *Angew. Chem. Int. Ed.*, 2012, **52**, 576–579.
- [6] P. F. Kiser, G. Wilson and D. Needham, *J Control Release*, 2000, **68**, 9–22.
- [7] J. P. Hervás Pérez, M. Sánchez-Paniagua López, E. López-Cabarcos and B. López-Ruiz, *Biosensors and Bioelectronics*, 2006, **22**, 429–439.
- [8] M. J. Serpe, J. Kim and L. A. Lyon, *Adv. Mater.*, 2004, **16**, 184–187.
- [9] H. G. Schild, *Progress in Polymer Science*, 1992, **17**, 163–249.
- [10] J. Gao and B. J. Frisken, *Langmuir*, 2005, **21**, 545–551.
- [11] R. Pelton, *Advances in Colloid and Interface Science*, 2000, **85**, 1–33.
- [12] A. Pich and W. Richtering, *Advances in Polymer Science*, 2010, **234**, 1–37.
- [13] R. H. Pelton, H. M. Pelton, A. Morphesis and R. L. Rowell, *Langmuir*, 1989, **5**, 816–818.
- [14] W. McPhee, K. C. Tam and R. Pelton, *Journal of Colloid and Interface Science*, 1993, **156**, 24–30.
- [15] K. C. Tam, S. Ragaram and R. H. Pelton, *Langmuir*, 1994, **10**, 418–422.
- [16] X. Wu, R. H. Pelton, A. E. Hamielec, D. R. Woods and W. McPhee, *Colloid and Polymer Science*, 1994, **272**, 467–477.
- [17] R. Acciaro, T. Gilányi and I. Varga, *Langmuir*, 2011, **27**, 7917–7925.
- [18] D. Duracher, A. Elaissari and C. Pichot, *Journal of Polymer Science Part A Polymer Chemistry*, 1999, **37**, 1823–1837.
- [19] P. J. Flory, *Principles of Polymer Chemistry*, Cornell University Press, 1953.

- [20] W. V. Smith and R. H. Ewart, *The Journal of Chemical Physics*, 1948, **16**, 592–599.
- [21] W. M. Thomas and J. J. Pellon, *Journal of Polymer Science*, 1954, **13**, 329–353.
- [22] M. Ueda, S. Shouji, T. Ogata, M. Kamachi and C. U. Pittman, *Macromolecules*, 1984, **17**, 2800–2804.
- [23] T. Sato, J. Miyamoto and T. Otsu, *Journal of Polymer Science: Polymer Chemistry Edition*, 1984, **22**, 3921–3932.
- [24] R. H. Pelton, *Journal of Colloid and Interface Science*, 2010, **348**, 673–674.
- [25] M. Stieger, J. S. Pedersen, W. Richtering and P. Lindner, *Journal of Chemical Physics*, 2004, **120**, 6197–6206.
- [26] W. Burchard and W. Richtering, *Progress in Polymer and Colloid Science*, 1989, **80**, 151–163.
- [27] *Neutrons, X-rays and Light: Scattering Methods Applied to Soft Condensed Matter*, ed. P. Lindner and T. Zemb, Amsterdam: North Holland Delta Series, 2002.
- [28] J. C. Hansen, D. Maier, J. Honerkamp, W. Richtering, F. M. Horn and H. Senff, *Journal of Colloid and Interface Science*, 1999, **215**, 72–84.
- [29] P. N. Pusey, *Liquids, Freezing and Glass Transition*, Elsevier Science Publishers B.V., 1991.
- [30] D. F. Evans and H. Wennerström, *The Colloidal Domain Where Physics, Chemistry, Biology, and Technology Meet*, Wiley-VCH, 2nd edn, 1999.
- [31] M. Rubinstein and R. H. Colby, *Polymer Physics*, Oxford University Press, 2003.
- [32] W. Burchard, M. Schmidt and W. H. Stockmayer, *Macromolecules*, 1980, **13**, 1265–1272.
- [33] W. Burchard and S. Ross-Murphy, *Physical Techniques for the Study of Food Biopolymers*, Edited by SB Ross Murphy, Blackie Academic, Glasgow, 1994, vol. 151.
- [34] H. Senff and W. Richtering, *Colloid and Polymer Science*, 2000, **278**, 830–840.

- [35] K. Schätzel, *Journal of Modern Optics*, 1991, **38**, 1849–1865.
- [36] G. Odian, *Principles of Polymerization*, Wiley Interscience, 4th edn, 2004.

4. Reaction mechanism and particle volume

4.1 Abstract

Precise particle size customization is a key requirement for the applications of stimuli-sensitive poly(*N*-isopropylacrylamide) microgels. No empirically supported mechanism has been presented to explain the microgel particle size dependence on polymerization conditions. In this work non-stirred precipitation polymerization is employed to address this question. It is argued that the reaction proceeds by radical solution polymerization mechanism rather than as emulsion polymerization. The number of particles in the batch, and the microgel particle volume, is shown to correlate with the charge density of particles determined by the kinetic chain length. Cross-linking efficiency is recognized to be an important factor in the particle nucleation. Properties of radical solution polymerization, such as differences in the rate of decomposition of thermally decomposing initiator and redox initiator are used to tune the particle number density in the batch. Contemporary synthesis approaches, including temperature-programmed synthesis, are discussed in the context of these results.

4.2 Introduction

A convenient particle size and structure control are necessary to tailor poly(*N*-isopropylacrylamide)^[1] (PNIPAM) microgel particles^[2,3] for various applications.^[4,5] These include, e.g., microlenses^[6], biosensors^[7,8], biocatalysis^[9] and stabilizers for smart emulsions.^[10] In recent years several groups have introduced novel precipitation polymerization approaches to answer this challenge, including low temperature synthesis,^[11] temperature-programmed synthesis^[12] and semi-batch synthesis.^[13] These empirical approaches clearly demonstrate that microgel par-

ticle synthesis can be advanced, but also the need for thorough understanding of the particle formation mechanism in order to devise new synthesis methods. In this work we investigate the fundamental aspects of microgel particle formation in precipitation polymerization using rapid, convenient and highly reproducible non-stirred synthesis method and show that a correlation exists between the final volume of the PNIPAM particles in the collapsed state and the average degree of polymerization predicted by the solution polymerization kinetics. As already recognized by Gao and Frisken,^[14] connecting the radical polymerization mechanism with the final particle volume would be an attractive explanation for the experimentally observed microgel size. However, the experimental evidence in support of this mechanism has been non-conclusive and even conflicting^[14] until now.

The fundamental question in precipitation polymerization is what controls the particle nucleation and determines the particle concentration in the batch, and thus, the microgel final particle volume. Several authors have demonstrated that modulating the colloidal stabilization by an additional stabilizer such as sodium dodecyl sulfate (SDS)^[15,16] and cetyl trimethyl ammonium bromide (CTAB),^[17] or the ionic strength of the aqueous reaction mixture^[13] is a convenient way to control microgel final particle size. If the particle stabilization can be enhanced by additional charges, any process affecting the charge density of the particles should result in a measurable difference in the final particle volume.

The fundamental difference between precipitation polymerization of NIPAM and emulsion polymerization is the locus of polymerization. It has been shown that the reaction rate is independent of the particle number,^[18,19] which, together with the fact that NIPAM is abundantly soluble to water, strongly suggest that propagation largely takes place in the continuous phase. We have shown that the particle growth rate (and the reaction rate derived from this data) is sensitive to both the initiator and monomer concentration in the batch.^[19] Furthermore we determined the reaction rate law to be $R_p \propto [M]_0^{0,97 \pm 0,1} [I]_0^{0,46 \pm 0,01}$, where $[M]_0$ is the initial monomer concentration and $[I]_0$ the initial initiator concentration in the batch. The exponents are very close to theoretically predicted values 1 and 1/2, respectively, for radical polymerization in solution.

In precipitation polymerization the chains are initiated by charged initiator fragments,^[20] and therefore the charge density of the polymer should depend on the average chain length during the reaction predicted by the radical solution kinetics. When several of the primary globules aggregate, nuclei with certain charges-to-polymer-mass ratio, and electrostatic stabilization, are formed (Figure 4.1, left). After this initial period, the particles likely grow by adsorption of chains from the continuous phase. The adsorbed chains can in principle be in collapsed or open conformation, depending whether the critical chain length for the collapse has been exceeded. During the growth process the particles repel each other due

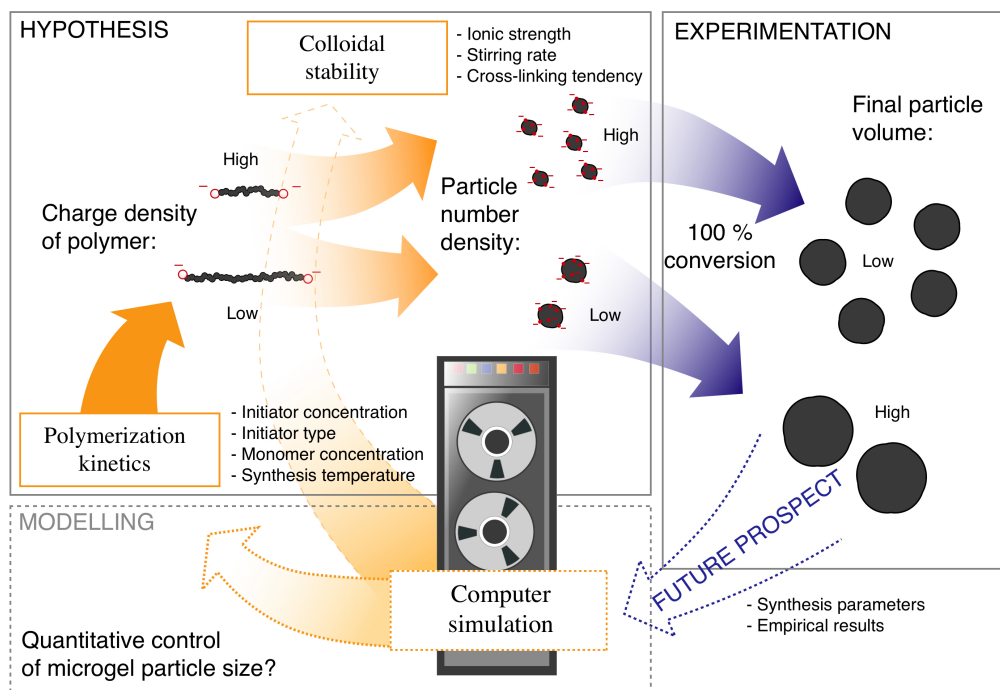


Figure 4.1: Establishing quantitative microgel final particle volume control: We assume that the final particle volume of the microgels in the collapsed state at 100 % conversion is determined by the number of particles at the end of the nucleation phase. The number of particles is assumed to be dependent on the accumulation of stabilizing initiator fragments to the polymer, which is controlled by the kinetics of radical polymerization. Thorough understanding of precipitation polymerization is necessary for the development of models, which can enable quantitative particle size control in future.

to electrostatic repulsion, thus preserving the narrow size distribution. The final particle volume therefore depends on the particle number density at the end of the nucleation phase (Figure 4.1, right).

Not all the reaction variables, such as initiator concentration, seem to lead to clearly observable trends.^[21] Gao and Frisken^[14] and we^[19] even measured a slight increase in the final particle volume of the particles with increasing potassium persulfate (KPS) initiator concentration, contrary to the expectation. The key to understand this and other unexpected results in microgel synthesis is to realize that a parameter, such as initiator concentration, may have multiple effects on the system. For instance, changing the initiator concentration changes the initiation rate, ionic strength (initiators are typically salts) and even the cross-linking tendency in the system^[22,14] likely due to peroxide cross-linking^[23] (p. 742).

Understanding the principles of microgel formation requires decoupling the

reaction parameters to a sufficient degree. Our approach in this work is to suppress the spontaneous cross-linking reactions due to the initiator in order to concentrate on the fundamentals of precipitation polymerization of *N*-isopropylacrylamide (NIPAM). We show that when the initiation rate is decoupled from cross-linking reactions, increasing the initiation rate increases the number of particles in the batch leading to lower final particle volume. Investigation into particle number dependency on synthesis temperature reveals strong dependence for thermally decomposing initiator, whereas the dependency is clearly weaker for redox initiator. To complete the parade of favorites of radical polymerization, we also show the increasing batch monomer concentration to reduce the number of particles. These empirically observed features of the precipitation polymerization support the notion that the particle number in the batch is modulated by the kinetic chain length according to the solution polymerization kinetics. In future work the proposed particle stabilization scheme can be incorporated to simulation models, which can enable quantitative particle size control in precipitation polymerization of NIPAM (Figure 4.1, bottom).

4.3 Experimental

4.3.1 Particle synthesis

NIPAM was recrystallized from n-hexane, other reactants were used as received. Typically NIPAM (Acros Organics) was weighted in a glass vessel and appropriate volume of accelerator *N,N,N',N'*-tetramethylethylenediamine (TEMED) was added if redox initiation system was used. Initiator potassium persulfate (KPS) or ammonium persulfate (APS) was weighted in another glass vessel. Filtered (0.2 μm RC membrane filter) double distilled MilliQ water was added to both vessels, which were agitated until the reactants had dissolved completely. Different concentrations of reactants were obtained by diluting to the end concentration. Initiator solutions were diluted with water, monomer - TEMED solutions were diluted with aqueous TEMED solution in order to keep the TEMED concentration constant regardless of monomer concentration. 0.5 ml of monomer solutions was transferred to 8 test tubes with 10 mm diameter, which were sealed with septa. Initiator solution was deoxygenized by purging with nitrogen and 0.5 ml was transferred to 1 ml nitrogen-washed syringes equipped with 120 mm needles. The needles were inserted to the test tubes through the septa but not immersed into the monomer solution. The monomer solutions in the test tubes were deoxygenized by nitrogen purging. The tubes were then inserted into a platform accommodating 8 tubes and immersed into an oil bath in a double-walled glass vessel connected to a Julabo refrigerated water bath. Temperature was measured in the oil bath and

when desired synthesis temperature was attained (50, 60, 70 or 80 °C), the syringes were pressed to the bottom of the test tubes and the initiator was injected into the tubes. Syringes were then removed and polymerization was let to proceed overnight. Tubes were then transferred rapidly to an oven at 60 °C in order to prevent sol fraction from redispersing from the particles at temperatures below poly(*N*-isopropylacrylamide) (PNIPAM) volume phase transition temperature (VPTT). The sol and gel fractions were not determined in this work.

4.3.2 Light scattering characterization

For dynamic light scattering characterization all instruments were preheated in order to prevent material from redispersing upon cooling below VPTT of PNIPAM. Hot filtered double distilled MilliQ water was used to dilute the reaction mixture to prevent multiple scattering. The sample cuvette was transferred hot to the toluene bath of the light scattering goniometer tempered at 50 °C.

A 3D light scattering goniometer scraped together from parts of ALV GmbH and LS-Instruments Ag goniometers was used for all dynamic measurements. ALV software and electronics as well as ALV-7004 hardware correlator was used to control the instrument and correlate the signal. Only one laser beam line ($\lambda = 632$ nm) and detection path was used to prevent simultaneous measurement at different scattering vectors. Typically 25 correlograms (minimum 90 s acquisition time) throughout the available q range per sample were obtained. For narrow monomodal size distributions the average diffusion coefficient (D) can be determined by linear regression from

$$\Gamma_2 = Dq^2 \quad (4.1)$$

where Γ_2 is decay rate of the exponential from the second order cumulant fit and q the magnitude of the scattering vector at given scattering angle. For our samples the cumulant fit was typically performed from 0.01 ms lag time until to the point where the electric field correlation function had decayed to 20% of the 0.01 ms value. Hydrodynamic radius was determined from the Stokes-Einstein relation and volume by assuming particles to be hard spheres with the hydrodynamic radius.

A closed SLS-Systemtechnik GmbH supplied goniometer with $\lambda = 658$ nm was used for form factor determination by static light scattering. Highly diluted samples were measured at 20 °C. The average scattering intensity was typically measured from 15° to 146° with 1° increments. Solvent scattering was subtracted from scattering of the samples.

4.3.3 ^1H -NMR

The ^1H -NMR spectra were measured with a 400 MHz Bruker DRX 400 NMR spectrometer at 23 °C directly from the reaction mixtures, where D_2O was used as solvent. The chemical shifts are presented in parts per million downfield from the TMS standard.

4.4 Results & Discussion

4.4.1 Particle volume in the collapsed state reflects the mass and number of particles in the batch

Collapsed polymer in a poor solvent typically forms dry globules with constant density due to thermodynamical reasons.^[24] Even though PNIPAM is known to contain significant amount of water in collapsed state,^[25] data obtained from scattering models for PNIPAM microgels indicates that the polymer volume fraction inside collapsed microgel is constant throughout the particle.^[26] Based on these considerations, final particle volume determination in the collapsed state is advantageous in the sense that the collapsed volume reflects the mass of polymer in the particles. Particle volume determination in the swollen state is complicated by factors such as non-constant particle density and swelling ratio determined by the cross-linker distribution and doesn't therefore provide an easy way to compare particle volumes of particles polymerized under different reaction conditions. We have argued,^[19] that the volume of the particles in the collapsed state reflects their number density at 100 % conversion according to

$$V_p = \frac{V_M}{\rho_p} [\text{M}]_0 \quad (4.2)$$

Here V_p is the final particle volume in the collapsed state, V_M ($\text{nm}^3 \text{mol}^{-1}$) the volume of collapsed network (including water) polymerized from 1 mol of NIPAM, ρ_p (dm^{-3}) the function describing number of particles in unit volume under given polymerization conditions and $[\text{M}]_0$ (mol dm^{-3}) the initial NIPAM concentration in the batch. It needs to be emphasized that the particles must not cool down below the VPTT at any point between the synthesis and characterization as Duracher et al. have reported that as much as 30% of the polymer (the sol fraction) can redisperse to the continuous phase upon swelling.^[21]

In summary, the final particle volume in the collapsed state provides an easily comparable quantity between different polymerization conditions. Furthermore it is an indirect measure of the particle number in the batch in accordance to Equation (4.2). These two facts make the final particle volume in the collapsed state a

convenient empirical quantity for comparing the effects of various synthesis parameters.

4.4.2 Polymerization in D₂O shows that virtually full conversion is reached within the reaction time

For the final particle volume of different batches to be comparable, full conversion has to be reached under typical polymerization conditions. The extent of the reaction was investigated by ¹H-NMR from batches prepared in heavy water. The ¹H-NMR spectra for initial NIPAM batch concentration of $8.2 \times 10^{-2} \text{ mol dm}^{-3}$ and $1.8 \times 10^{-2} \text{ mol dm}^{-3}$ after overnight polymerization are shown in Supporting Figure 4.8 and Supporting Figure 4.9. Small amount of monomer ($\approx 2\%$ based on the integrals) is present in the higher concentration batch whereas no monomer signal could be detected in the lower concentration batch. Overall this results is very satisfactory and shows that close to 100 % conversion is reached in the synthesis. The amount of unreacted monomer translates at most to few percent error in the final particle volume. All the batches polymerized in this work settle between the two monomer concentrations given above. As expected, polymerization in heavy water does not affect the final particle volume in the collapsed state (Supporting Figure 4.10).

4.4.3 KPS and APS induce spontaneous crosslinks whereas redox initiation does not

Cross-linking reactions are known to affect the particle nucleation, reducing the number particles in the batch.^[15,18] As KPS is known to induce spontaneous cross-linking,^[15,22] probably due to peroxide cross-linking reactions,^[23] (p. 742) removing this contribution is desirable when nucleation of the particles is investigated.

Gao and Frisken^[22] and later Hu et al.^[11] have shown that when the redox pair APS and TEMED is used to initiate the polymerization, particles dissolve to the continuous phase below the VPTT. This is likely due to the fact that the structure of radicals produced in the redox reaction is unsuitable for abstraction of hydrogens from the polymer chains. We have reproduced this result for the non-stirred precipitation polymerization with APS-TEMED as redox initiation system. Form factors measured in the swollen state (Supporting Figure 4.11) show that when KPS or APS alone are used as initiator in the absence of additional cross-linker, the initiator induced cross-linking creates spherical particles with narrow size distribution. In contrast when APS-TEMED redox pair is used to initiate the reaction, no form factor for a spherical particle is seen when particles are allowed to swell,

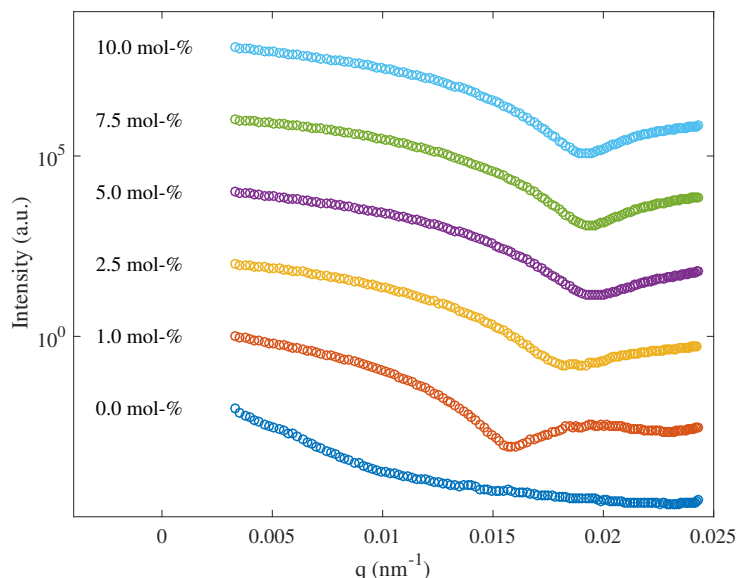


Figure 4.2: Form factors for particles with varying cross-linker fractions measured in the swollen state in water at 20 °C. APS-TEMED was used as initiator system. Distinguished minima characteristic of spherical particles with narrow size distribution are seen for all the samples containing cross-linker, whereas the sample without cross-linker redisperses. Intensities are scaled arbitrarily and do not reflect the absolute scattered intensity from each sample. Total monomer concentrations for 10 mol-% sample was $7.31 \times 10^{-2} \text{ mol dm}^{-3}$ and for the rest $8.21 \times 10^{-2} \text{ mol dm}^{-3}$.

whereas even 1 mol-% of additional cross-linker is enough to prevent to particles from completely dissolving (Figure 4.2). Our conclusion is that TEMED greatly suppresses the peroxide cross-linking typical of KPS and APS and therefore the particles polymerized without cross-linker dissolve when let to swell. We have not confirmed the morphology of the dissolved polymeric material. Some transfer reactions are still likely to take place, which will make molar mass analysis by size exclusion chromatography difficult.

4.4.4 Cross-linking affects the nucleation of the particles

The effect of the additional cross-linker was investigated by suppressing the cross-linking by the initiator using APS-TEMED redox initiation system. As seen in Figure 4.3 the final particle volume in the collapsed state increases non-linearly with the cross-linker fraction. Similar observations were made by McPhee et al.^[15] and Wu et. al.^[18] for KPS initiated PNIPAM microgels, and Duracher et al. for Poly(*N*-isopropylmethacrylamide) (PNIPMAM) microgels.^[21] The volume

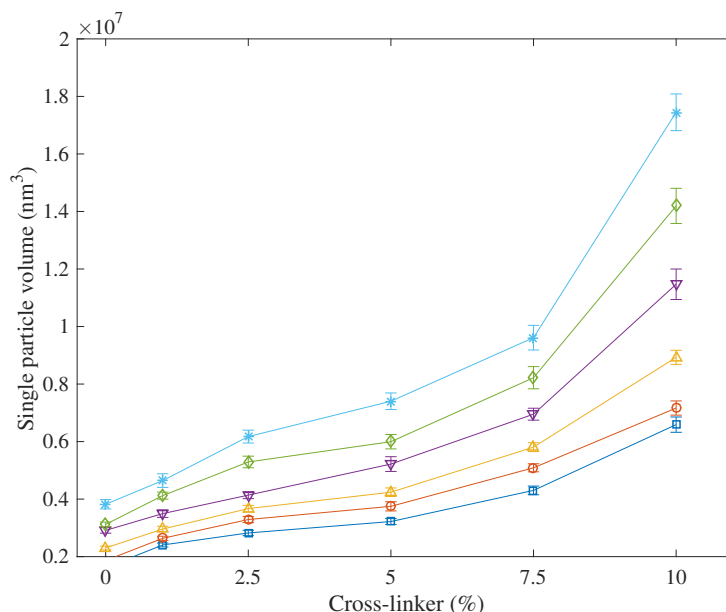


Figure 4.3: Final particle volume in the collapsed state with cross-linker fraction for various total monomer concentrations. All batches polymerized at 60 °C using APS-TEMED as initiator system. Total monomer concentrations (NIPAM + BIS) from top down: 6.40×10^{-2} , 5.49×10^{-2} , 4.58×10^{-2} , 3.67×10^{-2} , 2.76×10^{-2} and $1.83 \times 10^{-2} \text{ mol dm}^{-3}$. APS concentration $3.18 \times 10^{-3} \text{ mol dm}^{-3}$ with varying TEMED concentrations from top down: 8.38×10^{-4} , 7.19×10^{-4} , 5.99×10^{-4} , 4.80×10^{-4} , 3.61×10^{-4} and $2.42 \times 10^{-4} \text{ mol dm}^{-3}$

increase due to the total monomer concentration will be addressed in a later section.

Normalization of the collapsed volume data in Figure 4.3 to the 0 mol – % volume for each total monomer concentration (Figure S4.12) shows that the particle volume in batches with 10 mol – % cross-linker is approximately 4 times the volume of batches without cross-linker in every case. Such a large increase cannot be due to the possibly larger volume the cross-links occupy in the collapsed network. The volume increase has to be caused by the decrease of particle number density with the increasing cross-linker concentration, which shows that the cross-linker clearly affects the nucleation of the particles early in the reaction. A possible explanation for this phenomenon is that the increased probability of precursor particle aggregation decreases the number density of particles, resulting in higher final particle volume. An alternative explanation is that the additional crosslinks due to the cross-linker restrict the mobility of the bound charges and trap them in the interior of the particles. The charges contribute to colloidal stability efficiently

only at the surface, so the reduced stability could promote precursor aggregation and reduce the number density of the particles. In order to exclude complications caused by the cross-linking reactions, all further batches were synthesized without additional cross-linker.

4.4.5 In the absence of spontaneous cross-linking, final particle volume decreases with initiation rate

The long established kinetic scheme for conventional radical polymerization shows that the kinetic chain length ν is inversely proportional to the square root of the initiation rate (and also initiator concentration) $\nu \propto R_i^{-\frac{1}{2}} \propto [\text{APS}]^{-\frac{1}{2}}$.^[27,23] Therefore we expect that increasing the initiation rate shortens the average degree of polymerization, leading to higher charge density of the precursor particles and higher particle number density. The increased particle number density can be measured as smaller final particle volume in the collapsed state.

As far as we are aware the consensus in the field is that the initiator concentration does not have a strong influence on the particle size in precipitation polymerization. Pelton does not mention effect of the initiator concentration in his thorough review,^[2] Duracher et al. found no clear trend,^[21] Gao and Frisken^[14] and we^[19] in fact observed small but measurable increase in the final particle volume with increasing KPS concentration. Gao and Frisken attribute this phenomenon to the increasing ionic strength with the KPS concentration but the results shown in Figure 4.3 indicate that cross-linking reactions are also a plausible source for the volume increase. Further investigation is necessary to determine whether the increase in the final particle volume in the collapsed state is due to the cross-linking tendency per se or whether copolymerization kinetics also play a role in the particle nucleation.

The picture clearly changes when APS concentration is varied but all the other parameters are kept constant, as seen in Figure 4.4 A. The final particle volume in the collapsed state decreases with increasing APS concentration, exhibiting an asymptotic behavior towards higher initiator concentration. This leveling off of the final particle size beyond a rather small threshold might explain why the final particle size is typically reported to be independent of the initiator concentration. Figure 4.4 A shows the good reproducibility between the repeated series in the range of 1 - 2.5 mM APS. We attribute the minuscule differences to uncertainties in reaction composition and reaction temperature, which was difficult to adjust to closer than ± 0.4 K of each other between the series. Larger deviations can be seen in the very low APS concentrations below 1.0 mM APS. At these very low initiator concentrations initiation failed occasionally and the system appears to be very sensitive to perturbations.

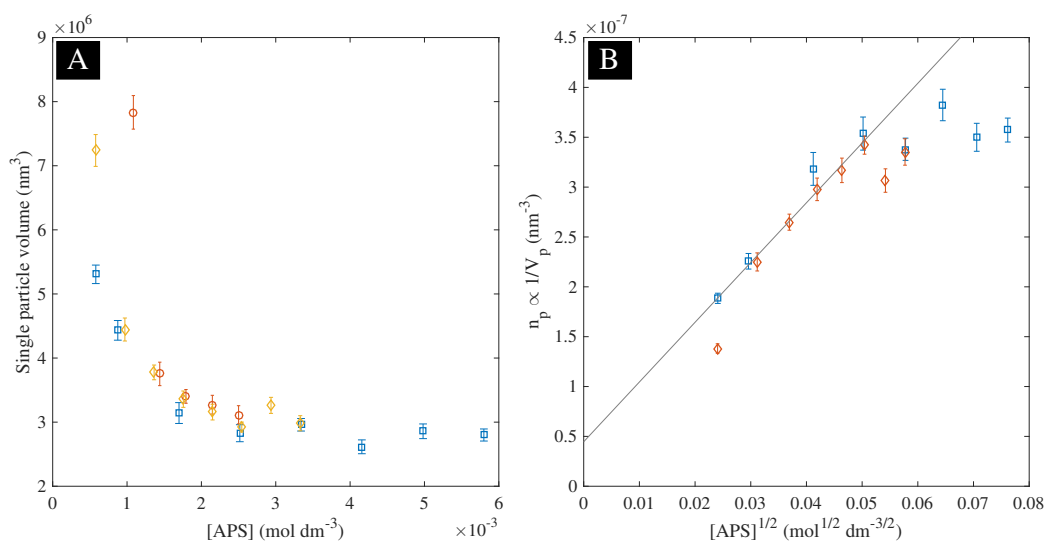


Figure 4.4: A: Final single particle volume in the collapsed state vs. APS concentration. Different symbols denote repeated polymerization series. **B:** Inverse particle volume vs. the square root of APS concentration. The line indicates linearization in the intermediate region, suggesting that the number of particles is proportional to the average charge density of the polymer. Polymerization at 60 °C, NIPAM and TEMED concentrations were held constant at 5.29×10^{-2} and 1.72×10^{-3} mol dm⁻³, respectively. The error bars denote the 95 % confidence interval from the light scattering measurement, not repetitions of the synthesis.

The charge density of the polymer is proportional to the inverse kinetic chain length or the square root of the initiator concentration $1/\nu \propto [\text{APS}]^{1/2}$. Figure 4.4 B shows the inverse final particle volume, which is proportional to the number density of particles according to Equation (4.2), against the charge density of the polymer. In the range between 1 - 2.5 mM APS the measurement points reside well on the line. This linearization suggest a dependence of the number of particles on the charge density of the polymer. Admittedly the range where we can see this dependency is rather limited but also broadening the initiator concentration range is not straightforward: At very low initiator concentrations our methodology would need to be improved (mainly in terms of the precision of the reactant composition and reaction temperature; and tedious repetitions) due to sensitivity of the system to perturbations. At high initiator concentrations this is likely a futile attempt as the increasing ionic strength arising from the initiator screens charges and destabilizes particles leading to the opposite effect to that of higher the initiation rate.

In principle, a similar concentration dependence should be observed when the

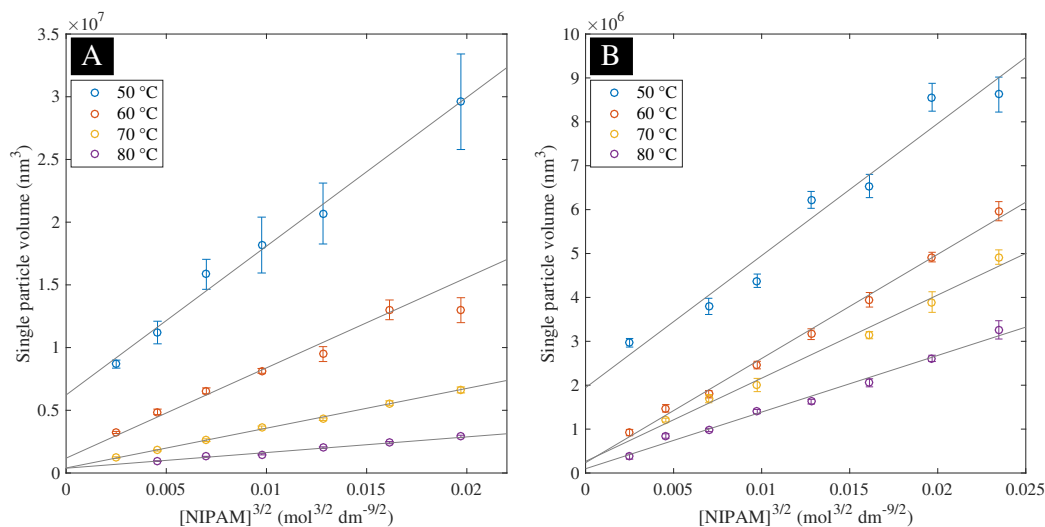


Figure 4.5: The final particle volume in the collapsed state against $3/2$ power of the monomer concentration at constant initiator concentration in each batch. **A:** KPS initiation, KPS concentration 1.56 mol dm^{-3} ; **B:** APS-TEMED initiation, APS and TEMED concentrations 1.56×10^{-3} and 1.71 mol dm^{-3} , respectively. Synthesis temperatures are given in the insets in each graph. The lines are linear fits to the data points. The error bars denote the 95 % confidence interval from the light scattering measurement, not repetitions of the synthesis.

concentration of the other redox component is varied, namely TEMED. However, we were unable to reproduce this effect for TEMED, instead the final particle volume increased drastically after certain threshold of TEMED concentration. This might be due to the fact that many amines act as a chain transfer agent^[23] (p. 246). In a forthcoming publication we will report on our finding that addition of chain transfer agent to the reaction mixture drastically increases the final particle volume in the collapsed state.

4.4.6 Final particle volume is less sensitive to synthesis temperature in the case of redox initiation

In solution polymerization the average degree of polymerization is proportional to the polymerization temperature according to

$$v \propto \frac{k_p}{(k_d k_t)^{1/2}} \propto \exp\left(-\frac{E_{\bar{X}}}{RT}\right) \quad (4.3)$$

Here k_p , k_d and k_t are the rate coefficients of propagation, initiator dissociation

Table 4.1: Fit parameters for linear fits for the final particle volume in the collapsed state with 3/2 power of monomer concentration shown in Figure 4.5. Upper section shows values for KPS initiated batches and lower section for APS-TEMED initiated batches. The slope and intercept terms are denoted by k and V_0 , respectively.

T °C	k $\text{dm}^{15/2} \text{mol}^{-3/2}$	Error $\text{dm}^{15/2} \text{mol}^{-3/2}$	V_0 dm^3	Error dm^3
50	1.29×10^{-15}	0.08×10^{-15}	5.5×10^{-18}	0.3×10^{-18}
60	6.9×10^{-16}	0.3×10^{-16}	1.5×10^{-18}	0.2×10^{-18}
70	3.14×10^{-16}	0.07×10^{-16}	4.1×10^{-19}	0.6×10^{-19}
80	1.25×10^{-16}	0.05×10^{-16}	3.9×10^{-19}	0.4×10^{-19}
50	2.9×10^{-16}	0.3×10^{-17}	2.1×10^{-18}	0.3×10^{-18}
60	2.31×10^{-16}	0.07×10^{-18}	3.0×10^{-19}	0.7×10^{-19}
70	1.79×10^{-16}	0.08×10^{-18}	3.8×10^{-19}	0.8×10^{-19}
80	1.22×10^{-16}	0.07×10^{-18}	1.6×10^{-19}	0.7×10^{-19}

and termination, respectively. $E_{\bar{X}} = E_p - (E_d/2) - (E_t/2)$ is the composite activation energy for the average degree of polymerization, R the gas constant and T the thermodynamic temperature. The composite activation energy for the kinetic chain length is about -60 kJ mol^{-1} for thermal initiator decomposition but close to 0 for redox initiation^[23] (p. 274). Therefore the kinetic chain length shows rather strong exponential decrease with synthesis temperature for KPS, whereas for APS-TEMED the chain length should be rather insensitive to the synthesis temperature.

The final particle volumes in the collapsed state at different reaction temperatures for KPS and APS-TEMED initiated batches are shown in Figure 4.5. The final particle volume in the collapsed state was found out to be proportional to the 3/2 power of the initial monomer concentration, which is shown by the linearization of the final particle volume data against $[\text{NIPAM}]^{3/2}$ in Figure 4.5. Table 4.1 shows the linear fit parameters for final particle volume values.

Batches for both initiator systems show qualitatively similar temperature dependence even though the effect is considerably stronger for KPS initiated batches. For KPS (Figure 4.5 A) the final particle volume strongly decreases with increasing synthesis temperature. In addition the intercept shifts to lower values when the synthesis temperature is raised. In terms of Equation (4.2) this would mean that the number of particles increases strongly when the synthesis temperature is increased. In the case of redox initiation the decrease of the final particle volume is less pronounced (Figure 4.5 B). Intercept term is approximately constant for other temperatures, except for 50 °C, which appears to be an outlier. Neverthe-

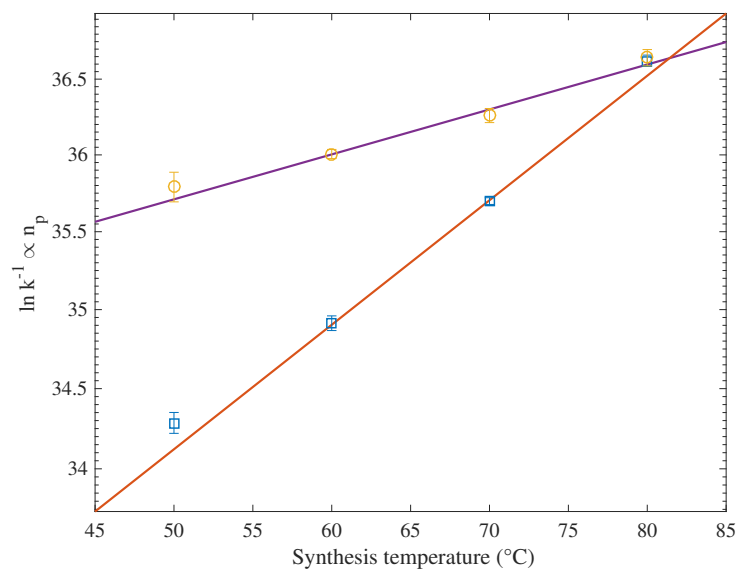


Figure 4.6: Logarithm of inverse slopes of the linear fits shown in Figure 4.5. The error bars denote the standard deviation. Solid lines are linear fits to the data. The inverse slopes k^{-1} are proportional to the number density of particles at each temperature as discussed in the context of Equation (4.5). Linearization shows that the inverse slope, or particle number density, is approximately exponentially dependent on the synthesis temperature for both KPS initiated batches (black squares) and APS-TEMED initiated batches (red circles). Temperature dependence is clearly stronger for KPS initiated batches where $k_{80^{\circ}\text{C}}^{-1}$ is 10 times $k_{50^{\circ}\text{C}}^{-1}$, whereas $k_{80^{\circ}\text{C}}^{-1}$ is only 2 times $k_{50^{\circ}\text{C}}^{-1}$ for APS-TEMED initiated batches.

less, APS-TEMED initiated batches show that the final particle volume is clearly less sensitive to the synthesis temperature, which is in line with our expectation based on the synthesis temperature dependence of the chain length. This is best demonstrated by the comparison of the inverse slopes of the linear fits k^{-1} (Figure 4.5), which are proportional to the number density of particles in the batch, as is discussed in more detail in the next section along with the interpretation of the intercepts in Figure 4.5. For both initiator types the inverse slopes exhibit approximately exponential dependence on synthesis temperature, as shown in Figure 4.6. This is in line with the number density being proportional to v^{-1} .

4.4.7 What can we say about the dependence of particle number density on initial monomer concentration?

The final particle volume in the collapsed state could be described by the empirical equation

$$V_p = k [M]_0^\alpha + V_0 \quad (4.4)$$

with $\alpha = 3/2$ and k and V_0 denoting the slope and intercept terms, respectively. V_0 has units of volume and k ($\text{dm}^{15/2} \text{mol}^{-3/2}$) for $\alpha = 3/2$. This empirical relationship might help us to reveal some details about the behavior of the number concentration function ρ_p in Equation (4.2). Substituting Equation (4.4) to (4.2) yields

$$\rho_p = \left(\frac{k [M]_0^{\alpha-1}}{V_M} + \frac{V_0}{V_M [M]_0} \right)^{-1} \quad (4.5)$$

Equation (4.5) consists of two terms. The first term forces the number density eventually towards zero with increasing initial batch monomer concentration $[M]_0$, whereas the second term is responsible for the initial increase in the number density with increasing initial monomer concentration. The behavior of Equation (4.5) is sketched in Figure 4.7 A. Our qualitative physical interpretation is as follows: For the given temperature and reaction composition polymer with certain average charge density is generated, which is determined by the polymerization kinetics and for conventional radical polymerization is given by the inverse of the kinetic chain length. For this charge density a minimum stable volume exists that the particles have to attain in order to become colloidally stable. At very low monomer concentrations this volume is difficult to reach because of the lack of polymerizable material and the precursor particles aggregate until they become colloidally stable. This leads to a decrease in the particle number density in the limit of zero initial monomer concentration and manifests itself as leveling off of

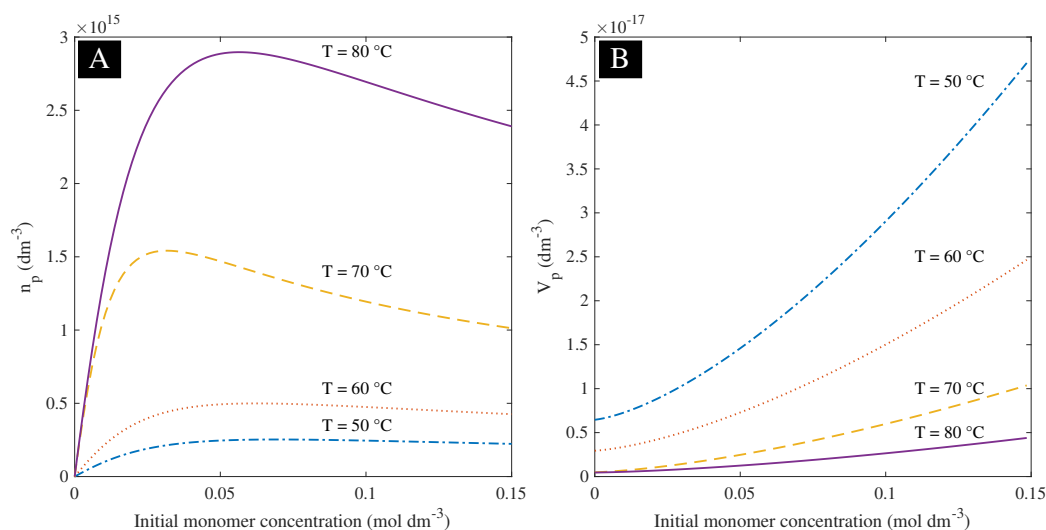


Figure 4.7: A: The behavior of the number density function according to Equation (4.5) calculated with k and V_0 parameters for KPS given in Table 4.1. Synthesis temperatures are given in the graph. Arbitrary value of $0.07 \text{ dm}^3 \text{ mol}^{-1}$ was used for V_M . Initially the number of particles increases with initial monomer concentration as more of particles with the minimum stable volume for the given charge density can be generated. The increasing kinetic chain length and decreasing charge density destabilizes the precursor particles and leads to decrease in the final particle number. This translates to the characteristic curved dependence of the final particle volume on the initial monomer concentration, as shown in **B**.

the final particle volume curve at low monomer concentrations as shown in Figure 4.7 B.

When the initial monomer concentration is increased, the minimum stable volume also increases slightly, as the initial kinetic chain length is directly proportional to the initial monomer concentration $v \propto [M]_0$. However, more monomer means more polymerizable material and the number of particles increases as the particles do not have to aggregate as much to reach the minimum stable volume.

Upon further increase a tipping point is reached when the monomer concentration is abundant enough to rapidly form the nuclei and the rest of the material is polymerized on these particles. The decrease in the particle number might be explainable by the fact that the kinetic chain increases further and the charge density decreases, which might require larger minimum particle volume. Whether this is the case or the phenomenon is due to kinetic aspects of particle formation is unaddressable by the experimental means we have employed here.

The parameter V_0 could be regarded as the smallest stable volume at a given temperature and initiator concentration in the limit of zero monomer concentra-

tion. The inverse of the parameter k provides a relative measure of the number density of the particles according to Equation (4.5). As seen in Figure 4.6 k^{-1} is approximately exponentially dependent on synthesis temperature, KPS initiated batches showing clearly higher temperature dependence than redox initiated batches, which is consistent with the prediction of our hypothesis and Equation (4.3).

In the case of APS concentration the final particle volume in the collapsed state appears to be proportional to the kinetic chain length. For this to be the case also for monomer concentration, the first term of Equation (4.5), which is the term responsible for the decreasing number density with $[M]_0$, has to include $[M]_0$, not $[M]_0^{1/2}$. This is the case if the final particle volume would be proportional to the square of the initial monomer concentration. Plotting the final particle volume data in Figure 4.6 B against $[M]_0^2$ indeed produces a credible linearization, but the precision of our experimental data does not allow us to unambiguously make a distinction between the $[M]_0^{3/2}$ and $[M]_0^2$ dependence. Nevertheless, the number of particles decreases with increasing initial monomer concentration in the batch for both cases.

4.4.8 Implications for low synthesis temperature approaches

In the light of these results the principle of low temperature synthesis method by Hu et al.^[11] and the temperature-programmed synthesis method by Meng et al.^[12] is the reduction in the number of particles at the low particle nucleation temperature and therefore increase in the final particle size. The ramp of the synthesis temperature in the method of Meng et al. serves to accelerate the reaction after the nucleation phase is completed, essentially combining low nuclei density with fast reaction times. The ramp speed has to be chosen appropriately however, as too fast a ramp results in secondary nucleation and formation of two particle populations with narrow size distributions (data not shown). Type of the initiator also has to be chosen appropriately, neither of these approaches is expected to work if an initiator system exhibiting no chain length dependence with synthesis temperature is used.

No coagulum was observed to form at any synthesis temperature with non-stirred synthesis approach in contrast to reports by Meng and Hu. In our experience the formation of coagulum results from strong agitation (fast stirring) of the reaction mixture at a reaction stage when particles are poorly stabilized. Poorly stabilized particles are created at low synthesis temperature with thermal initiator and/or high initial batch monomer concentration. The monomer concentrations used by Meng and Hu were higher than any used in this work. For instance non-stirred synthesis with high monomer concentration and KPS as initiator at 50 °C

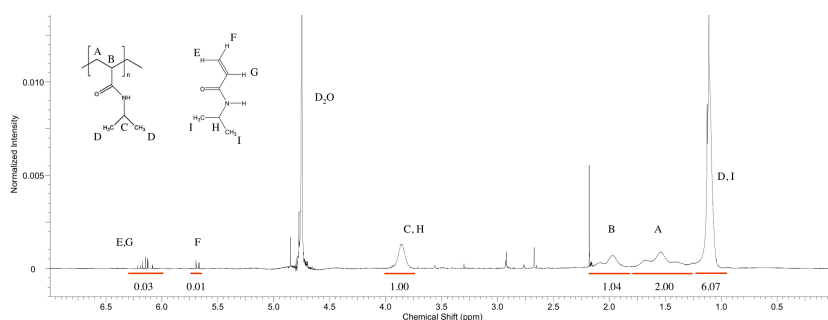
will result in sedimentation of the massive particles during the synthesis and if a reactor tube few hours into the reaction is agitated, the whole batch coagulates macroscopically. Therefore the synthesis temperature, initiator type, initial batch monomer concentration and stirring rate all have to be chosen in a way that the target particle volume is obtained without decreasing the yield due to particle aggregation.

4.5 Conclusions

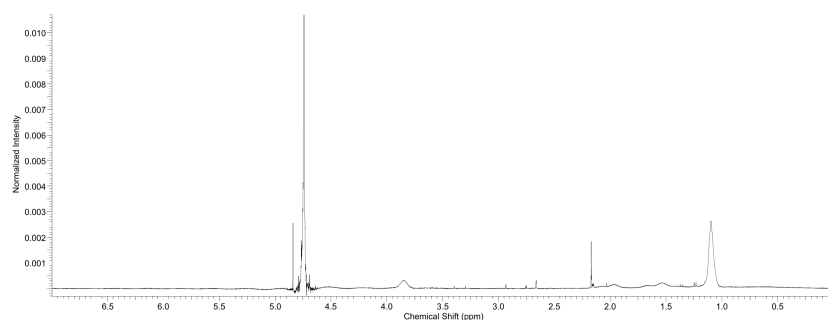
Rapid and convenient test tube polymerization yielding PNIPAM microgels with narrow size distribution was used to investigate the effect of reaction conditions on number density of microgel particles. For the first time we demonstrated that the number density of PNIPAM microgel particles is consistent with the mechanism of radical polymerization in solution. According to this hypothesis, the polymerization takes place in the continuous phase, in contrast to polymer particles as in emulsion polymerization. The particle number density can be tuned by the amount of stabilizing initiator fragments in the polymer, governed by the kinetic chain length produced in given reaction conditions.

Our results explain the mechanism of contemporary approaches such as low temperature^[11] and temperature-programmed synthesis^[12] and point out the common pitfalls in precipitation polymerization of NIPAM. An important factor were observed to be the cross-linking reactions, which significantly reduce the number density of particles in the batch. The new insight into particle formation mechanism can be used as guideline for tuning the microgel particle size for any given application and is helpful for the development of simulation models and novel synthesis methods for temperature-sensitive microgels.

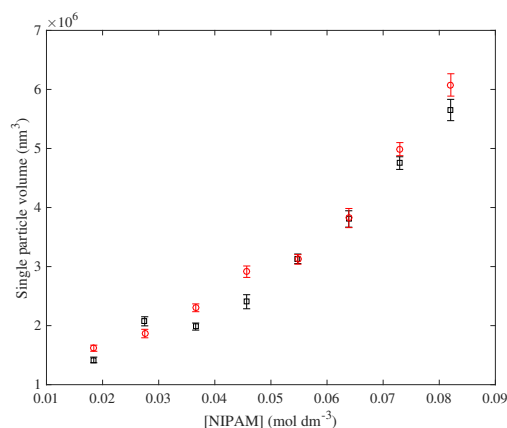
4.6 Supporting information



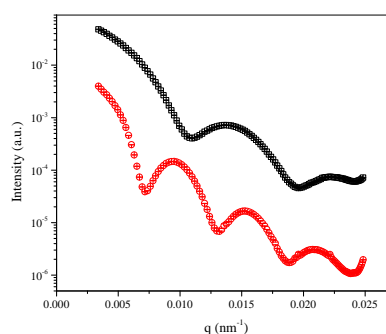
Supporting Figure 4.8: ^1H -NMR spectra of reaction mixture after polymerization in D_2O . Initial concentrations of NIPAM was $8.2 \times 10^{-2} \text{ mol dm}^{-3}$. APS concentration was 1.71 mol dm^{-3} and TEMED 1.07 mol dm^{-3} . Integrals show that there is $\approx 2\%$ unreacted monomer present in the reaction mixture. ^1H -NMR(400.30 MHz, D_2O): $\delta = 1.1 \text{ ppm}$ (6H, s), 1.55 ppm (2H, br. s), 1.95 ppm (1H, br. s), 3.8 ppm (1H, br. s), 5.6 ppm (1H, d), $6.1\text{-}6.25 \text{ ppm}$ (3H, m).



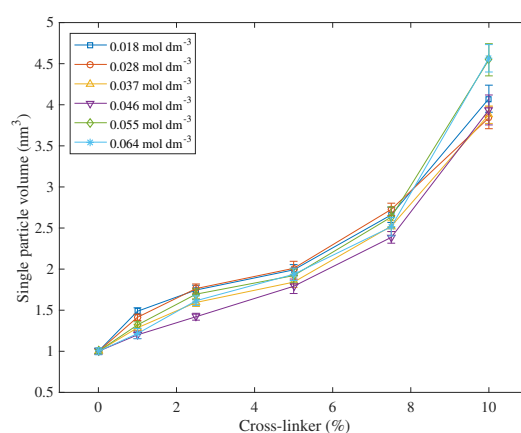
Supporting Figure 4.9: ^1H -NMR spectra of reaction mixture after polymerization in D_2O . Initial concentrations of NIPAM was $1.8 \times 10^{-2} \text{ mol dm}^{-3}$ respectively. APS concentration was 1.71 mol dm^{-3} and TEMED 1.07 mol dm^{-3} . ^1H -NMR(400.30 MHz, D_2O): $\delta = 1.1 \text{ ppm}$ (6H, s), 1.55 ppm (2H, br. s), 1.95 ppm (1H, br. s), 3.8 ppm (1H, br. s).



Supporting Figure 4.10: Collapsed final particle volume with initial NIPAM concentration for polymerization at 60 °C in water (red circles) and heavy water (black squares). APS and TEMED concentration were $1.7 \times 10^{-3} \text{ mol dm}^{-3}$ and $1.07 \times 10^{-3} \text{ mol dm}^{-3}$ in each batch, respectively. The error bars represent the 95 % confidence interval from the dynamic light scattering measurement.



Supporting Figure 4.11: Form factors for initiator cross-linked samples measured in ethanol at 20 °C. Distinguished minima indicate spherical particles with narrow size distribution despite lack of cross-linker. Black squares: polymerization with APS at 60 °C, NIPAM and APS concentrations 8.2×10^{-2} and $1.5 \times 10^{-3} \text{ mol dm}^{-3}$, respectively. Red circles: polymerization with KPS at 50 °C, NIPAM and KPS concentrations 8.2×10^{-2} and $1.5 \times 10^{-3} \text{ mol dm}^{-3}$, respectively. Intensities are arbitrarily scaled.



Supporting Figure 4.12: Final particle volume in the collapsed state with cross-linker fraction for various total monomer concentrations, normalized to 0% cross-linker batches. All batches polymerized at 60 °C using APS-TEMED as initiator system. Total monomer concentrations (NIPAM + BIS) are given in the figure. APS concentration $3.18 \times 10^{-3} \text{ mol dm}^{-3}$ with varying TEMED concentrations from highest to lowest monomer concentration: 8.38×10^{-4} , 7.19×10^{-4} , 5.99×10^{-2} , 4.80×10^{-4} , 3.61×10^{-4} and $2.42 \times 10^{-4} \text{ mol dm}^{-3}$

Bibliography

- [1] H. G. Schild, *Progress in Polymer Science*, 1992, **17**, 163–249.
- [2] R. Pelton, *Advances in Colloid and Interface Science*, 2000, **85**, 1–33.
- [3] A. Pich and W. Richtering, *Advances in Polymer Science*, 2010, **234**, 1–37.
- [4] B. R. Saunders, N. Laajam, E. Daly, S. Teow, X. Hu and R. Stepto, *Advances in Colloid and Interface Science*, 2009, **147-148**, year.
- [5] J. B. Thorne, G. J. Vine and M. J. Snowden, *Colloid and Polymer Science*, 2011, **289**, 625–646.
- [6] M. J. Serpe, J. Kim and L. A. Lyon, *Adv. Mater.*, 2004, **16**, 184–187.
- [7] J. P. Hervás Pérez, M. Sánchez-Paniagua López, E. López-Cabarcos and B. López-Ruiz, *Biosensors and Bioelectronics*, 2006, **22**, 429–439.
- [8] L. V. Sigolaeva, S. Y. Gladys, A. P. H. Gelissen, O. Mergel, D. V. Pergushov, I. N. Kurochkin, F. A. Plamper and W. Richtering, *Biomacromolecules*, 2014, **15**, 3735–3745.
- [9] O. Kudina, A. Zakharchenko, O. Trotsenko, A. Tokarev, L. Ionov, G. Stoychev, N. Puretskiy, S. W. Pryor, A. Voronov and S. Minko, *Angew. Chem. Int. Ed.*, 2013, **53**, 483–487.
- [10] S. Wiese, A. C. Spiess and W. Richtering, *Angew. Chem. Int. Ed.*, 2012, **52**, 576–579.
- [11] X. Hu, Z. Tong and L. A. Lyon, *Langmuir*, 2011, **27**, 4142–4148.
- [12] Z. Meng, M. H. Smith and L. A. Lyon, *Colloid and Polymer Science*, 2009, **287**, 277–285.
- [13] T. Still, K. Chen, A. M. Alsayed, K. B. Aptowicz and A. G. Yodh, *Journal of Colloid and Interface Science*, 2013, **405**, 96–102.
- [14] J. Gao and B. J. Frisken, *Langmuir*, 2003, **19**, 5217–5222.
- [15] W. McPhee, K. C. Tam and R. Pelton, *Journal of Colloid and Interface Science*, 1993, **156**, 24–30.
- [16] M. Andersson and M. S. L., *Journal of Polymer Science Part B Polymer Physics*, 2006, **24**, 3305–3314.

- [17] K. von Nessen, M. Karg and T. Hellweg, *Polymer*, 2013, **54**, 5499–5510.
- [18] X. Wu, R. H. Pelton, A. E. Hamielec, D. R. Woods and W. McPhee, *Colloid and Polymer Science*, 1994, **272**, 467–477.
- [19] O. L. J. Virtanen and W. Richtering, *Colloid and Polymer Science*, 2014, **292**, 1743–1756.
- [20] R. H. Pelton, H. M. Pelton, A. Morphesis and R. L. Rowell, *Langmuir*, 1989, **5**, 816–818.
- [21] D. Duracher, A. Elaissari and C. Pichot, *Journal of Polymer Science Part A Polymer Chemistry*, 1999, **37**, 1823–1837.
- [22] J. Gao and B. J. Frisken, *Langmuir*, 2003, **19**, 5212–5216.
- [23] G. Odian, *Principles of Polymerization*, Wiley Interscience, 4th edn, 2004.
- [24] M. Rubinstein and R. H. Colby, *Polymer Physics*, Oxford University Press, 2003.
- [25] R. H. Pelton, *Journal of Colloid and Interface Science*, 2010, **348**, 673–674.
- [26] M. Stieger, J. S. Pedersen, W. Richtering and P. Lindner, *Journal of Chemical Physics*, 2004, **120**, 6197–6206.
- [27] P. J. Flory, *Principles of Polymer Chemistry*, Cornell University Press, 1953.

5. The next step in precipitation polymerization

5.1 Abstract

Many applications of poly(*N*-isopropylacrylamide) microgels necessitate robust control over particle size. Here we derive scaling law for the particle size in precipitation polymerization of *N*-isopropylacrylamide. The average particle volume in collapsed state is proportional to monomer ([M]) and initiator ([I]) concentration according to $\bar{V}_p \propto [M]^{5/3} [I]^{-4/3}$. The derived power law agrees well with experimentally observed particle volume. The derivation assumes the particle number density to depend on the initiation rate and the surface charge density of monochain globules generated during the nucleation phase. The model also qualitatively predicts the experimentally observed particle size trends when reaction temperature or chain transfer agent concentration are varied. Reaction rate measurements show that the reaction proceeds initially as radical solution polymerization, therefore justifying the use of Flory-Schulz approximation for the globule surface charge density in this work.

5.2 Introduction

Hydrogels are good candidates for bioapplications due to their biocompatibility, which arises from similarities in the properties of soft living tissues and hydrogels: Both are elastic water swollen structures with similar mechanical stiffness. Producing hydrogels in colloidal nanoparticle form increases the versatility of hydrogels further as they can be administered directly to circulation^[1,2] or used as building blocks for macrostructures, such as 2D films suitable for cell culture substrates that enable convenient cell harvesting.^[3,4]

A contemporary archetype for colloidal hydrogels are stimuli-sensitive poly(*N*-

isopropylacrylamide) (PNIPAM) microgels. These cross-linked polymer particles are easily produced by precipitation polymerization^[5] of *N*-isopropylacrylamide (NIPAM), which yields spherical colloidal gels in the radius range of tens of nanometers to some micrometers. They owe their temperature sensitivity to the properties of PNIPAM^[6] and other stimuli-sensitive properties to functional comonomers. The stimuli-sensitivity can be exploited in microgels for various targeted applications.^[7,8,9]

One of the important properties of microgels in respect to applications is their mechanical strength. For instance, it has been demonstrated that deformable soft microgel particles exhibit longer circulation time in blood stream in contrast to hard nanoparticles.^[2] Lately preparation methods for hollow^[10,11,12] and large ultra low cross-linked^[13,14,15] PNIPAM microgels have been introduced; these particles typically exhibit high swelling degrees and deformability at interfaces^[16]. We have recently demonstrated that the ultra low cross-linked particles are actually hollow PNIPAM shells, which can be realized in an easy batch synthesis.^[17] These ultra low cross-linked particles can translocate through pores that are significantly smaller than their hydrodynamic radius in dispersion, in analogy to cells.^[15,18,19,20]

Another key aspect in microgel synthesis is the particle size control. For example, the circulation time of nanoparticles can be extended further if the particle size is kept below 100 nm.^[1] The standard method to achieve small microgel particle sizes is to use an additional surfactant, such as sodium dodecyl sulfate (SDS), in the synthesis.^[21] Alternative approaches to size modulation include copolymerization with ionizable monomers^[22,23] or macromonomers.^[24,25]

When no additional components are desired, an attractive prospect to tune the particle size to the suitable size range is to take advantage of the inherent properties of precipitation polymerization, which however requires knowledge on the mechanism of the reaction. Information on the fundamentals of precipitation polymerization of NIPAM is surprisingly sparse in the literature, even though the reaction has been in continuous use for over 20 years.^[26] According to the original hypothesis by Wu et al.^[27] the reaction would follow Smith-Ewart type 3 kinetics^[28]; in the work of Duracher et al.^[29] on *N*-isopropylmethacrylamide the locus of polymerization was also assumed to be in the polymer particles. Meunier et al.^[30] present kinetic data on PNIPAM based cationic gel particles, but do not present a clear conclusion on the reaction mechanism.

The connection of particle size and the reaction mechanism has been discussed in earlier work.^[29,31] In the lack of additional surfactant the PNIPAM particle nuclei will be stabilized by the charged initiator fragments. The number of stable particles at the end of the nucleation phase therefore depends on the average number of chain ends per polymerized monomers. In other words, the differences in the particle number density in different reaction conditions arise from the aver-

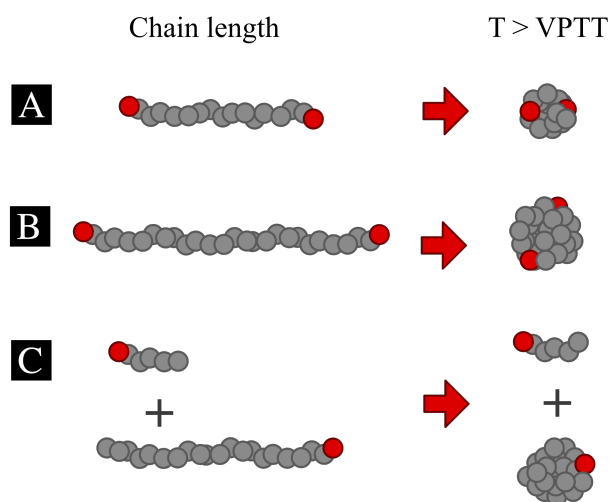


Figure 5.1: The relationship between the chain length x and the surface charge density of monochain polymer globules. Red circles denote charged initiator fragments and grey circles monomer repeating units. Changing the reaction conditions changes the average chain length of the generated chains. The surface charge density of the collapsed globules is higher for shorter chains, **A**, in comparison to longer chains, **B**. In the presence of chain transfer agent (**C**), some of the chains are too short to undergo collapse above the VPTT. They cannot therefore act as stabilizers and contribute charges to primary aggregates, which leads to lower surface charge density of the aggregates. This is in contrast to surfactants, such as SDS, which always have a hydrophobic part and end up in the particles.

age degree of polymerization, which changes with monomer, initiator and chain transfer agent concentration as well as reaction temperature. This concept is qualitatively depicted in Figure 5.1.

Building on this mechanism, we derive scaling laws to account for the average final particle volume of the microgels. The two main assumptions are that the number of particles in the batch is proportional to the initiation rate and surface charge density of monochain globules produced during the nucleation phase.

The kinetic measurements presented first in this work in fact indicate the reaction to proceed as radical solution polymerization briefly after the initiation. A simple approximation for the monochain surface charge density under these reaction conditions is provided by Flory-Schulz distributions derived for chain transfer modulated radical solution polymerization. Comparison with experimental data shows that the particle volume adheres to the theoretical power laws in respect to monomer and initiator concentration. Deviations from the power law

at low monomer concentration regime and the particle volume in the presence of chain transfer agent can be qualitatively explained when the critical length for coil-to-globule transition is accounted for.

5.3 Experimental

5.3.1 Particle synthesis for size determination

Non-stirred precipitation polymerization was used to produce the particles for final particle volume analysis. Reaction parameters and hydrodynamic radii of particles are available in Supporting Information. This method has been described in detail in previous work.^[32] Briefly: A series of aqueous solutions are prepared by diluting from a master solution in a way that the concentration of the reactant of interest varies and all other reactants stay constant. 1 ml of solutions are transferred to test tubes of 10 mm diameter and sealed with rubber septa. Solutions are purged with nitrogen through the septa for 20 min to remove oxygen and then immersed to a well regulated oil bath. Typical reaction temperatures vary from 50 °C to 80 °C. The reaction temperature needs to be stable during the nucleation time shortly after the immersion of the tubes to ensure reproducible results. The tubes are left to react for at least an hour and then transferred to a hot oven without letting the dispersion to cool below PNIPAM volume-phase transition temperature (VPTT). This ensures that the sol fraction does not detach from the particles and the collapsed volume reflects the weight of the particles. If thermally decomposing initiator such as potassium persulfate (KPS) is used, all the reactants can be mixed together at room temperature and deoxygenated. If redox system such as ammonium persulfate (APS) - N,N,N',N'-tetramethylethylenediamine (TEMED) is used, all the other reactants except APS can be mixed together and transferred to test tubes (0.5 ml per tube). After APS solutions have been deoxygenated, 0.5 ml of APS solution is transferred to 1 ml syringes equipped with 120 mm needles, and inserted into the test tubes; the needles are not immersed in to the monomer solution. The monomer mixture is deoxygenated as above, and the tubes with syringes are immersed to oil bath. To initiate the reaction, the needles are pressed to the bottom of the tubes, APS solution is injected, and the syringes with needles removed.

5.3.2 Polymer synthesis for chromatography

In order to confirm the effect of 2-mercaptoethanol as chain transfer agent (CTA), 7 batches of PNIPAM at various 2-mercaptoethanol concentrations were synthesized. The polymerization was carried out in water at room temperature. Solutions

with various CTA concentrations were made, 3 ml of monomer-TEMED solution were transferred to 7 20 ml vials equipped with stirring bars and sealed with septa. The solutions were purged with nitrogen for 1 h. APS-CTA solutions were purged in separate vials. To initiate the reaction, 3 ml of APS-CTA solution were injected to the 20 ml vials. The reaction was left to proceed overnight. The solutions were then lyophilized without further purification.

5.3.3 Calorimetry

A RC1su reaction calorimeter with a triple-walled 500 ml RTCAL glass reactor by Mettler-Toledo was used to measure the heat produced by the cleavage of the double bonds of NIPAM during the polymerization. The measuring principles have been reported in literature.^[33,34] The calorimeter was set to an isothermal mode, meaning that the reaction temperature T_r was set to a constant value of 60 °C while the jacket temperature T_j changed automatically to maintain T_r constant. The heat of polymerization is measured by monitoring the heat flow between the reaction vessel and the heating jacket using a thermocouple embedded in the polymer matrix at the inner glass wall of the jacket. The reaction heat curve is obtained with a resolution of 2 s between the measurements.

The polymerization was carried out in 100 ml reaction mixtures. Monomer and TEMED were dissolved in double distilled water inside the glass reactor, purged with argon for 30 min and equilibrated for 60 min under stirring (100 rpm) to the desired reaction temperature. Subsequently a preheated degassed solution of APS and 2-mercaptoethanol in 0.5 ml double distilled water was added rapidly through a 1 ml syringe into the reactor.

5.3.4 Dynamic light scattering

The final particle volumes of microgels were measured in the collapsed state. Reaction mixtures were transferred to an oven without letting the polymerization tubes to cool below the VPTT. A drop of dispersion was transferred with a preheated needle and 1 ml syringe to 10 ml of double distilled water tempered at 60 °C. The high dilution is necessary to prevent multiple scattering during the light scattering experiment. The diluted dispersions were transferred to preheated dynamic light scattering (DLS) cuvettes and transferred rapidly to the toluene bath of the laser goniometer, which was tempered at 50 °C. Typically 25 correlograms with 90 s acquisition time were recorded throughout the available q range. The scattering vector magnitude is given by $q = 4\pi n/\lambda \sin(\theta/2)$, where n is the refractive index of the dispersion, λ the wavelength of the incident radiation in vacuum and θ the scattering angle. The mean decay rate of the electric field correlation function was determined by 2nd order cumulant analysis.^[35] The best

estimate for the mean diffusion coefficient was then obtained by linear regression from

$$\Gamma_2 = Dq^2$$

where Γ_2 is the mean decay rate of the electric field correlation function at scattering vector magnitude q , and D is the mean diffusion coefficient particles. The instrument was a 3D DLS laser goniometer built from ALV GmbH and LS Instruments AG parts. ALV electronics and software were used to control the instrument. The data was acquired in normal DLS mode, i.e. the other beam was blocked during the acquisition, resulting in one scattering vector.

5.3.5 Size exclusion chromatography (SEC)

SEC analysis was performed at 40 °C using a high-pressure liquid chromatography pump (Bischoff 2250) and SEC-3010 Differential RI / Viscometer detector (WGE Dr. Bures GmbH). The eluting solvent was dimethylformamide (DMF) with 1 g dm⁻³ LiBr and a flow rate of 1.0 cm³ min⁻¹. Polymer concentration was 1 g dm⁻³ in all samples. Five columns with PSS 90 GRAM material were used. The length of the precolumn was 50 mm and the diameter 8 mm. The remaining four columns had a length of 300 mm, diameter of 8 mm, particle size of 10 μm, and the nominal pore widths were 30, 100, 1000 and 3000 Å.

5.4 Results and Discussion

5.4.1 Reaction rate measurements indicate solution polymerization kinetics shortly after initiation

Figure 5.2 shows calorigrams recorded for reactions with various NIPAM and initiator concentrations. Redox system consisting of APS and TEMED was used to initiate the reaction. The heat output in the reaction is mainly due to the cleavage of the NIPAM double bonds; the heat flow measured during the reaction is directly proportional to the reaction rate. The calorigrams for various NIPAM concentrations were integrated to obtain the total reaction enthalpy for each reaction. Linear regression to the data points gives the best estimate for the heat of polymerization of NIPAM as 84.5 ± 0.3 kJ mol⁻¹ (Supporting Information). This value is comparable with the heat of polymerization of many other alkenes.^[36]

Close inspection of calorigrams with variable NIPAM concentrations in Figure 5.2 A reveals an increase in the reaction rate at the end of the reaction for the highest NIPAM concentrations. This sort of behavior is typical of autoacceleration (Trommsdorff effect), where the termination reactions of the growing chains

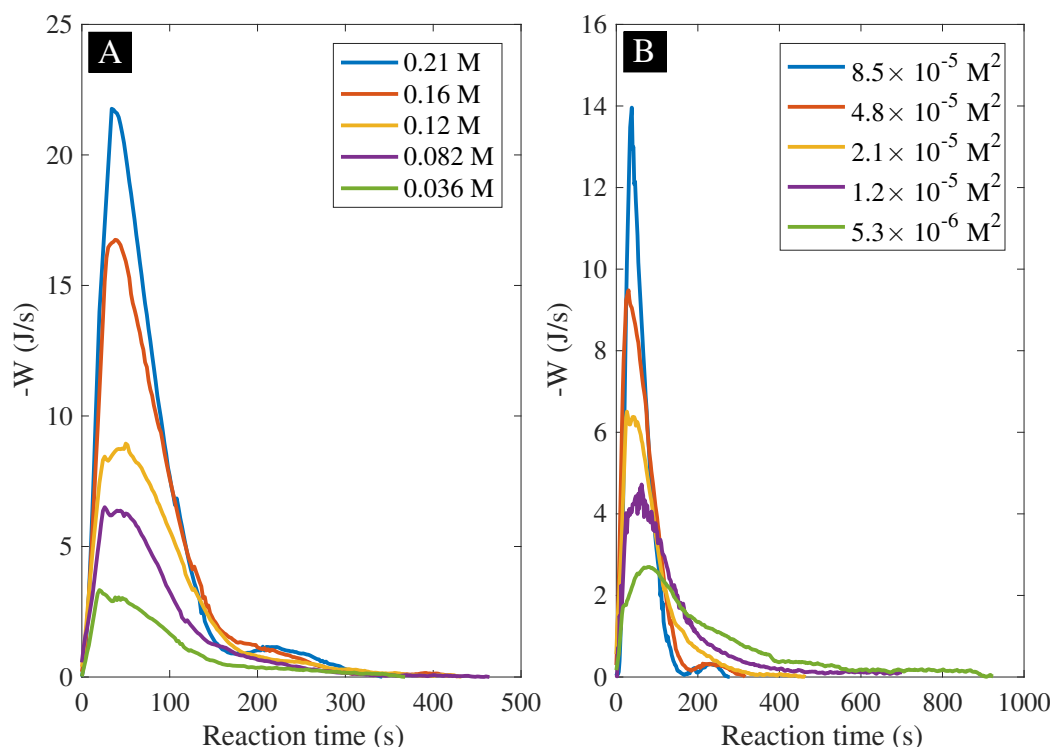


Figure 5.2: Calorigrams for reactions with various reactant compositions. **A:** Variable NIPAM concentration (legend). APS and TEMED concentrations were kept constant at 3.1×10^{-3} and 6.8 mol dm^{-3} , respectively. **B:** Variable APS and TEMED concentrations, given as product of the reagents (legend). APS and TEMED were added in 1:1 mole ratio. NIPAM concentration was kept constant at $8.2 \times 10^{-2} \text{ mol dm}^{-3}$.

are hindered due to high viscosity, but small weight unreacted monomer is mobile enough to reach the active sites.^[36] For these batches coagulation around the stirrer shaft and blade were observed after the reaction; it is therefore possible that propagating radicals get trapped in the agglomerates where autoacceleration takes place.

The calorigrams for various APS and TEMED concentrations (added always in 1:1 ratio) in Figure 5.2 B show that the reaction rate is also sensitive to the initiator concentration. The total reaction enthalpy of different batches is in the range of 680 – 690 kJ for the first three initiator concentrations but then jumps to 800 kJ for the two highest concentrations. Constant enthalpy was expected for all the batches. The increase in enthalpy is likely an artifact arising from the rapid start of the reaction in combination with power fluctuation caused by the initiator injection. This fluctuation was easier to correct for the batches with less initiator.

The maximum reaction rates with NIPAM concentration and the product

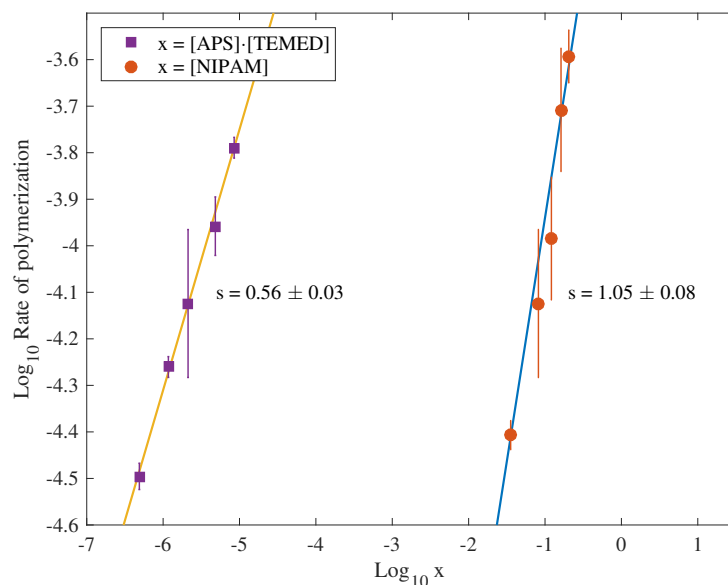


Figure 5.3: Power law dependence of reaction rate with the product of APS and TEMED concentrations and NIPAM concentration.

of APS and TEMED concentrations linearize acceptably in log-log presentation (Figure 5.3), giving the best estimates for the power law exponents as 0.56 ± 0.03 and 1.05 ± 0.08 for initiator and monomer concentrations, respectively. The maximum rate is achieved rapidly after the initiation, when the concentration of unreacted monomer is high in the continuous phase. NIPAM, APS and TEMED are well soluble to reaction medium, which means that the initiation and significant propagation takes place in the continuous phase. The polymer globules at the beginning of the reaction are small^[37] and any propagating globules likely terminate rapidly upon encounter in the continuous phase similarly to chains in open conformation in normal radical solution polymerization. Considering these aspects it is not surprising that the power law exponents are close to the theoretically predicted for radical solution polymerization: $1/2$ and 1 for initiator and monomer concentrations,^[38,36] respectively.

5.4.2 Scaling laws for the particle volume

PNIPAM microgels form homogeneous spherical particles above the VPTT.^[39] Assuming the majority of monomer is polymerized to particles, the average volume of the collapsed particles is approximately

$$\bar{V}_p = \frac{\sum V_i}{\rho_p} = \frac{V_M}{\rho_p} [M]_0 \propto \frac{1}{R_i \cdot \bar{\rho}_A} [M]_0 \quad (5.1)$$

where V_i is the volume of the i th particle, V_M the volume of collapsed PNIPAM network above the VPTT (including the water inside the network) polymerized from one mole of NIPAM, $[M]_0$ the initial monomer concentration in the batch and ρ_p the number density function that depends on the reaction conditions.

\bar{V}_p is a convenient quantity that can be determined by a careful DLS measurement, and it is proportional to the average weight of the particles at the end of the reaction. This is however only the case if the particles are not left to cool down between characterization and synthesis; otherwise the sol fraction^[29] will detach from the particles and the result does not anymore represent the situation in the reactor.

As a simple approximation, we assume the number of particles at the end of the nucleation phase to be proportional to the initiation rate R_i and surface charge density of the monochain globules $\bar{\rho}_A$ generated in the continuous phase during nucleation, i.e., $n \propto R_i \cdot \bar{\rho}_A$. The initiation rate sets the upper limit to the particle number density and surface charge density is a measure of degree of aggregation necessary to stabilize the nuclei.

PNIPAM particles typically have a narrow size distribution, which implies that the nucleation period at the beginning of the reaction is short. The nucleation likely proceeds by precipitation of chains on each other, and ends when these primary aggregates have accumulated sufficient charge to repel aggregates of similar size. Given radical solution polymerization mechanism, the Flory-Schulz estimate of the monochain globule surface charge density is given by

$$\bar{\rho}_A(x_c) = \frac{\bar{N}_-}{(v_0 \bar{N})^{2/3}} \propto \frac{\bar{n}_{xc,1} + 2\bar{n}_{xc,3} + \bar{n}_{xc,4}}{\bar{x}_{xc}^{2/3}} \quad (5.2)$$

Here \bar{N}_- is the average number of negatively charged initiator fragments in a globule and $(v_0 \bar{N})^{2/3}$ the surface area of the average globule; v_0 being the volume occupied by one repeating unit in the collapsed network (with water) and \bar{N} the average number of repeating units in a chain. Symbol \propto denotes proportionality up to a constant factor. Mole fraction of polymer species i longer than x_c is denoted by $\bar{n}_{xc,i}$. Different species in chain transfer modulated polymerization are given in Table 5.1.

Only polymer moieties longer than the critical length for chain collapse x_c contribute to the nucleation process. The instantaneous mole fractions of all the possible polymer molecules of length x in chain transfer modulated radical solution polymerization are given by

Table 5.1: Structure of species formed in radical chain polymerization in the presence of chain transfer agent. An initiator fragment is denoted by I, a reinitiating chain transfer agent fragment by CT, repeating units by M and x is the number units in the chain. In Flory-Schulz scheme the initiating fragments are counted in the overall chain length.

Designation	Structure	Chain length	No. of kinetic chains
1	$I-M_{x-1}$	x	1
2	$CT-M_{x-1}$	x	1
3	$I-M_{x-2}-I$	x	2
4	$I-M_{x-2}-CT$	x	2
5	$CT-M_{x-2}-CT$	x	2

$$n_{x,1} = \frac{2p_{tr}(1-p_{tr})}{1+p_{tr}}(1-p)p^{x-1} \quad (5.3)$$

$$n_{x,2} = \frac{2p_{tr}^2}{1+p_{tr}}(1-p)p^{x-1} \quad (5.4)$$

$$n_{x,3} = \frac{(1-p_{tr})^3}{1+p_{tr}}(1-p)^2(x-1)p^{x-2} \quad (5.5)$$

$$n_{x,4} = \frac{2p_{tr}(1-p_{tr})^2}{1+p_{tr}}(1-p)^2(x-1)p^{x-2} \quad (5.6)$$

$$n_{x,5} = \frac{p_{tr}^2(1-p_{tr})}{1+p_{tr}}(1-p)^2(x-1)p^{x-2} \quad (5.7)$$

The chain length x depends on the probability of any active center to propagate p and the fraction of termination by chain transfer p_{tr} . In Equation 5.2 only the charge bearing molecules affect the surface charge whereas the overall average degree of polymerization of chains exceeding the critical length, \bar{x}_{xc} , determines the average surface area.

Equations 5.2 to 5.7 are useful for understanding how the scaling laws for final particle volume derived below behave in the limit of low monomer concentration and in the presence of chain transfer agent. For details regarding equations 5.3 to 5.7, p and p_{tr} , and the numerical values for parameters used in this work, see Supporting Information.

In the absence of chain transfer agent only polymer formed by combination of two kinetic chains (Species 3, Table 5.1) is present during the nucleation phase. At constant initiator concentration, and given $[M]_0$ is sufficiently large so that the

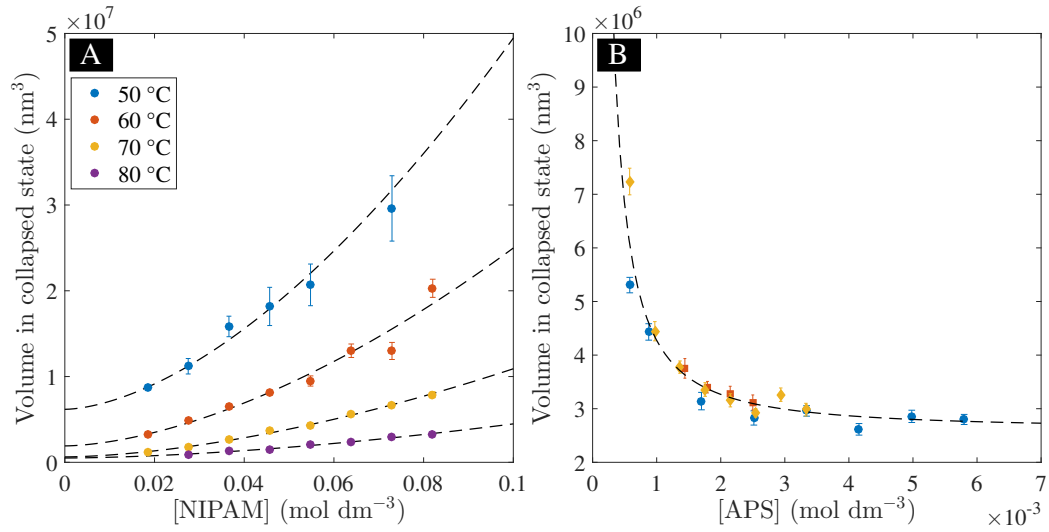


Figure 5.4: Effect of reaction temperature and monomer concentration as well as initiator concentration on the final particle volume in collapsed state. **A**: Final particle volume in collapsed state with NIPAM concentration at different reaction temperatures. KPS concentration was $1.56 \times 10^{-3} \text{ mol dm}^{-3}$ in all batches. Dashed lines are least squares fits on equation $\bar{V}_p = B[\text{NIPAM}]^{5/3} + C$. **B**: Final particle volume with APS concentration. Different symbols denote the repetition of the synthesis. NIPAM and TEMED concentrations were $5.29 \times 10^{-2} \text{ mol dm}^{-3}$ and $1.72 \times 10^{-3} \text{ mol dm}^{-3}$, respectively, in all batches. Dashed line is a least squares fit on equation $\bar{V}_p = B[\text{APS}]^{-4/3} + C$. Error bars denote the standard deviation of the DLS measurement.

role of x_c is negligible, the number density of particles at reaction temperature T is proportional to

$$\rho_p([M]_0, T) \propto R_i \cdot \bar{\rho}_A = k_d(T)[I]_0 \cdot \frac{2}{(v_0 \sum x n_{x,3})^{2/3}} \propto \frac{k_d(T)}{\bar{x}^{2/3}} \propto \frac{k_d(T)}{[M]_0^{2/3}} \quad (5.8)$$

where $[I]_0$ is the batch initiator concentration and k_d is the rate constant of initiator dissociation. Similarly for constant monomer concentration and temperature

$$\rho_p([I]_0) \propto R_i \cdot \bar{\rho}_A \propto k_d[I]_0 \cdot \frac{2}{\bar{x}^{2/3}} \propto [I]_0^{4/3} \quad (5.9)$$

Substitutions of reactant concentrations to \bar{x} follow directly from well-known expressions for kinetic chain length in steady-state radical solution polymerization. Substitution of Equations 5.8 and 5.9 to Equation 5.1 reveal power law dependency of final particle volume in respect to monomer and initiator concentration

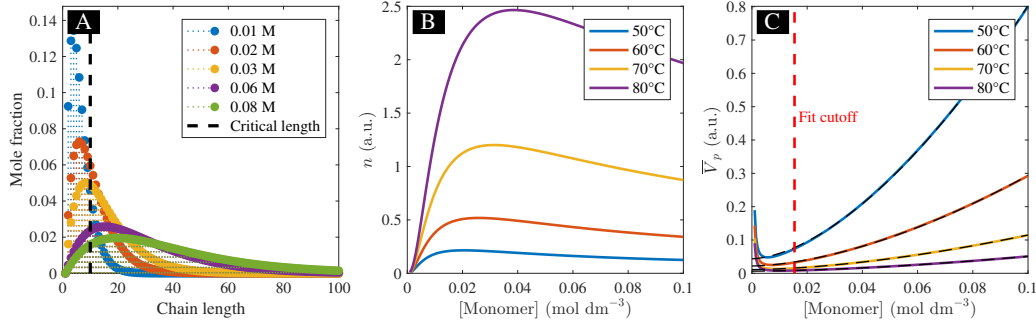


Figure 5.5: **A:** Chain length distributions from Equation 5.5 for 60 °C curve shown in C. **B:** Particle number density with monomer concentration, calculated as $k_d(T)/k_d(50^\circ\text{C}) \cdot \bar{\rho}_A$ with $\bar{\rho}_A$ given by Equation 5.2. **C:** Average particle volume calculated as $[\text{Monomer}]/n$.

$$\bar{V}_p([\text{M}]_0, T) \propto k_d(T)^{-1} [\text{M}]_0^{5/3} \quad (5.10)$$

$$\bar{V}_p([\text{I}]_0) \propto [\text{I}]_0^{-4/3} \quad (5.11)$$

Experimental data and least squares fits to the power laws are shown in Figure 5.4. The final particle volume in collapsed state follows $[\text{M}]^{5/3}$ dependence well when a non-negative intercept term is allowed, as seen in Figure 5.4 A. The best fitting power law exponent was determined by least squares fitting; the scaling law exponent of $5/3$ (≈ 1.68) is close to the best fitting exponent 1.5 ± 0.3 . In the case of variation of initiator concentration, the best fitting scaling law exponent -1.2 ± 0.2 also shows only a small deviation from $-4/3$ (≈ -1.33), and the theoretical exponent describes the data well (Figure 5.4 B).

The positive intercept term in the limit of zero monomer concentration can be explained by the exclusion of short chain fractions from the nucleation process. Figure 5.5 A shows that when the batch monomer concentration is low, only the longest chains exceed the threshold for chain collapse, x_c . Consequently the surface charge density of the globules drops sharply with decreasing monomer concentration and leads to decrease in the particle number density in the low monomer concentration regime, shown in Figure 5.5 B. The dashed lines in 5.5 C show that the final particle volume still follows $\bar{V}_p \propto [\text{M}]^{5/3}$ dependence, but the drop in the particle number density leads to a positive intercept, which was experimentally verified in Figure 5.4 A. Possible loss of material due to chain exclusion is discussed in Supporting Information.

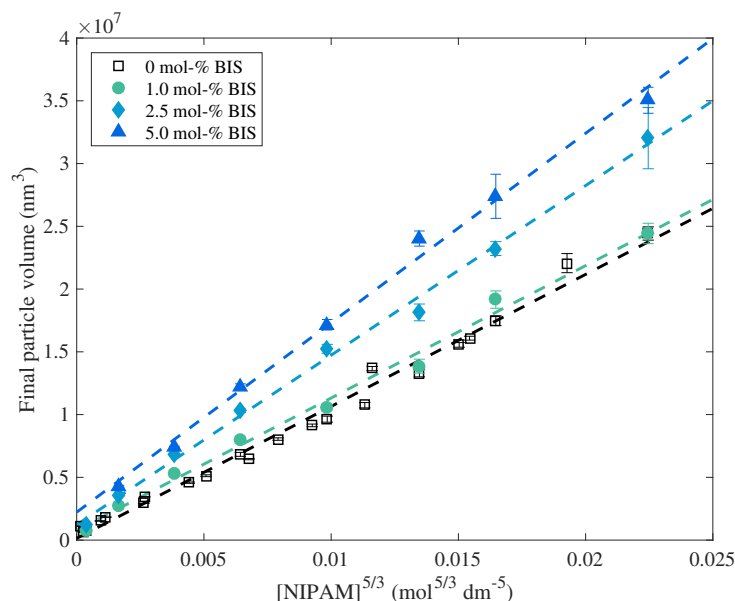


Figure 5.6: Effect of crosslinker on the particle volume. KPS concentration was $1.56 \times 10^{-3} \text{ mol dm}^{-3}$ and polymerization temperature 70°C .

5.4.3 Scaling law for particle volume applies in the presence of cross-linker

Practical work often necessitates the use of crosslinker in the synthesis, even though it is possible to prepare particles solely by persulfate initiator crosslinking.^[13,17] Use of crosslinker in precipitation polymerization is known to increase the final particle volume.^[32,17] Figure 5.6 shows series of particles polymerized with 0 to 5.0 mol-% N',N-methylenebisacrylamide (BIS) at 70°C . Linearization of \bar{V}_p against $[\text{NIPAM}]^{5/3}$ shows that the power law scaling applies in this typical crosslinker range. At 1 mol-% BIS no significant difference to crosslinker free synthesis can be observed; in the cases of 2.5 mol-% and 5.0 mol-% the average final particle volume in collapsed state increases significantly. Small quantity of BIS does not warrant a significant increase in the molar volume or water affinity of the collapsed network; instead the increase in volume reflects the increased mass of the particles.

This increase can be attributed to the decrease in particle number density with increasing crosslinker concentration and more efficient capture of short chain fractions from the continuous phase. The decrease in particle density arises from the increased probability of irreversible aggregation of polymer globules during the nucleation phase, when globules with active centers react with unpolymerized

double bonds of BIS in other globules.

5.4.4 2-mercaptoethanol can be used as charge exclusion agent

Chain transfer agent terminates many initiator started chains at low chain length, which leads to charge exclusion from the primary aggregates. 2-mercaptoethanol (ME) was used to increase the mole fraction of short chains unable to undergo chain-to-globule transition, and thus increase the final particle volume.

Figure 5.7 presents the experimental final particle volume data for batches synthesized in the presence of ME, as well as the corresponding calculated examples. Figure 5.7 A, B and C shows data from experiments, which were used to test this hypothesis by polymerizing NIPAM at constant NIPAM-to-ME ratio, constant ME concentration in every batch and variable ME concentration when all the other parameters were kept constant, respectively.

In chain transfer modulated synthesis all the polymer species from Table 5.1 are present; the effect of chain transfer on the average surface charge density of monochain globules was approximated from Equation 5.2 (Figure 5.7 D, E and F). The qualitative behavior of the final particle volume was calculated from Equation 5.1 up to a constant factor and is shown in Figure 5.7 G, H and I.

Figure 5.7 A shows that addition of small mole fraction of ME in the monomer mixture causes a drastic increase in the average particle volume, which can be attributed to the decrease in particle number density in accordance to Equation 5.1. The hydrophilicity of the ME hydroxide groups can be a contributing factor to the enlarged volume through increase in the amount of bound water in the collapsed network, but the minute concentrations used here hardly explain the drastic volume change.

The final particle volume grows at notably higher rate with batch monomer concentration in comparison to synthesis where no ME was used. The best fitting exponent for the ME containing batches was determined to be 2.1 in contrast to 1.5, determined previously for the non-ME polymerization. The change in growth rate is due to the abrupt decrease in globule surface charge density (Figure 5.7 D), which causes the monochain globules to aggregate to a notably higher extent than in the absence of ME.

The explanation for the rapid drop in average monochain surface charge density is the shift from termination by coupling to significant termination by chain transfer. The effect of chain transfer on Flory-Schulz distributions is presented in Figure 5.8; the dashed lines denote the threshold length for coil-to-globule transition. Figure 5.8 A shows that the number fraction of telomers and short chains increases strongly with ME concentration. Due to their low degree of polymerization they constitute a small fraction of the polymer mass (Figure 5.8 B) and consequently the majority of polymer is retained in the particles. Many of the

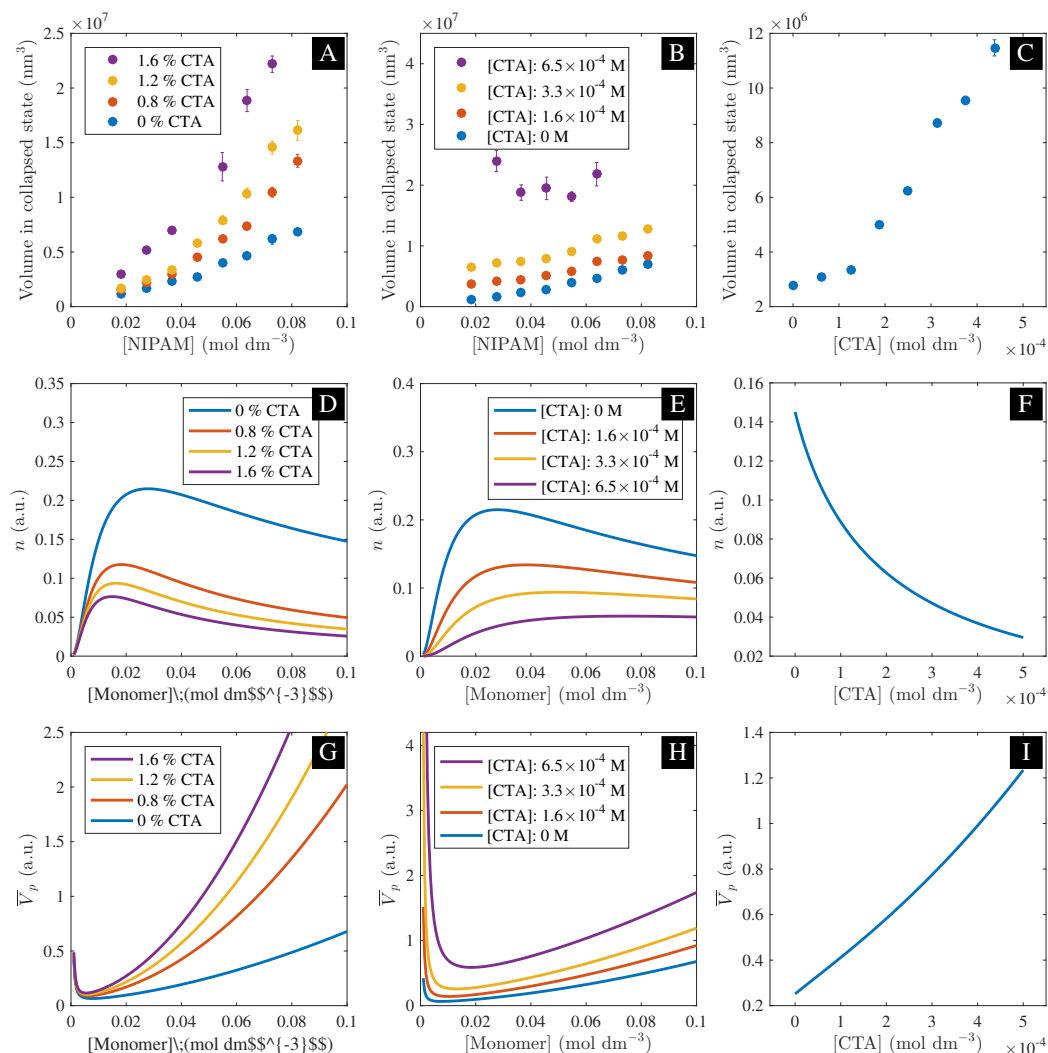


Figure 5.7: Effect of chain transfer agent concentration on the final particle volume. **A:** Constant NIPAM-to-ME ratio. The inset shows the mole percentage of ME. APS and TEMED concentrations were $1.56 \times 10^{-3} \text{ mol dm}^{-3}$ and $3.42 \times 10^{-3} \text{ mol dm}^{-3}$, respectively. **B:** Constant ME concentration. APS and TEMED concentrations were the same as in A. **C:** variable ME concentration at constant NIPAM, APS and TEMED concentrations, which were $3.65 \times 10^{-2} \text{ mol dm}^{-3}$, $7.8 \times 10^{-4} \text{ mol dm}^{-3}$ and $8.6 \times 10^{-4} \text{ mol dm}^{-3}$, respectively. **D, E** and **F** show the corresponding globule surface charge density plots and **G, H** and **I** the corresponding monomer concentration divided by charge density plots. The exact parameters for the Flory-Schulz calculation can be found in the supporting information. All polymerizations were carried out at 60°C . Error bars denote the standard deviation of the DLS measurement.

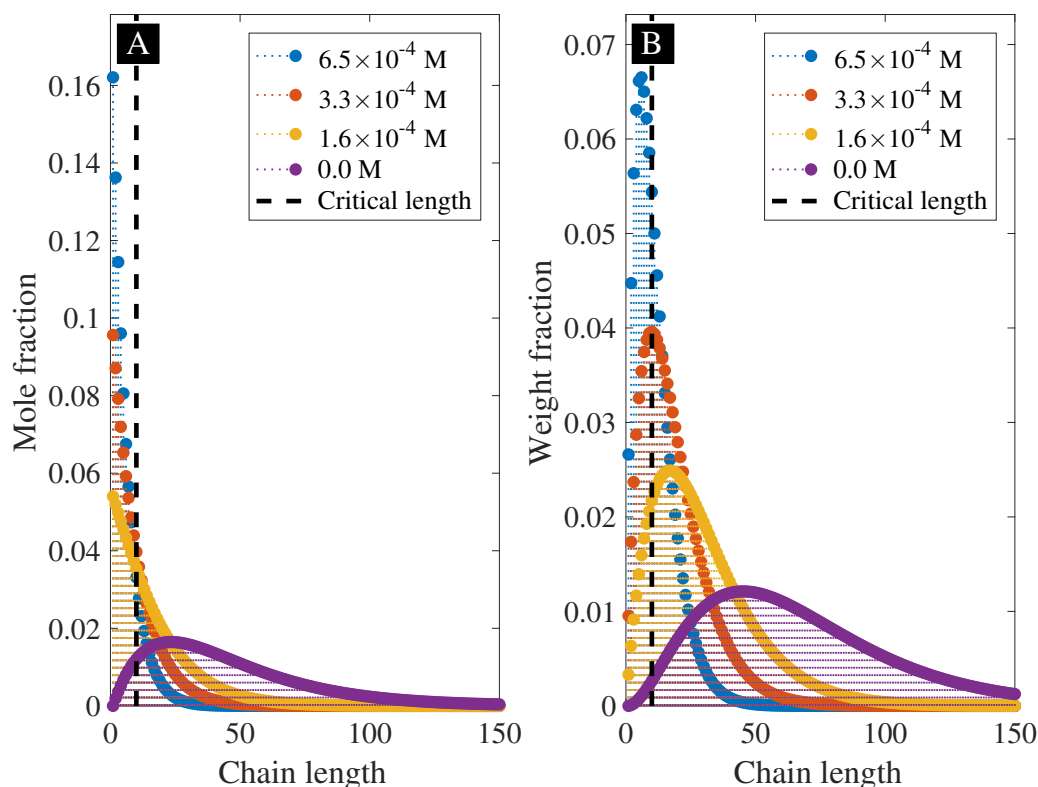


Figure 5.8: Effect of chain transfer agent on the total chain length distribution. Distributions were calculated with parameters used for Figure 5.7 C, F and I. **A:** Mole fractions. **B:** Weight fractions. Increasing the ME concentration (inset) leads to rapid increase in short chains as termination mechanism changes from coupling to termination by chain transfer. Short chains with initiator fragments can be excluded from the primary aggregates, which leads to lower surface charge density of the aggregates.

excluded short chains were however started by charged initiator fragments, and their exclusion leads to decrease in the surface charge of the collapsed globules. The shape of the experimental data is qualitatively reproduced in Figure 5.7 G, including the differing volume growth rates between ME and non-ME batches.

Constant ME concentration regardless of NIPAM concentration results in a considerable intercept term at low NIPAM regime and excessive use of ME (in this case ME concentration of $6.5 \times 10^{-4} \text{ mol dm}^{-3}$) in the reaction mixture leads to destabilization and aggregation of particles (Figure 5.7 B). Proportionally larger volume increase at low NIPAM concentration is due to the surface charge density of globules decreasing rapidly in the limit of zero NIPAM, where ME-to-NIPAM ratio increases rapidly (Figure 5.7 E). Inverting the surface charge density data leads to a vertical shift to higher volume in the calculated final particle volume

data in Figure 5.7 H, similar to that of experimentally observed behavior.

Finally, variation of only the ME concentration in the batch further highlights the strong effect of the ME; $4.4 \times 10^{-4} \text{ mol dm}^{-3}$ of ME in the batch results in approximately six fold increase in the final particle volume in collapsed state in Figure 5.7 C. This is due to non-linear decrease in the globule surface charge density (Figure 5.7 F). Again, the experimental data is qualitatively reproduced in Figure 5.7 I.

The fact that the same theoretical framework can reproduce the experimental data qualitatively when four independent reaction parameters are varied (monomer, initiator and ME concentration, as well as reaction temperature) is a strong indication that the chain length dependent surface charge density of the monochain globules and charge exclusion at the nucleation phase are indeed important factors for the particle number density in precipitation polymerization.

A side effect of ME modulated synthesis is the fact that chains become so short that it is difficult to exceed the gel point in the particles, i.e., the particles redisperse upon cooling below VPTT. Cross-linking density in the particles can be increased by increasing the concentration of an additional cross-linker such as N,N'-methylenebisacrylamide (BIS), but this proved unfeasible: BIS decreases the particle number density,^[32] which led to excessive aggregation of the particles during the synthesis when ME was present in the reaction mixture. Also using KPS to induce cross-links to particles^[13,17] did not lead to particles stable below VPTT. Therefore ME modulated synthesis serves as a good model system for investigating the particle nucleation, but is not a practical method to increase the microgel size.

5.5 Conclusions

In this work PNIPAM particle volume was shown to scale with monomer and initiator concentration according to $\bar{V}_p \propto [\text{M}]^{5/3} [\text{I}]^{-4/3}$ under two key assumptions: The particle number density in the batch is proportional to the initiation rate and surface charge density of monochain globules generated during the nucleation phase. Deviations from the scaling laws in the low monomer concentration regime and in the presence chain transfer agent could be qualitatively explained by recognizing that only chains longer than the critical length for coil-to-globule transition contribute to the nucleation process.

Using these principles, we showed that PNIPAM particle size could be tuned over a considerable range by varying monomer, initiator and chain transfer agent concentrations and reaction temperature. The measured particle volume was found to agree well with the derived power law dependencies in respect to monomer and initiator concentration. Experiment showed that the scaling law for the particle

volume was valid between 0 to 5 mol – % of crosslinker.

Our results highlight PNIPAM as a well-behaving model system, which can provide more insight into the fundamental mechanism of precipitation polymerization of thermoresponsive polymers. The most important reaction phase is the particle nucleation, which was found to follow radical solution polymerization kinetics.

The ideas presented here are not specific to PNIPAM, but further work is necessary to confirm whether these principles are generally applicable to other systems. The tangible benefits of the framework presented here include e.g. reduction of microgel size to a range suitable for drug delivery applications without the use of additional surfactants. Furthermore, the recent progress in realization of interesting new hollow-like PNIPAM particle architectures^[10,11,12,14,15,17,40], and their use in biomimetic applications necessitates robust control over particle size.

5.6 Supporting information

5.6.1 Flory-Schulz distributions in presence of chain transfer agent

The derivation presented here follows that of Flory,^[41,38,36] but takes also the effect of chain transfer into account.

Mole and weight fractions in radical chain polymerization

Consider a short period Δt early in the reaction, during which the reactant composition doesn't significantly change. During this time several reactions take place: new active centers are generated by the initiator, monomer is added to the propagating centers, and active centers are destroyed by coupling with other active centers or by chain transfer reactions, which immediately regenerate the center but stop the previous chain growth. Rate of these reactions are given by the well known rate equations

$$R_i = 2k_i f [I] \quad (5.12)$$

$$R_p = -\frac{d[M]}{dt} = k_p [M] [M\cdot] \quad (5.13)$$

$$R_{tr} = -\frac{d[CTA]}{dt} = k_{tr} [CTA] [M\cdot] \quad (5.14)$$

$$R_c = 2k_c [M\cdot] [M\cdot] \quad (5.15)$$

Here i , p , tr and c stand for initiation, propagation, transfer and chain coupling, respectively. $[I]$, $[M]$, $[M\cdot]$ and $[CTA]$ indicate the initiator, monomer, propagating radical and transfer agent concentrations, k are the corresponding rate constants and f the initiator efficiency. Assuming steady-state conditions, i.e.,

$$\frac{d[M\cdot]}{dt} = R_i - R_c = 0 \quad (5.16)$$

the number of events during the time Δt are given by

$$N_i = N_c = R_c \Delta t \quad (5.17)$$

$$N_p = R_p \Delta t \quad (5.18)$$

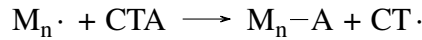
$$N_{tr} = R_{tr} \Delta t \quad (5.19)$$

In the case that one could reach to the reactor after Δt and take a closer look at the chains formed, five different types of molecules would be found. These

Supporting Table 5.2: Structure of species formed in radical chain polymerization in the presence of chain transfer agent. I denotes an initiator fragment, CT a reinitiating chain transfer agent fragment, A the atom or fragment transferred and x the number units in the chain, including the initiating fragments.

Designation	Structure	Chain length	No. of kinetic chains
1	$I-M_{x-1}-A$	x	1
2	$CT-M_{x-1}-A$	x	1
3	$I-M_{x-2}-I$	x	2
4	$I-M_{x-2}-CT$	x	2
5	$CT-M_{x-2}-CT$	x	2

are shown in Supporting Table 5.2. Type 1 molecules are initiated by an initiator fragment and terminated by a chain transfer reaction whereas type 2 molecules are initiated by a chain transfer agent fragment and terminated by a chain transfer reaction. The transfer reaction can be depicted as



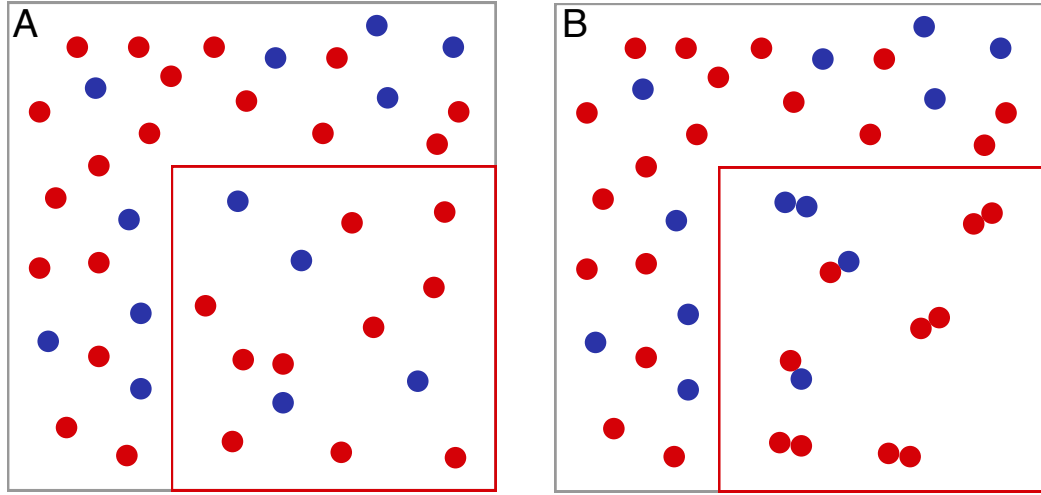
where a chain transfer agent CTA transfers an atom or fragment A to the active n -mer $M_n \cdot$ terminating the chain growth and becomes an active fragment $CT \cdot$, which can start a new chain growth.

Type 3 to 5 molecules are the molecules that are formed by coupling of chains initiated by initiator or chain transfer agent fragments. Type 3 to 5 molecules are each formed from two kinetic chains, which were started either by a chain transfer agent fragment or an initiator fragment. Fractions of kinetic chains and their combination are depicted in Supporting Figure 5.9.

Let us take a closer look into the mole fractions of each type of molecules in Supporting Table 5.2. In the limit of large number of molecules the mole fraction of each type corresponds to the probability that such a molecule is formed, which furthermore corresponds to the probability that we pick one type of molecule from the mixture of all formed molecules at random. The number of kinetic chains formed during Δt equals the number of growing radicals destroyed. This is given by

$$N_v = N_c + N_{tr} \quad (5.20)$$

This, however, is not the total number molecules formed during Δt , which we need to determine the probabilities. The total number of molecules is given by



Supporting Figure 5.9: Kinetic chains formed in polymerization during Δt . Red and blue circles denote kinetic chains started by a transfer agent fraction and an initiator fragment, respectively. Red square marks the fraction of kinetic chains that are terminated by coupling. **A:** All kinetic chains. **B:** The actual molecules obtained.

$$N = \frac{N_c}{2} + N_{tr} \quad (5.21)$$

because for a molecule to form, one radical has to be destroyed by transfer or two radicals by combination. If we reach into a reactor depicted in Supporting Figure 5.9 B, the probabilities to obtain a transfer terminated molecule and a combined molecules are

$$n_{tr} = \frac{N_{tr}}{N_{tr} + N_c/2} = \frac{2p_{tr}}{1 + p_{tr}} \quad (5.22)$$

$$n_c = \frac{N_c/2}{N_{tr} + N_c/2} = \frac{1 - p_{tr}}{1 + p_{tr}} \quad (5.23)$$

respectively. Here p_{tr} is the fraction of all radicals destroyed by transfer.

$$p_{tr} = \frac{N_{tr}}{N_{tr} + N_c} \quad (5.24)$$

Every chain transfer reaction not only destroys a radical but also creates a new one. Therefore any chain can be started by an initiator fragment or a chain transfer agent fragment. Probability that a chain is started by a transfer agent fragment is the fraction of transfer events $p_{i,tr}$ from all events that generate an active center

$$p_{i,tr} = \frac{N_{tr}}{N_{tr} + N_i} \quad (5.25)$$

where subindex i stands for initiation. Under steady-state kinetics the number of radicals created and destroyed by initiation and combination, however, are the same and therefore the mole fractions of kinetic chains started by transfer agent fragment and initiator fragment p_i are

$$p_{i,tr} = \frac{N_{tr}}{N_{tr} + N_c} = p_{tr} \quad (5.26)$$

$$p_i = 1 - p_{i,tr} = 1 - p_{tr} \quad (5.27)$$

Because Equations 5.26 and 5.27 apply to all the kinetic chains in general, the fractions of kinetic chains started by transfer and initiator are the same for the both populations of transfer terminated (outside the red box) and combined (inside the red box) molecules in Supporting Figure 5.9.

We now have the tools to calculate the probabilities for species 1 and 2 in Supporting Table 5.2 but species 3 to 5 require further consideration. For the combined molecules there are three end group possibilities. The probability to pick any one combination at random from $N_c/2$ possibilities is the number of ways one can build this combination from N_c kinetic chains divided by the number of ways one can build any combination from N_c kinetic chains. In our parlance of red (R, transfer started) and blue (B, initiator started) circles this is

$$P(RR) = \frac{\text{All the possible combinations RR from R distinct entities}}{\text{All the possible combinations of two from R + B distinct entities}}$$

$$P(BB) = \frac{\text{All the possible combinations BB from B distinct entities}}{\text{All the possible combinations of two from R + B distinct entities}}$$

$$P(RB) = \frac{\text{All the possible combinations RB from R + B distinct entities}}{\text{All the possible combinations of two from R + B distinct entities}}$$

These values are given by

$$P(RR) = \frac{\binom{N_R}{2}}{\binom{N_R+N_B}{2}} = \frac{N_R(N_R-1)}{(N_R+N_B-1)(N_R+N_B)} = \frac{p_{tr}(p_{tr}N_c-1)}{N_c-1} \quad (5.28)$$

$$\begin{aligned} P(BB) &= \frac{\binom{N_B}{2}}{\binom{N_R+N_B}{2}} = \frac{N_B(N_B-1)}{(N_R+N_B-1)(N_R+N_B)} \\ &= \frac{(1-p_{tr})((1-p_{tr})N_c-1)}{N_c-1} \end{aligned} \quad (5.29)$$

$$P(RB) = \frac{N_R \cdot N_B}{\binom{N_R+N_B}{2}} = \frac{2N_R \cdot N_B}{(N_R+N_B-1)(N_R+N_B)} = \frac{2p_{tr}(1-p_{tr})N_c}{N_c-1} \quad (5.30)$$

The binomial coefficient is given by

$$\binom{n}{k} = \frac{n!}{k!(n-k)!} \quad (5.31)$$

and we use the fact that $N_R + N_B = N_c$ (total number of kinetic chains ended by combination) and $N_R = p_{tr}N_c$ and $N_B = (1-p_{tr})N_c$, based on the argumentation regarding Equations 5.26 and 5.27.

The Equations 5.28 to 5.30 simplify even further when we note that

$$\lim_{N_c \rightarrow \infty} P(RR) = p_{tr}^2 \quad (5.32)$$

$$\lim_{N_c \rightarrow \infty} P(BB) = (1-p_{tr})^2 \quad (5.33)$$

$$\lim_{N_c \rightarrow \infty} P(RB) = 2p_{tr}(1-p_{tr}) \quad (5.34)$$

which should be applicable to the system at hand as the number of kinetic chains terminated by transfer is large as in any molecular system. The mole fractions of all the species 1 to 5 can be calculated by combining Equations 5.22, 5.23, 5.26, 5.27 and 5.32 - 5.34 in appropriate manner.

$$n_1 = \frac{2p_{tr}(1-p_{tr})}{1+p_{tr}} \quad (5.35)$$

$$n_2 = \frac{2p_{tr}^2}{1+p_{tr}} \quad (5.36)$$

$$n_3 = \frac{(1-p_{tr})^3}{1+p_{tr}} \quad (5.37)$$

$$n_4 = \frac{2p_{tr}(1-p_{tr})^2}{1+p_{tr}} \quad (5.38)$$

$$n_5 = \frac{p_{tr}^2(1-p_{tr})}{1+p_{tr}} \quad (5.39)$$

Equations 5.35 to 5.39 give the mole fractions of chains with certain end groups but don't say anything about the number of units x in the chain. In the case we adopt the principle of equal reactivity for simplicity, i.e., all the radicals have equal reactivity regardless of their size, then any given propagating center has a probability p to add a further monomer or probability $1-p$ to terminate either by transfer or combination. The probability tree to illustrate this process is given in Supporting Figure 5.10.

The probability p is given by the fraction of propagation steps of all the possible steps that the propagating center can take, i.e., propagate, terminate by transfer or combine

$$p = \frac{N_p}{N_p + N_c + N_{tr}} \quad (5.40)$$

The total probability for the chain propagation to stop is

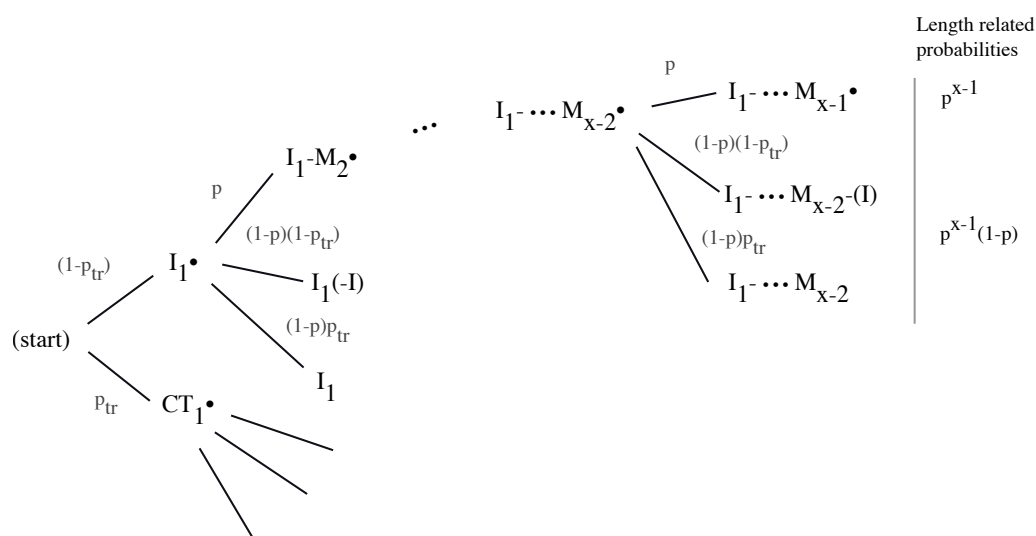
$$1-p = \frac{N_c + N_{tr}}{N_p + N_c + N_{tr}} \quad (5.41)$$

and individually

$$(1-p)(1-p_{tr}) = \frac{N_c}{N_p + N_c + N_{tr}} \quad (5.42)$$

$$(1-p)p_{tr} = \frac{N_{tr}}{N_p + N_c + N_{tr}} \quad (5.43)$$

From the probability tree in Supporting Figure 5.10 we see that *within each population of kinetic chains* (i.e. kinetic chains with different initiation and termination modes) the probability to obtain an x -mer is the same $p^{x-1}(p-1)$. The



Supporting Figure 5.10: Probability tree for radical chain polymerization in the presence of chain transfer agent. The probabilities that the chain is initiated by initiator or chain transfer agent fragments are $1 - p_{tr}$ and p_{tr} , respectively. Due to assumption of equal reactivity of the propagating centers regardless of length, the probability that the propagating center adds a monomer is p and the probabilities that the chain terminates by combination or transfer $(1 - p)(1 - p_{tr})$ and $(1 - p)p_{tr}$, respectively. Within each population of kinetic chains, the probability to obtain a chain of exactly x units is $p^{x-1}(1 - p)$, because in a chain of x units there have been $x - 1$ propagation steps, each with probability p , and one termination step with probability $(1 - p)$.

difference between the populations is only the relative amounts of chains determined by the starting modes $(1 - p_{tr})$ and p_{tr} and the termination modes $(1 - p_{tr})$ and p_{tr} . Therefore the length distribution in each population has the same shape and the probabilities of obtaining a kinetic x -mer of certain length is decoupled from its starting and termination modes.

The probability that a molecule that consists of one kinetic chain (species 1 and 2) has x units is therefore $p^{x-1}(1 - p)$. When accounting for an x -mer that has formed by combination, we have to recognize that the x -mer consists of a y - and z -mer with $y + z = x$, which can be combined in

$$\begin{array}{llll}
 1 & & I_1 \cdot & + \cdot M_{z-1} \cdots -M_3 + M_2 - I_1 \\
 2 & & I_1 - M_2 \cdot & + \cdot M_{z-2} \cdots -M_3 + M_2 - I_1 \\
 3 & & I_1 - M_2 - M_3 \cdot & + \cdot M_{z-3} \cdots -M_3 + M_2 - I_1 \\
 \cdot & & & \cdot \\
 \cdot & & & \cdot \\
 \cdot & & & \cdot \\
 x-3 & I_1 - M_2 - M_3 \cdots M_{y-3} \cdot & + & \cdot M_3 - M_2 - I_1 \\
 x-2 & I_1 - M_2 - M_3 \cdots M_{y-2} \cdot & + & \cdot M_2 - I_1 \\
 x-1 & I_1 - M_2 - M_3 \cdots M_{y-1} \cdot & + & \cdot I_1
 \end{array}$$

$(x - 1)$ ways. The probability that a combined molecule has x units is therefore

$$(x - 1)p^{y-1}(1 - p)p^{z-1}(1 - p) = (x - 1)p^{x-2}(1 - p)^2 \quad (5.44)$$

Combining these results with the analysis of mole fractions of the species 1 to 5, the mole fractions of x -mers of all species are given by

$$n_{x,1} = \frac{2p_{tr}(1 - p_{tr})}{1 + p_{tr}}(1 - p)p^{x-1} \quad (5.45)$$

$$n_{x,2} = \frac{2p_{tr}^2}{1 + p_{tr}}(1 - p)p^{x-1} \quad (5.46)$$

$$n_{x,3} = \frac{(1 - p_{tr})^3}{1 + p_{tr}}(1 - p)^2(x - 1)p^{x-2} \quad (5.47)$$

$$n_{x,4} = \frac{2p_{tr}(1 - p_{tr})^2}{1 + p_{tr}}(1 - p)^2(x - 1)p^{x-2} \quad (5.48)$$

$$n_{x,5} = \frac{p_{tr}^2(1 - p_{tr})}{1 + p_{tr}}(1 - p)^2(x - 1)p^{x-2} \quad (5.49)$$

The weight fractions are given by

$$w_x = \frac{xn_x N}{\sum_{x=1}^{\infty} xn_x N} = \frac{xn_x}{\sum_{x=1}^{\infty} xn_x} \quad (5.50)$$

where N is the total number of molecules. The sum in the denominator evaluates to

$$\begin{aligned} \sum_{x=1}^{\infty} xn_x &= \sum_{x=1}^{\infty} xn_{x,1} + \sum_{x=1}^{\infty} xn_{x,2} + \sum_{x=1}^{\infty} xn_{x,3} + \sum_{x=1}^{\infty} xn_{x,4} + \sum_{x=1}^{\infty} xn_{x,5} \\ &= \frac{2}{(1 + p_{tr})(1 - p)} \end{aligned} \quad (5.51)$$

when using sums

$$\sum_{x=1}^{\infty} xp^{x-1} = \frac{1}{(1 - p)^2} \quad (5.52)$$

$$\sum_{x=1}^{\infty} x(x-1)p^{x-2} = \frac{2}{(1 - p)^3} \quad (5.53)$$

to evaluate the individual sums for Equations 5.45 to 5.49. Using Equation 5.50 for every mole fraction of species 1 to 5 then gives

$$w_{x,1} = p_{tr}(1 - p_{tr})(1 - p)^2 xp^{x-1} \quad (5.54)$$

$$w_{x,2} = p_{tr}^2(1 - p)^2 xp^{x-1} \quad (5.55)$$

$$w_{x,3} = \frac{(1 - p_{tr})^3}{2}(1 - p)^3 x(x-1)p^{x-2} \quad (5.56)$$

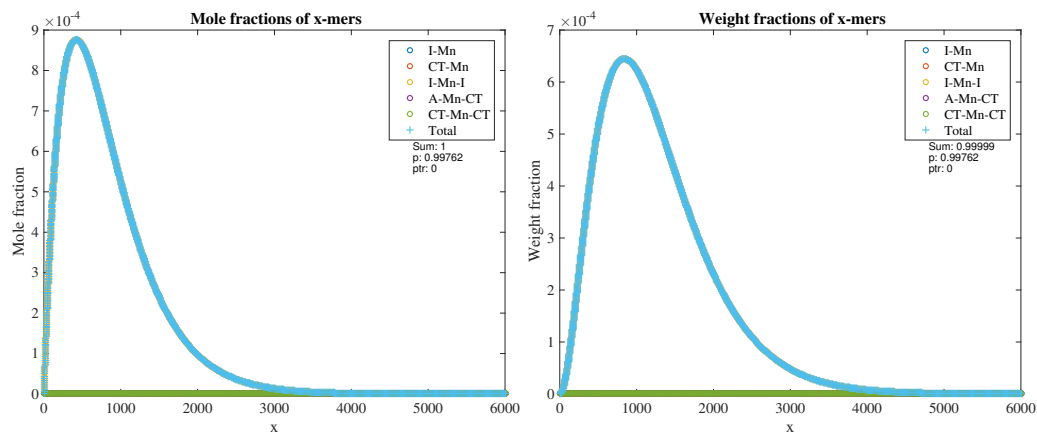
$$w_{x,4} = p_{tr}(1 - p_{tr})^2(1 - p)^3 x(x-1)p^{x-2} \quad (5.57)$$

$$w_{x,5} = \frac{p_{tr}^2(1 - p_{tr})}{2}(1 - p)^3 x(x-1)p^{x-2} \quad (5.58)$$

Calculated examples for mole and weight fractions

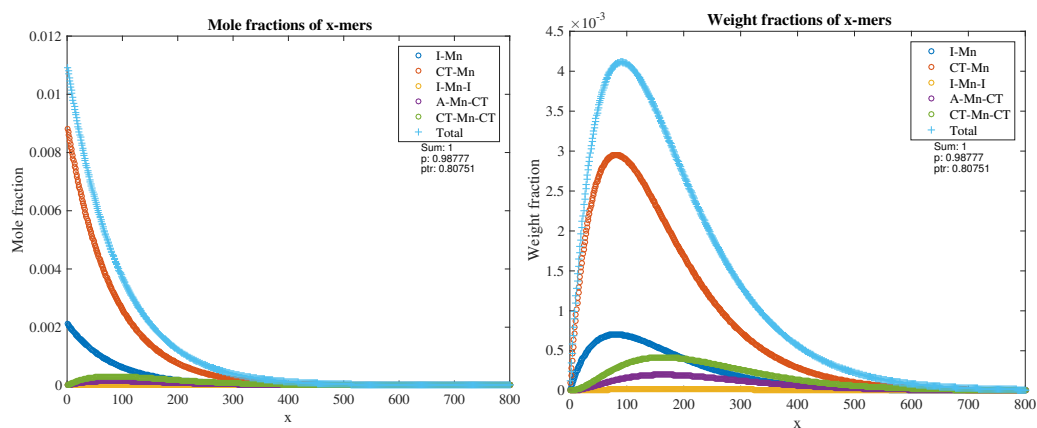
The reaction parameters for methacrylate photopolymerization from Odian^[36] were used to calculate the effect of chain transfer agent on the mole and weight fractions of the product in Δt . These are given in Supporting Table 5.3. These values were used to calculate the values for p and p_{tr} used in Equations 5.45 to 5.49 and 5.54 to 5.58.

The mole and weight fractions for reaction without chain transfer agent is shown in Supporting Figure 5.11. No other product is formed except combined



(a) Mole fractions of species 1-5, no transfer. (b) Weight fractions of species 1-5, no transfer.

Supporting Figure 5.11: Mole and weight fractions of species 1-5 when no transfer agent is used. $p = 0.9976$, $p_{tr} = 0$. Only combined species 3 is present.



(a) Mole fractions of species 1-5, transfer. (b) Weight fractions of species 1-5, transfer.

Supporting Figure 5.12: Mole and weight fractions of species 1-5 when agent is used. $p = 0.9878$, $p_{tr} = 0.8075$ with $C_{tr} = 20$ and $[CT] = 1 \times 10^{-4} \text{ mol} \cdot \text{dm}^{-3}$. Chain length is greatly shortened. Transfer terminated short species dominate the mole fractions. Also the weight fractions are dominated by the transfer terminated product, but the shortest product contributes less to the weight fraction.

Supporting Table 5.3: Reaction parameters for methacrylate photopolymerization given in Odian.

Quantity	Values	Units
k_p	7.96×10^2	$\text{dm}^3 \text{mol}^{-1} \text{s}^{-1}$
k_c	8.25×10^6	$\text{dm}^3 \text{mol}^{-1} \text{s}^{-1}$
C_{tr}	Adjusted	$\text{dm}^3 \text{mol}^{-1} \text{s}^{-1}$
[CT]	Adjusted	mol dm^{-3}
[M]	0.20	mol dm^{-3}
[R·]	2.30×10^{-8}	mol dm^{-3}

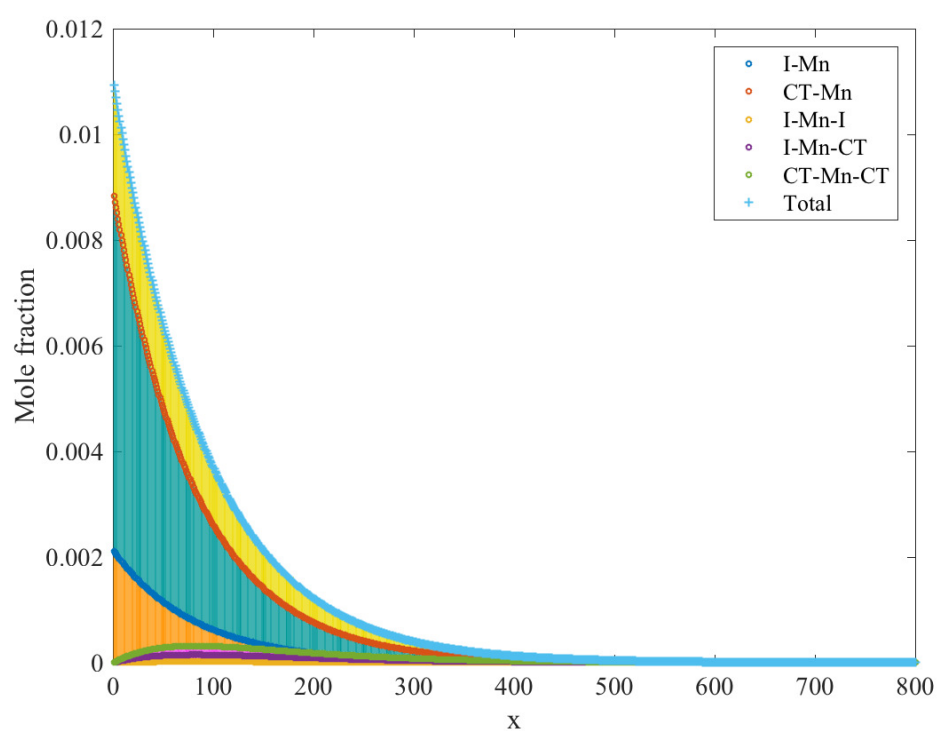
chains. As is seen in Supporting Figure 5.11b, the longer product contributes more to the weight fraction, shifting the distribution function to the direction of longer chains.

The picture changes drastically if chain transfer agent is present in the reaction mixture. The mole and weight fractions for this sort of reaction are shown in Supporting Figure 5.12. Here $C_{tr} = 20$, and $[\text{CT}] = 1 \times 10^{-4} \text{mol dm}^{-3}$. Even though p goes down from 0.9976 only to 0.9878, the p_{tr} rises to 0.8075 meaning that most of the kinetic chains are terminated by transfer instead of combination. This leads to drastic shortening of the chains so that short transfer terminated chains dominate the mole fraction as seen in Supporting Figure 5.12a. Some of the chains are very short chains that are unlikely to go through coil-to-globule transition. These species however dominate the mole fraction of the product, which would lead to the assumption of polymer charge density decreasing as these chains are excluded from the collapsed polymer particles.

Comparison with simulation

The validity of the closed form expressions were tested by comparing the calculated mole fractions with those obtained by simulating the probability tree in Supporting Figure 5.10. This essentially means that computer comes up with a random number, which is compared with the probability of propagation. If the number is smaller than the probability, the kinetic chain adds an unit, and if not, the chain is terminated. The mode of termination is decided by comparing the random number with the probability of termination by transfer or combination in a similar manner as with propagation. This process is repeated until the chain terminates and then a new kinetic chain is started.

Supporting Figure 5.13 shows the result for simulation of two million kinetic chains with $p = 0.9976$ and $p_{tr} = 0.8075$. The bar charts represent the result from



Supporting Figure 5.13: Comparison of calculated mole fractions and simulated result. The scatter plots represent the values calculated from the closed form expressions and the bar charts the simulated result of 2 million kinetic chains.

simulation and the scatter plots the calculated mole fractions. As can be seen the bar charts align well with the calculated values, which indicates that the closed form expressions represent the probability tree in Supporting Figure 5.10 accurately. This naturally says nothing about the fact whether the said probability tree is a reasonable description of the polymerization system.

Charge density of polymer and monomer loss due to transfer

In the case of precipitation polymerization of NIPAM we are interested in the average surface charge density of single chain globules given that there is some critical chain length x_c , which is required for the chains to contribute to the charge density. This is given by equation

$$\bar{\rho}_A = \frac{\sum_{x=x_c}^{\infty} z n_x}{(v_0 \sum_{x=x_c}^{\infty} (x-k) n_x)^{2/3}} \quad (5.59)$$

where v_0 is the volume occupied by one repeating unit, z is the charge number of the x -mer and k is 1 for species 1 and 2 and 2 for species 3-5 because we want to exclude the contribution of chain ends to the number of repeating units. Accounting for the different types of molecules we get

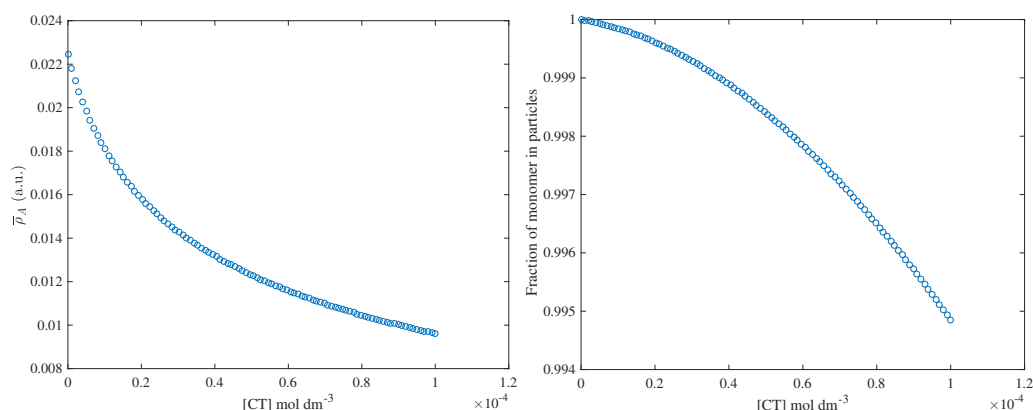
$$\bar{\rho}_A \propto \frac{\sum_{x=x_c+1}^{\infty} 1 \cdot n_{x,1} + \sum_{x=x_c+2}^{\infty} 2 \cdot n_{x,3} + \sum_{x=x_c+2}^{\infty} 1 \cdot n_{x,4}}{(\sum_{x=x_c+1}^{\infty} (x-1) n_{x,1} + \sum_{x=x_c+1}^{\infty} (x-1) n_{x,2} + \sum_{x=x_c+2}^{\infty} (x-2) n_{x,3} + \sum_{x=x_c+2}^{\infty} (x-2) n_{x,4} + \sum_{x=x_c+2}^{\infty} (x-2) n_{x,5})^{2/3}} \quad (5.60)$$

Chains that have lower number of repeating units than some critical value x_c , are assumed not to undergo a coil-to-globule transition and are therefore excluded from the particles. We can estimate the significance of this process by calculating the fraction of monomer units that actually end up in the particles

$$\Lambda = \frac{\sum_{x=x_c}^{\infty} (x-k) n_x N}{\sum_{x=1}^{\infty} (x-k) n_x N} \quad (5.61)$$

The limits of summation and k are appropriately modified for every type of species as in the case of Eq. 5.60.

An example of Eq. 5.60 is plotted in Supporting Figure 5.14a and of Eq. 5.61 in Supporting Figure 5.14b. Here the critical number of monomer units in the chain was chose to be 10 and the chain transfer agent concentration was varied from 0 to $2 \times 10^{-4} \text{ mol} \cdot \text{dm}^{-3}$ with reaction parameters of methacrylamide photopolymerization. As can be seen in Supporting Figure 5.14a the number of charges per polymerized monomer units in chains having more monomer units than 10 decreases with the chain transfer agent concentration. This should lead to less stabilization of precursor particles.

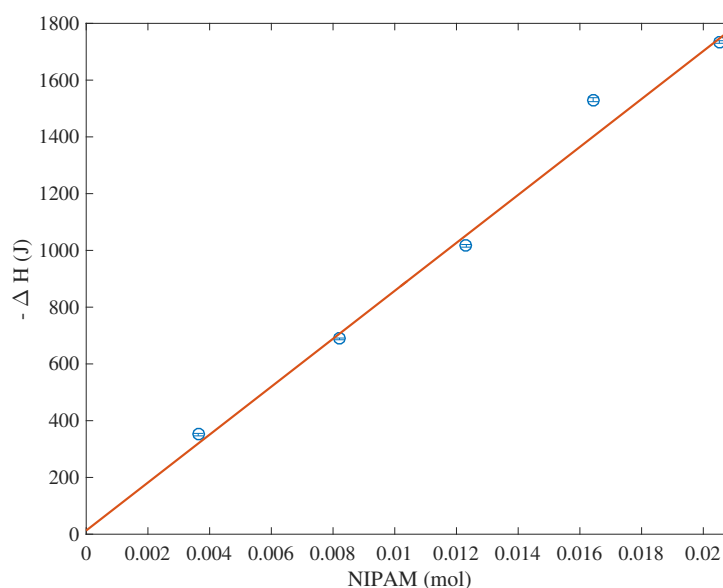


(a) Charge density of the polymer with concentration of chain transfer agent concentration. (b) Fraction of monomer, which ends up in particles with chain transfer agent concentration.

Supporting Figure 5.14: Charge density of polymer and monomer loss with chain transfer agent concentration. Reaction parameters are the same as before but $[CT]$ is varied between 0 and $2 \times 10^{-4} \text{ mol} \cdot \text{dm}^{-3}$. x_c was chosen to be 10.

Because not all the chains are expected to go through coil-to-globule transformation the particle volume might also decrease. This is demonstrated in Supporting Figure 5.14b. In the case no chain transfer agent is present virtually all monomer ends up in the product. When transfer agent is added, the fraction of monomer belonging to chains capable of coil-to-globule transition decreases gradually.

The reaction composition however changes during the polymerization, and detailed simulation is required to calculate the real loss of monomer due to chains not exceeding the critical chain length for collapse. One also has to consider the possibility of the locus of polymerization moving from the continuous phase to the particle surfaces in a later stage: The active centers on the particle surface during the growth phase can add monomer directly from the continuous phase and therefore circumvent the exclusion problem. Furthermore, peroxide initiators are known to create active sites to the polymer backbone^[13] to the extent that otherwise uncrosslinked particles gelate^[17]. It is a possibility that active sites in solubilized polymer and particle surface react so that the particles actually scavenge solubilized polymer from the continuous phase.



Supporting Figure 5.15: Reaction enthalpy with NIPAM concentration. The heat of polymerization of NIPAM was determined to be $84.5 \pm 0.3 \text{ kJ mol}^{-1}$ with intercept of $13 \pm 4 \text{ J}$

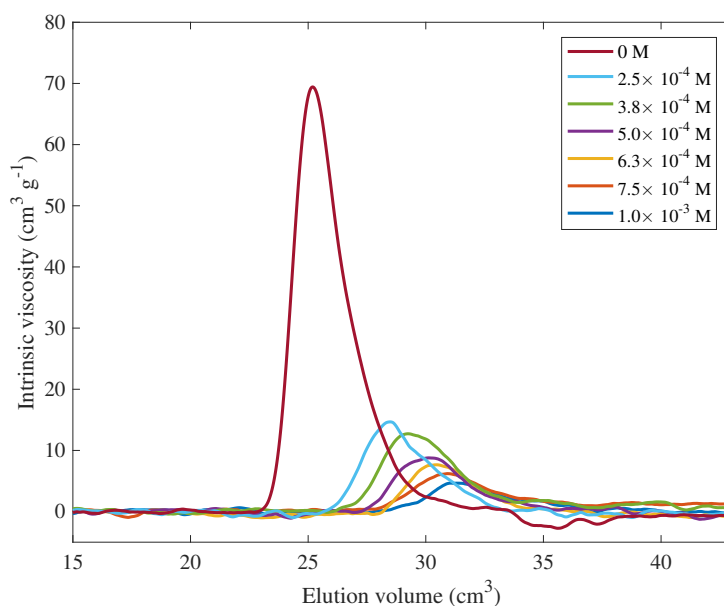
5.6.2 Experimental details

Heat of polymerization

Supporting Figure 5.15 shows reaction enthalpy with the amount of NIPAM. Reaction enthalpies were obtained by numerically integrating the traces shown in Figure 2A of the main paper. The heat of polymerization of NIPAM was determined to be $84.5 \pm 0.3 \text{ kJ mol}^{-1}$.

SEC characterization of 2-mercaptoethanol modulated polymerization

Supporting Figure 5.16 shows SEC eluograms of PNIPAM synthesized at room temperature in water in the presence of 2-mercaptoethanol (ME). The polymerization was carried out below the VPTT to minimize any branching reactions taking place in the collapsed particles at high polymer volume fraction, which would make the SEC analysis unfeasible. Even a small addition of ME results in a large drop in the intrinsic viscosity signal and a shift of the signal to higher retention volume. This corresponds to decrease in the molecular weight and confirms that ME acts as a chain transfer agent.



Supporting Figure 5.16: SEC eluograms for PNIPAM samples synthesized in the presence of 2-mercaptoethanol (ME). Significant drop in intrinsic viscosity and the shift of the signal to higher retention volume indicates that ME acts as a chain transfer agent. ME concentrations are given in the legend. NIPAM concentration was $8.1 \times 10^{-2} \text{ mol dm}^{-3}$, and APS and TEMED concentrations were $1.71 \times 10^{-3} \text{ mol dm}^{-3}$ and $1.81 \times 10^{-3} \text{ mol dm}^{-3}$, respectively, in every batch.

Parameters for Flory-Schulz calculations

According to the hypothesis presented in this paper the initiation rate during the nucleation phase sets the upper limit to the number of particles in the batch and the surface charge density of the primary globules determines to which extent they aggregate. That is, short chains, which form small globules, have high surface charge and aggregate less than longer chains. This is because each chain has 0 to 2 charged initiator fragments (depending on modes of initiation and termination), but variable number of repeating units. In other words, this simple model assumes that

$$\rho_p \propto R_i \cdot \bar{\rho}_A \propto R_i \cdot \frac{q}{A} \propto R_i \cdot \frac{q}{\bar{x}_c^{2/3}}$$

where ρ_p is number density of particles, R_i initiation rate during the nucleation phase, $\bar{\rho}_A$ average surface charge density of globules, q average number of charges per chain, A the average surface area of the primary globules and \bar{x}_c the average number of repeating units in chains that exceed the critical length for coil-to-

Supporting Table 5.4: Ranges of typical values of parameters in radical solution polymerization, values for methyl acrylate polymerization and the values used to generate the plots in the main article. Ranges and methyl acrylate values are taken from Odian^[36], section 3-8. Non-catalyzed potassium persulfate (KPS) dissociation constants are from Kolthoff and Miller^[42]. Here k_p is rate constant of propagation, E_p activation energy of propagation, k_t rate constant of coupling, E_t activation energy of coupling, k_d rate constant of initiator dissociation, $k_{d,\text{redox}}$ rate constant of initiator dissociation in redox system and c_s chain transfer constant.

Parameter	Units	Typical range	Methyl acrylate	Value used
k_p (60 °C)	$\text{dm}^3 \text{mol}^{-1} \text{s}^{-1}$	10^2 to 10^4	2.09×10^3	5.3×10^3
E_p	kJ mol^{-1}	16 to 25	29.7×10^3	29.7×10^3
k_t (60 °C)	$\text{dm}^3 \text{mol}^{-1} \text{s}^{-1}$	10^6 to 10^8	9.5×10^6	9.5×10^6
E_t	kJ mol^{-1}	1 to 23	22.2×10^3	22.2×10^3
KPS (non-catalyzed)				
k_d (50 °C)	s^{-1}	10^{-6} to 10^{-4}	1.6×10^{-6}	3.4×10^{-5}
k_d (60 °C)	s^{-1}	10^{-6} to 10^{-4}	5.0×10^{-6}	8.2×10^{-5}
k_d (70 °C)	s^{-1}	10^{-6} to 10^{-4}	1.4×10^{-5}	1.9×10^{-4}
k_d (80 °C)	s^{-1}	10^{-6} to 10^{-4}	3.9×10^{-5}	3.9×10^{-4}
$k_{d,\text{redox}}$ (60 °C)	$\text{dm}^3 \text{mol}^{-1} \text{s}^{-1}$	10^{-6} to 10^{-4}	10 to $1000 \times k_d$	$750 \times k_d$ (60 °C)
c_s (60 °C)	—	10^{-6} to 50	—	10

globule transition.

The first approximation for \bar{x}_c during the nucleation period under given experimental conditions can be obtained from Flory-Schulz distributions for radical chain polymerization. Some of the reaction parameters are set, such as reaction temperatures and reactant concentrations, others are unknown. The task is therefore to find a set of reaction parameters leading to n , that qualitatively reproduces characteristics of experimental final particle volume data. A requirement for the reaction parameters is that the values have to be within typical ranges reported for radical solution polymerization systems.

Reaction parameters for methyl acrylate polymerization compiled by Odian^[36] were used as the starting point; Odian also lists typical ranges for the parameters. These are shown in Supporting Table 5.4.

Methyl acrylate polymerization rate parameters were refined by a least squares procedure in order to find a possible set of parameters that would describe the experimental data acceptably. All the k_d parameters were free parameters; for k_p and k_t only the value at 60 °C was a free parameter. The values for other reaction temperatures were calculated by scaling with the corresponding activation energies (E_x) according to

$$k_x(T) = k(60^\circ\text{C}) \cdot \exp\left(\frac{E_x}{R} \left[\frac{1}{333.15\text{ K}} - \frac{1}{T}\right]\right)$$

where R is the gas constant. A small program was written to solve the optimization problem

$$\min_{\mathbf{x}} ||\bar{V}_{p,M,T} - \bar{V}_{p,M}(\mathbf{x})||_2^2$$

where $||\cdot||_2$ stands for vector 2-norm, $\bar{V}_{p,M,T}$ refers to average particle volume at monomer concentration $[M]$ and temperature T in Figure 4A of the main paper. Vector \mathbf{x} contains the model parameters and $\bar{V}_{p,M}(\mathbf{x})$ is the model expression for the average particle volume

$$\bar{V}_{p,M}(\mathbf{x}) = A \times \frac{[M]}{\bar{\rho}_{A,m,t} \cdot k_d(T)/k_d(50^\circ\text{C})}$$

The surface charge density is calculated from

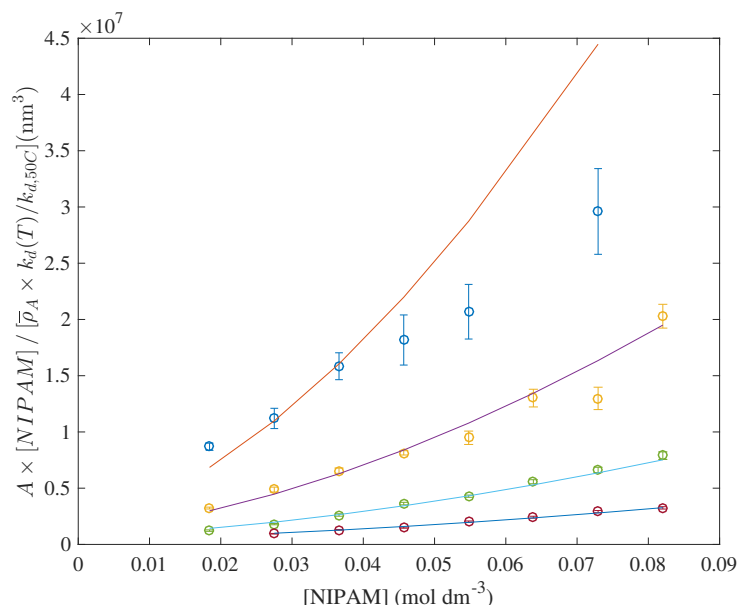
$$\bar{\rho}_A = \frac{\bar{n}_{xc,1} + 2\bar{n}_{xc,3} + \bar{n}_{xc,4}}{\bar{x}_{xc}^{2/3}}$$

with mole fractions as given in the main paper (Equations 3 to 7). Assuming that the charged fragments are located at the globule surface and that the globule density is constant, this expression is correct up to a constant factor ($v_0^{-2/3}$), see Eq. 2 in main paper). Constant A absorbs V_M , absolute particle number density n and other proportionality constants that were left out in the derivation of the scaling law. The parameter vector \mathbf{x} therefore contains

$$\mathbf{x} = [A \ k_p(60^\circ\text{C}) \ k_t(60^\circ\text{C}) \ k_d(50^\circ\text{C}) \ k_d(60^\circ\text{C}) \ k_d(70^\circ\text{C}) \ k_d(80^\circ\text{C})]$$

necessary to calculate the mole fractions from Flory-Schulz equations given in the manuscript. Rate constants for propagation (k_p) and termination (k_t) were scaled to other temperatures using the activation energies, as explained above. Depending on the initial guesses, one can find a local minimum so that the data fits approximately, as shown by Supporting Figure 5.17. The calculated result does agree with the largest particles well. This can be explained by the fact that the largest particles polymerized at 50°C start to sediment during the polymerization and the sample for the dynamic light scattering experiment can be taken only from the stable but smaller particles that remain dispersed in water.

The kinetic parameters obtained by least squares minimization are given in Supporting Table 5.4. One should not consider these values to be specific to NI-PAM polymerization per se; if the extent of aggregation of primary globules is



Supporting Figure 5.17: $\bar{V}_{p,M}(\mathbf{x})$, with \mathbf{x} determined by least squares procedure. The deviation of the largest particles is due to sedimentation during the polymerization, as explained in the text.

proportional to the charge density of polymer, this set is one set of parameters that produces polymer charge density capable of describing the experimental data qualitatively in the case of precipitation polymerization of NIPAM.

Some of the batches were initiated with potassium persulfate (KPS) and some by ammonium persulfate - N,N,N',N'-tetramethylethylenediamine (APS-TEMED) redox system. The dissociation constant for redox system is typically several orders of magnitude higher than that of the corresponding persulfate by thermal decomposition.^[36] Under certain circumstances, the use of redox initiation offers additional benefits beyond the fun factor. It is a property of APS-TEMED initiation that initiator induced cross-linking is greatly diminished,^[17] which is essential when the effect of initiation rate on particle number density is investigated. Presence of initiator induced cross-linking leads to decrease in the number of particles with increasing initiator concentration, whereas the opposite is observed when the additional cross-linking is suppressed.^[32] Furthermore, in situations where it is difficult to get rid of all the oxygen in the reaction medium (e.g. in calorimeter), the high initiation rate provided by redox initiator system helps to diminish any disturbances caused by trace amounts of oxygen.

5.6.3 Experimental data

The reactant compositions and hydrodynamic radii for all the batches featured in this work are listed in Supporting Tables 5.5 to 5.10 on the next pages. Data is organized based on the figures they appear in the main paper.

Supporting Table 5.5: Reaction parameters for KPS initiated batches at different temperatures. Horizontal lines denote batches that were polymerized simultaneously.

Figure	T (°C)	[NIPAM] (mmol dm ⁻³)	[KPS] (mmol dm ⁻³)	R_h (nm)	STD (nm)
4A	50	73.0	1.6	192	4
4A	50	54.8	1.6	170	3
4A	50	45.7	1.6	163	3
4A	50	36.6	1.6	156	2
4A	50	27.5	1.6	139	2
4A	50	18.4	1.6	127.5	0.8
4A	60	82	1.6	170	2
4A	60	73.0	1.6	146	2
4A	60	63.9	1.6	146	2
4A	60	54.8	1.6	131	1.4
4A	60	45.7	1.6	124.8	0.5
4A	60	36.6	1.6	116.1	0.7
4A	60	27.5	1.6	105.2	0.8
4A	60	18.4	1.6	91.7	0.4
4A	70	82	1.6	123.5	0.9
4A	70	73.0	1.6	116.5	0.7
4A	70	63.9	1.6	110.0	0.6
4A	70	54.8	1.6	100.8	0.4
4A	70	45.7	1.6	95.4	0.5
4A	70	36.6	1.6	85.5	0.6
4A	70	27.5	1.6	75.5	0.6
4A	70	18.4	1.6	66.4	0.6
4A	80	82	1.6	91.9	0.5
4A	80	73.0	1.6	88.6	0.5
4A	80	63.9	1.6	83.3	0.5
4A	80	54.8	1.6	78.5	0.4
4A	80	45.7	1.6	70.9	0.4
4A	80	36.6	1.6	67.6	0.3
4A	80	27.5	1.6	61.0	0.3

Supporting Table 5.6: Reaction parameters for APS-TEMED initiated batches with variable APS concentration. Horizontal lines denote batches that were polymerized simultaneously.

Figure	T (°C)	[APS] (mmol dm ⁻³)	[TEMED] (mmol dm ⁻³)	[NIPAM] (mmol dm ⁻³)	R_h (nm)	STD (nm)
4B	60	2.5	17	54.9	90.6	0.7
4B	60	2.2	17	54.9	92.1	0.7
4B	60	1.8	17	54.9	93.3	0.5
4B	60	1.5	17	54.9	96.4	0.8
4B	60	5.8	17	54.9	87.4	0.5
4B	60	5.0	17	54.9	88.0	0.6
4B	60	4.2	17	54.9	85.5	0.6
4B	60	3.3	17	54.9	89.1	0.5
4B	60	2.5	17	54.9	87.7	0.7
4B	60	1.7	17	54.9	90.9	0.8
4B	60	0.9	17	54.9	101.9	0.6
4B	60	0.6	17	54.9	108.2	0.5
4B	60	3.3	17	54.9	89.3	0.6
4B	60	2.9	17	54.9	92.0	0.6
4B	60	2.5	17	54.9	88.7	0.4
4B	60	2.2	17	54.9	91	0.6
4B	60	1.8	17	54.9	92.9	0.6
4B	60	1.4	17	54.9	96.6	0.5
4B	60	1.0	17	54.9	102	0.7
4B	60	0.6	17	54.9	120	0.7

Supporting Table 5.7: Reaction parameters for various N,N'-methylenebisacrylamide (BIS) batches. Horizontal lines denote batches that were polymerized simultaneously.

Figure	T (°C)	[NIPAM] (mmol dm ⁻³)	BIS (mol-%)	[KPS] (mmol dm ⁻³)	R_h (nm)	STD (nm)
6	70	104.4	0	1.6	180	1.3
6	70	86.8	0	1.6	161	1.2
6	70	77.0	0	1.6	147	1.1
6	70	63.9	0	1.6	132	1.1
6	70	49.6	0	1.6	117.7	0.9
6	70	9.1	0	1.6	56.0	0.4
6	70	95.3	0	1.6	174	2
6	70	82.2	0	1.6	151.7	0.6
6	70	70.5	0	1.6	145.3	0.6
6	70	56.1	0	1.6	121.8	0.5
6	70	43.1	0	1.6	104.8	0.5
6	70	29.4	0	1.6	93.7	0.2
6	70	25.7	0	1.6	71.4	0.3
6	70	5.2	0	1.6	64.3	0.4
6	70	83.5	0	1.6	156.6	0.5
6	70	69.4	0	1.6	136.9	0.9
6	70	61.6	0	1.6	129.7	0.5
6	70	51.1	0	1.6	115.5	0.3
6	70	39.7	0	1.6	103.0	0.4
6	70	29.2	0	1.6	89.3	0.7
6	70	17.8	0	1.6	75.9	0.2
6	70	7.3	0	1.6	53.9	0.9
6	70	104.4	1.0	1.6	180	2
6	70	86.8	1.0	1.6	166	2
6	70	77.0	1.0	1.6	149	2
6	70	63.9	1.0	1.6	136.2	0.9
6	70	49.6	1.0	1.6	124.0	0.8
6	70	36.5	1.0	1.6	108	0.4
6	70	22.2	1.0	1.6	87.4	0.2
6	70	9.1	1.0	1.6	56.3	0.4
6	70	104.4	2.5	1.6	197	5
6	70	86.8	2.5	1.6	177	1.4
6	70	77.0	2.5	1.6	163	2
6	70	63.9	2.5	1.6	153.8	1.2
6	70	49.6	2.5	1.6	135	0.6
6	70	36.5	2.5	1.6	117.6	0.6
6	70	22.2	2.5	1.6	94.6	0.4
6	70	9.1	2.5	1.6	66.1	0.6
6	70	104.4	5.0	1.6	203	2
6	70	86.8	5.0	1.6	187	4
6	70	77.0	5.0	1.6	179	1.5
6	70	63.9	5.0	1.6	160	1.3
6	70	49.6	5.0	1.6	142.9	0.9
6	70	36.5	5.0	1.6	121	0.3
6	70	22.2	5.0	1.6	100.8	0.6

Supporting Table 5.8: Reaction parameters for batches with constant NIPAM-to-2-mercaptoethanol (ME) ratio. Horizontal lines denote batches that were polymerized simultaneously.

Figure	T (°C)	[NIPAM] (mmoldm ⁻³)	[APS] (mmoldm ⁻³)	[TEMED] (mmoldm ⁻³)	[ME] (mmoldm ⁻³)	R_h (nm)	STD (nm)
7A	60	82.1	1.6	3.4	0	118.0	0.7
7A	60	72.9	1.6	3.4	0	113.7	1.4
7A	60	63.8	1.6	3.4	0	103.9	0.6
7A	60	54.8	1.6	3.4	0	98.4	0.6
7A	60	45.7	1.6	3.4	0	87.0	0.5
7A	60	36.5	1.6	3.4	0	82.6	0.6
7A	60	27.5	1.6	3.4	0	73.7	0.7
7A	60	18.4	1.6	3.4	0	65.7	0.4
7A	60	82.1	1.6	3.4	0.66	147	1.1
7A	60	72.9	1.6	3.4	0.58	136	1
7A	60	63.8	1.6	3.4	0.51	120.4	0.8
7A	60	54.8	1.6	3.4	0.44	113.7	0.6
7A	60	45.7	1.6	3.4	0.37	102.6	0.6
7A	60	36.5	1.6	3.4	0.29	88.8	0.5
7A	60	27.5	1.6	3.4	0.22	80.4	0.6
7A	60	18.4	1.6	3.4	0.15	71.5	0.5
7A	60	82.1	1.6	3.4	0.99	157	1.5
7A	60	72.9	1.6	3.4	0.88	151	1
7A	60	63.8	1.6	3.4	0.77	135	1
7A	60	54.8	1.6	3.4	0.66	124	1
7A	60	45.7	1.6	3.4	0.55	111.9	0.7
7A	60	36.5	1.6	3.4	0.44	93.1	0.4
7A	60	27.5	1.6	3.4	0.33	83.2	0.4
7A	60	18.4	1.6	3.4	0.22	72.8	0.5
7A	60	72.9	1.6	3.4	1.17	174	1
7A	60	63.8	1.6	3.4	1.0	165	2
7A	60	54.8	1.6	3.4	0.88	145	3
7A	60	36.5	1.6	3.4	0.59	118.9	0.8
7A	60	27.5	1.6	3.4	0.44	107.0	0.8
7A	60	18.4	1.6	3.4	0.29	89.6	0.6

Supporting Table 5.9: Reaction parameters for batches with constant 2-mercaptoethanol (ME) concentration. Horizontal lines denote batches that were polymerized simultaneously.

Figure	T (°C)	[NIPAM] (mmoldm ⁻³)	[APS] (mmoldm ⁻³)	[TEMED] (mmoldm ⁻³)	[ME] (mmoldm ⁻³)	R_h (nm)	STD (nm)
7B	60	82.1	1.6	3.4	0	118.0	0.7
7B	60	72.9	1.6	3.4	0	113.7	1.4
7B	60	63.8	1.6	3.4	0	103.9	0.6
7B	60	54.8	1.6	3.4	0	98.4	0.6
7B	60	45.7	1.6	3.4	0	87.0	0.5
7B	60	36.5	1.6	3.4	0	82.6	0.6
7B	60	27.5	1.6	3.4	0	73.7	0.7
7B	60	18.4	1.6	3.4	0	65.7	0.4
7B	60	82.1	1.6	3.4	0.16	126.3	0.5
7B	60	72.9	1.6	3.4	0.16	122.7	0.9
7B	60	63.8	1.6	3.4	0.16	121.5	0.6
7B	60	54.8	1.6	3.4	0.16	111.3	0.7
7B	60	45.7	1.6	3.4	0.16	106.1	0.6
7B	60	36.5	1.6	3.4	0.16	101.5	0.7
7B	60	27.5	1.6	3.4	0.16	100.7	0.6
7B	60	18.4	1.6	3.4	0.16	97.0	0.6
7B	60	82.1	1.6	3.4	0.33	145.0	0.8
7B	60	72.9	1.6	3.4	0.33	140	1
7B	60	63.8	1.6	3.4	0.33	138.4	0.8
7B	60	54.8	1.6	3.4	0.33	129.0	0.8
7B	60	45.7	1.6	3.4	0.33	124.1	0.6
7B	60	36.5	1.6	3.4	0.33	121.6	0.7
7B	60	27.5	1.6	3.4	0.33	120.3	0.7
7B	60	18.4	1.6	3.4	0.33	116.3	0.8
7B	60	63.8	1.6	3.4	0.65	173	3
7B	60	54.8	1.6	3.4	0.65	163	1.2
7B	60	45.7	1.6	3.4	0.65	167	3
7B	60	36.5	1.6	3.4	0.65	165	2
7B	60	27.5	1.6	3.4	0.65	179	2

Supporting Table 5.10: Reaction parameters for batches with constant NIPAM, APS and TEMED concentrations.

Figure	T (°C)	[NIPAM] (mmol dm ⁻³)	[APS] (mmol dm ⁻³)	[TEMED] (mmol dm ⁻³)	[ME] (mmol dm ⁻³)	R_h (nm)	STD (nm)
7C	60	36.5	7.8	0.86	0.44	140	1.2
7C	60	36.5	7.8	0.86	0.38	131.6	0.7
7C	60	36.5	7.8	0.86	0.31	127.7	0.7
7C	60	36.5	7.8	0.86	0.25	114.1	0.6
7C	60	36.5	7.8	0.86	0.19	105.9	0.5
7C	60	36.5	7.8	0.86	0.13	92.6	0.5
7C	60	36.5	7.8	0.86	0.63	90.3	0.6
7C	60	36.5	7.8	0.86	0	87.3	0.4

Bibliography

- [1] F. Alexis, E. Pridgen, L. K. Molnar and O. C. Farokhzad, *Mol. Pharmaceutics*, 2008, **5**, 505–515.
- [2] T. J. Merkel, S. W. Jones, K. P. Herlihy, F. R. Kersey, A. R. Shields, M. Napier, J. C. Luft, H. L. Wu, W. C. Zamboni, A. Z. Wang, J. E. Bear and J. M. DeSimone, *Proceedings of the National Academy of Sciences of the United States of America*, 2011, **108**, 586–591.
- [3] S. Schmidt, M. Zeiser, T. Hellweg, C. Duschl, A. Fery and H. Möhwald, *Adv. Funct. Mater.*, 2010, **20**, 3235–3243.
- [4] Y. Xia, X. He, M. Cao, C. Chen, H. Xu, F. Pan and J. R. Lu, *Biomacromolecules*, 2013, **14**, 3615–3625.
- [5] R. Pelton, *Advances in Colloid and Interface Science*, 2000, **85**, 1–33.
- [6] H. G. Schild, *Progress in Polymer Science*, 1992, **17**, 163–249.
- [7] E. S. Lee, Z. Gao and Y. H. Bae, *J Control Release*, 2008, **132**, 164–170.
- [8] T. Hoare and R. Pelton, *Macromolecules*, 2004, **37**, 2544–2550.
- [9] T. Hoare and R. Pelton, *Macromolecules*, 2007, **40**, 670–678.
- [10] V. Lapeyre, N. Renaudie, J.-F. Dechezelles, H. Saadaoui, S. Ravaine and V. Ravaine, *Langmuir*, 2009, **25**, 4659–4667.
- [11] J. Dubbert, T. Honold, J. S. Pedersen, A. Radulescu, M. Drechsler, M. Karg and W. Richtering, *Macromolecules*, 2014, **47**, 8700–8708.
- [12] R. Contreras-Cáceres, L. Schellkopf, C. Fernández-López, I. Pastoriza-Santos, J. Pérez-Juste and M. Stamm, *Langmuir*, 2015, **31**, 1142–1149.
- [13] J. Gao and B. J. Frisken, *Langmuir*, 2003, **19**, 5212–5216.
- [14] Z. Meng, M. H. Smith and L. A. Lyon, *Colloid and Polymer Science*, 2009, **287**, 277–285.
- [15] H. Bachman, A. C. Brown, K. C. Clarke, K. S. Dhada, A. Douglas, C. E. Hansen, E. Herman, J. S. Hyatt, P. Kodlekere, Z. Meng, S. Saxena, M. W. Spears Jr, N. Welsch and L. A. Lyon, *Soft Matter*, 2015, **11**, 2018–2028.
- [16] K. Geisel, A. A. Rudov, I. I. Potemkin and W. Richtering, *Langmuir*, 2015, **31**, 13145–13154.

- [17] O. L. J. Virtanen, A. Mourran, P. T. Pinard and W. Richtering, *Soft Matter*, 2016, **12**, 3919–3928.
- [18] A. C. Brown, S. E. Stabenfeldt, B. Ahn, R. T. Hannan, K. S. Dhada, E. S. Herman, V. Stefanelli, N. Guzzetta, A. Alexeev, W. A. Lam, L. A. Lyon and T. H. Barker, *Nat Mater*, 2014, **13**, 1108–1114.
- [19] N. M. B. Smeets and T. Hoare, *Journal of Polymer Science Part A Polymer Chemistry*, 2013, **51**, 3027–3043.
- [20] S. Pan, J. M. G. T. Torres, T. Hoare and R. Ghosh, *Journal of Membrane Science*, 2015, **479**, 141–147.
- [21] W. McPhee, K. C. Tam and R. Pelton, *Journal of Colloid and Interface Science*, 1993, **156**, 24–30.
- [22] D. C. Jones and L. A. Lyon, *Macromolecules*, 2000, **33**, 8301–8306.
- [23] T. López-León, J. L. Ortega-Vinuesa, D. Bastos-González and A. Elaïssari, *J. Phys. Chem. B*, 2006, **110**, 4629–4636.
- [24] D. Dupin, S. Fujii, S. P. Armes, P. Reeve and S. M. Baxter, *Langmuir*, 2006, **22**, 3381–3387.
- [25] A. Pich, S. Berger, O. Ornatsky, V. Baranov and M. A. Winnik, *Colloid and Polymer Science*, 2008, **287**, 269–275.
- [26] R. H. Pelton and P. Chibante, *Colloids and Surfaces*, 1986, **20**, 247–256.
- [27] X. Wu, R. H. Pelton, A. E. Hamielec, D. R. Woods and W. McPhee, *Colloid and Polymer Science*, 1994, **272**, 467–477.
- [28] W. V. Smith and R. H. Ewart, *The Journal of Chemical Physics*, 1948, **16**, 592–599.
- [29] D. Duracher, A. Elaïssari and C. Pichot, *Journal of Polymer Science Part A Polymer Chemistry*, 1999, **37**, 1823–1837.
- [30] F. Meunier, A. Elaïssari and C. Pichot, *Polymers for Advanced Technologies*, 1995, **6**, 489–496.
- [31] J. Gao and B. J. Frisken, *Langmuir*, 2003, **19**, 5217–5222.
- [32] O. L. J. Virtanen, H. M. Ala-Mutka and W. Richtering, *Macromol. Chem. Phys.*, 2015, **216**, 1431–1440.

- [33] R. Riesen, *Thermochimica Acta*, 1987, **119**, 219–222.
- [34] B. Grob and R. Riesen, *Thermochimica Acta*, 1987, **114**, 83–90.
- [35] W. Burchard and W. Richtering, *Progress in Polymer and Colloid Science*, 1989, **80**, 151–163.
- [36] G. Odian, *Principles of Polymerization*, Wiley Interscience, 4th edn, 2004.
- [37] O. L. J. Virtanen and W. Richtering, *Colloid and Polymer Science*, 2014, **292**, 1743–1756.
- [38] P. J. Flory, *Principles of Polymer Chemistry*, Cornell University Press, 1953.
- [39] M. Stieger, J. S. Pedersen, W. Richtering and P. Lindner, *Journal of Chemical Physics*, 2004, **120**, 6197–6206.
- [40] A. J. Schmid, J. Dubbert, A. A. Rudov, J. S. Pedersen, P. Lindner, M. Karg, I. I. Potemkin and W. Richtering, *Scientific Reports*, 2016, **6**, 1–13.
- [41] P. J. Flory, *Journal of the American Chemical Society*, 1936, **58**, 1877–1885.
- [42] I. M. Kolthoff and I. K. Miller, *Journal of American Chemical Society*, 1951, **73**, 3055–3059.

6. Particle concentration by *in situ* small-angle neutron scattering

6.1 Abstract

Poly(*N*-isopropylacrylamide) microgels have found various uses in fundamental polymer and colloid science as well as in applications. They are conveniently prepared by precipitation polymerization of *N*-isopropylacrylamide. In this reaction radical polymerization and colloidal stabilization intertwine and play together to produce well-defined thermosensitive particles of narrow size distribution. Here we have used small-angle neutron scattering in conjunction with a stopped-flow device to monitor the particle growth in precipitation polymerization *in situ*. The average particle volume growth is found to follow pseudo-first order kinetics, indicating that the polymerization rate is determined by the availability of unreacted monomer. Peroxide initiator induced cross-linking as well as bifunctional monomer are shown to decrease the particle number density in the batch. The results indicate the particles to form very early in the reaction, and their concentration to stay approximately the same thereafter. Overall reaction rate is found to be sensitive to monomer and initiator concentration in accordance to radical solution polymerization mechanism, supporting results from earlier work.

6.2 Introduction

Poly(*N*-isopropylacrylamide)^[1] (PNIPAM) is an archetypal example of a stimuli-sensitive smart polymer, characterized by its well-defined lower critical solution temperature (LCST) of approximately 32 °C^[2] in water. Radical polymerization of aqueous *N*-isopropylacrylamide (NIPAM) solution above LCST yields soft colloidal particles in the size range of tens of nanometers^[3] to few micron.^[4] These so-called microgels^[5,6] have a narrow size distribution, exhibit volume-

phase transition (VPT) at PNIPAM LCST and have found various uses for instance as emulsion stabilizers,^[7,8,9,10] drug carriers^[11,12,13] and in bioapplications.^[14,15,16,17]

The formation of stable particles of narrow size distribution^[18,19] in precipitation polymerization of NIPAM has been attributed to electrostatic stabilization by charged persulfate initiator fragments, which accumulate to the particles as a part of the radical polymerization process.^[20] The reaction condition dependent chain length has been proposed as the regulating mechanism for the number of stabilizing initiator fragments in the particles.^[21,22] Lately it has been shown that the principles of radical solution polymerization can be effectively used to regulate the stabilization and final particle volume of PNIPAM particles.^[23,24]

The narrow size distribution of particles implies that the particle nucleation takes place shortly after initiation and the number of particles stays approximately constant thereafter. The rapid growth of particles at typical reaction conditions^[25] makes characterization of particle formation and growth difficult. High flux small-angle neutron scattering (SANS) in combination with stopped-flow device for controlled initiation is an ideal tool to track particle and population properties *in situ*. In this work we employ SANS to investigate the effects of monomer, initiator and cross-linker concentration on the growth of PNIPAM particles in their native, undisturbed environment. Understanding the precipitation polymerization in detail is of fundamental interest to polymer chemists and physicists and helps to improve synthesis methods to customize the smart particles for their numerous applications.

6.3 Model expression for the scattered intensity

In a SANS experiment the average scattered intensity from a dispersion of particles is proportional to structure factor $S(q)$ and form factor $P(q)$

$$I(q) \propto S(q)P(q) \quad (6.1)$$

$P(q)$ contains spatially averaged information on the geometry and internal structure of the scatterers; $S(q)$ contributes to the intensity only when the particle positions are correlated. If the interparticle interactions are weak and/or the dispersion is sufficiently dilute, particle positions in the scattering volume are uncorrelated and $S(q) \rightarrow 1$. We shall see that this is the case in the current work.

Then for a collection of n_p particles dispersed in scattering volume V_{sc} at nominal scattering vector magnitude \bar{q} , the average scattered intensity is given by

$$I(\bar{q}) = \frac{n_p \Delta \rho^2}{V_{sc}} \int_0^\infty \int_0^\infty Res(\bar{q}, q, \sigma) RDF(R, \sigma_p) V(R)^2 P(q, R) dR dq \quad (6.2)$$

In this expression $\Delta\rho$ is the scattering contrast between the continuous phase and the particles, $Res(\bar{q}, q, \sigma)$ is the instrument resolution function, $RDF(R, \sigma_p)$ the particle radius distribution function and $V(R)$ the scattering weight of the particle fraction with radius R . The resolution function can be described by^[26,27]

$$Res(\bar{q}, q, \sigma) = \frac{q}{\sigma^2} \exp\left(-\frac{\bar{q}^2 + q^2}{2\sigma^2}\right) \cdot I_0\left(\frac{\bar{q}q}{\sigma^2}\right) \quad (6.3)$$

Here σ is the smearing parameter for \bar{q} , which accounts for the instrument collimation configuration, beam wavelength spread, apertures and detector pixel size. $I_0(x)$ is the modified Bessel function of the first kind. Pedersen^[27] notes that 10 point discretization is sufficient for the calculation resolution function, the same discretization was used here.

Collapsed PNIPAM particles can be approximated as homogeneous spheres,^[18] adequately described by the hard sphere form factor

$$P(q, R) = \left(\frac{3 [\sin(qR) - qR \cos(qR)]}{(qR)^3} \right)^2 \quad (6.4)$$

with the scattering weight of a homogenous sphere given by

$$V(R) = \frac{4}{3} \pi R^3 \quad (6.5)$$

In lack of further knowledge on the particle size distribution, it is reasonable to assume the particle weight (volume) to be distributed according to the normal distribution. From the properties of random variables it follows that

$$RDF(R, \sigma_p) = 4\pi^2 g\left(\frac{4}{3}\pi R^3, \sigma_p\right) \quad (6.6)$$

where $g(V, \sigma_p)$ is Gaussian distribution in respect to particle volume and σ_p is the polydispersity index, i.e. standard deviation of the distribution divided by its mean. It is noteworthy that typically the particle size distribution is assumed to be Gaussian in radius,^[18] which leads to smaller values for the polydispersity index than reported in this work. Discretization of 50 points was used in the numerical calculation of the integral over the distribution.

The number of particles formed during the early reaction nucleation period determines final particle volume of microgels.^[23,24] A model independent method to approximate the particle number density is the Porod invariant,^[28] which is related to the volume fractions of the polymer and heavy water phases in the scattering volume

$$Q = \int_0^\infty I(q) q^2 dq = 2\pi^2 \Phi(1 - \Phi)(\Delta\rho)^2 \quad (6.7)$$

where Φ and $(1 - \Phi)$ are the volume fractions of polymer repeating units and heavy water in the scattering volume. The unsmeared model expression $I(q)$ was used to calculate the integral. During the reaction the collapsed polymer is located in particles with average volume \bar{V}_p and therefore the volume fraction of polymer in the scattering volume V_{sc} is given by

$$\Phi = \frac{n_p \Phi_p \bar{V}_p}{V_{sc}} \quad (6.8)$$

where Φ_p is the polymer volume fraction inside the particles, here taken as 0.42 for collapsed PNIPAM microgels.^[18] The time evolution of the number of particles in the scattering volume can be then approximated by rearranging Eq. 6.8

$$n_p(t) = \frac{\Phi(t) V_{sc}}{\Phi_p \bar{V}_p(t)} \quad (6.9)$$

Above, scattering volume V_{sc} ($4.8 \times 10^{-5} \text{ dm}^3$) is an instrumental parameter determined by the cuvette path length and beam dimensions. Average volume of particles $\bar{V}_p(t)$ is obtained by fitting the model expression Eq. 6.2 to the experimental scattering patterns; the volume fraction of polymer is solved from the Porod integral, Eq. 6.7.

6.4 Experimental

All *in situ* measurements were performed at small-angle neutron scattering diffractometer KWS-2^[29] using detector distance of 20 m. The nominal wavelength provided by the mechanical velocity selector was 7 Å with 20 % wavelength spread. The scattered neutrons were detected with a planar ^3He tube array detector; the detector image was azimuthally integrated to obtain the angular scattering pattern $I(q)$. Before averaging, the detector images were corrected for empty cell and solvent scattering, as well as for electronic and background noise.

PNIPAM was recrystallized from hexane; cross-linker N,N'-methylenebisacrylamide (BIS), initiator ammoniumpersulfate (APS) and accelerator N,N,N',N'-tetraethylethylenediamine (TEMED) were used as received. Monomer and initiator solutions of appropriate concentrations were prepared separately to heavy water and deoxygenized by purging with argon. When accelerator TEMED was used, it was mixed in with the monomers.

Precipitation polymerization was carried out in a BioLogic SFM-300 stopped-flow device, which was positioned in the neutron beam. SFM-300 was connected to a Julabo refrigerated circulator, tempered at 65 °C. Prior to loading the monomer

and initiator into separate sample chambers of the SFM-300 instrument, the chambers, channels, mixer and cuvette were flushed with deoxygenized heavy water to remove oxygen from the device.

After tempering the monomer and initiator solutions in the chambers at least 15 min, the reaction was initiated by rapidly mixing the monomer and initiator in 1:1 ratio. The reaction was monitored for minimum 20 min, using 5 sec integration time.

MATLAB program FitIt!, designed for evaluation of static scattering data, was scripted to fit approximately 15 000 scattering patterns with the model described in the previous section.

6.5 Results and Discussion

6.5.1 Validity of the model expression

Typical data from an *in situ* stopped-flow polymerization at various reaction times is shown in Figure 6.1. After the initiation of the polymerization in the mixer chamber the reaction mixture is rapidly directed to the observation cuvette, where it remains stationary for the duration of the reaction. The early reaction time scattering pattern is typically flat, except for a sharp upturn at the low q region. Strong forward scattering indicates the presence of large structures. The origin of this phenomenon is likely due to small argon bubbles from the mixing, as any polymer structures present at the early reaction stage are expected to be small. With increasing reaction time the scattering from the growing polymer particles begins to dominate the scattered intensity. This is seen from the emergence of a form factor minimum, which shifts to smaller q values with increasing particle size.

Solid lines in Figure 6.1 denote the model expression, Eq. 6.2, fitted to the data points. Generally the model captures well the features of the data, confirming that the collapsed PNIPAM particles can be treated as homogeneous spheres. Homogeneous structure is to be expected as the thermal blobs of a polymer in a poor solvent, such as PNIPAM at temperatures over the volume phase transition temperature (VPTT) in D₂O, pack densely together to minimize the surface area with the solvent.^[30] The dashed line in the form factor measured 1200 s after reaction start on top of the model fit shows the unsmeared scattering pattern without instrumental effects.

The calculation of the Porod invariant imposes certain requirements for the system under investigation.^[28] The experimental intensity should not exhibit a strong upturn as $q \rightarrow 0$, which is typical for aggregated systems. In addition the scattering intensity has to decay faster than q^{-3} .

Smooth behavior and good model fit in the low q regime of the experimental

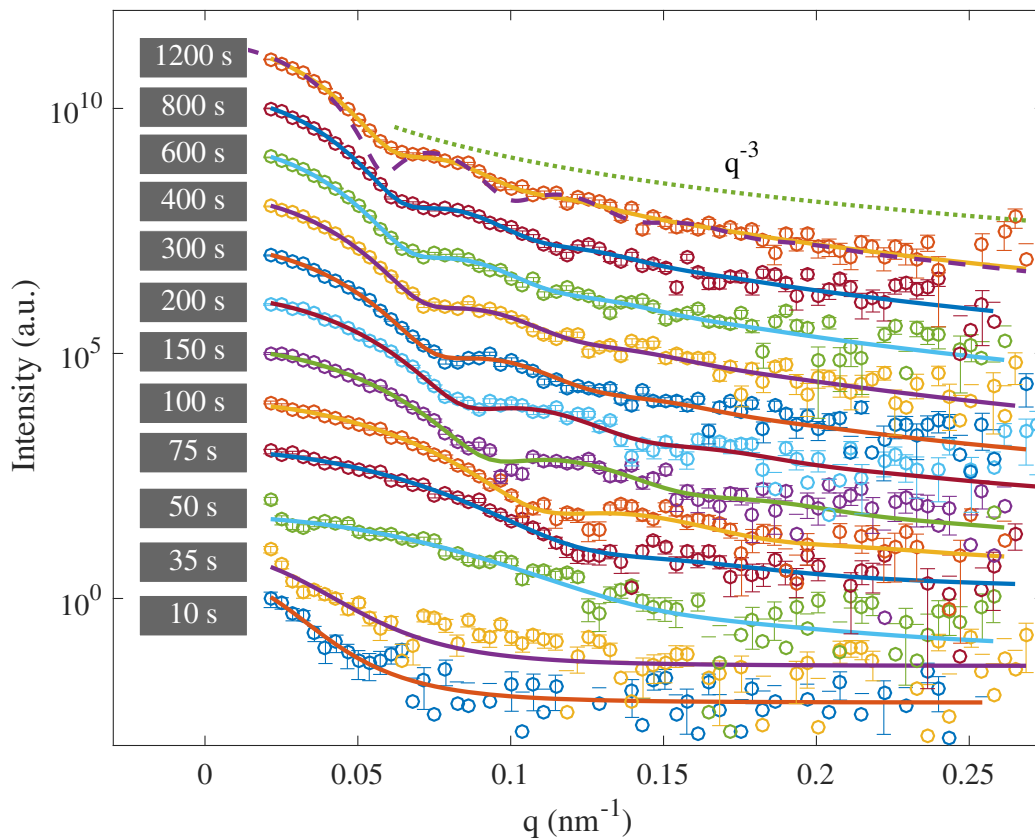


Figure 6.1: Form factors at various reaction times. Solid lines denote the model expression. Dashed line shows the model expression without instrumental smearing. Dotted line demonstrates that the scattered intensity decays faster than q^{-3} . Data sets are arbitrarily scaled for clear presentation. NIPAM concentration was $2.00 \times 10^{-2} \text{ mol dm}^{-3}$, APS and TEMED concentrations were, $1.56 \times 10^{-3} \text{ mol dm}^{-3}$ and $1.56 \times 10^{-3} \text{ mol dm}^{-3}$, respectively.

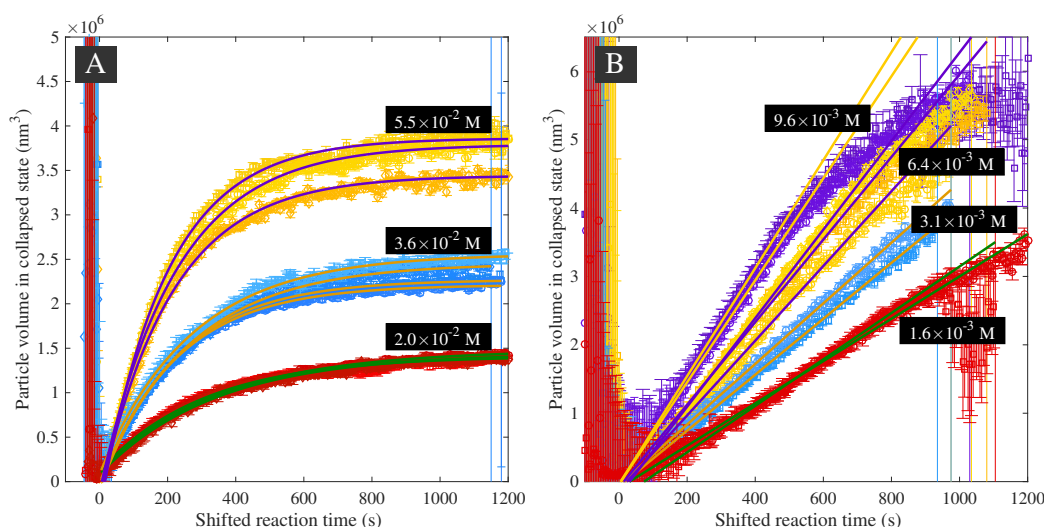


Figure 6.2: Average particle volume with reaction time. Repetitions under the same reaction conditions are denoted by the color scheme. Traces have been shifted to 0 for clear presentation. **A:** For various NIPAM concentrations. APS and TEMED were used as redox initiation system. Their concentrations were $1.56 \times 10^{-3} \text{ mol dm}^{-3}$ and $1.56 \times 10^{-3} \text{ mol dm}^{-3}$, respectively. Solid lines are fits to Eq. 6.11. **B:** For various APS concentrations. APS was solely used to initiate the reaction. NIPAM concentration was $3.65 \times 10^{-2} \text{ mol dm}^{-3}$. Solid lines are linear fits. The traces were shifted to zero reaction time for clearer presentation.

data indicates that no aggregation of particles takes place during the polymerization. Aggregation would be observed as intensified forward scattering and/or a kink in the low q regime due to correlation of particle positions in a small aggregate, in analogy to the structure factor. In fact the data shows no sign of the presence of structure factor in the experimentally accessible q range, which indicates dilute dispersion and/or weak interactions between the particles. The model used here would not be able to describe these features if they were present, leading to a poor fit. A dotted line at the top of Figure 6.1 shows that the experimental data decays faster than q^{-3} , fulfilling the other requirement.

6.5.2 Average particle growth follows pseudo-first order kinetics

Monomer and initiator concentration have marked effects on the final particle volume of PNIPAM microgels, which exhibits power law behavior in respect to both of these reactants.^[23,24] *In situ* 3D dynamic light scattering experiments have shown the average growth rate of the particles to increase with both the

monomer and initiator concentration.^[25] Figure 6.2A confirms that the average volume growth rate and final particle volume is strongly influenced by the initial monomer concentration. The same color of the traces denotes repetition of the measurement under the same reaction conditions. Slightly variable induction periods were observed for the repetitions presumably due to trace amounts of oxygen in the instrument; the traces in Figure 6.2 are shifted to zero reaction time for clear presentation. The experiment is the most reproducible at the lowest monomer concentration of $2.0 \times 10^{-2} \text{ mol dm}^{-3}$, the higher monomer concentration runs show more variation in respect to the final particle volume. The initial high volumes with large uncertainty possibly arise from mixing induced microbubbles as discussed in the context of Figure 6.1.

PNIPAM particles typically have a narrow size distribution,^[18,19] which implies a short particle nucleation phase at the beginning of reaction and subsequent particle growth. If no particle aggregation takes place during the polymerization, the time evolution of the average particle volume during the reaction can be assumed to follow

$$\bar{V}_p(t) = \frac{V_M}{n_p(t)} \int_0^t R_p(t) dt \quad (6.10)$$

where V_M is the volume of collapsed polymer, including water,^[31] polymerized from one mole of NIPAM, n_p the number of particles in the batch and R_p the rate of monomer consumption. The experimentally observed particle growth in Figure 6.2A could be well described with an equation of the form

$$\bar{V}_p(t) = \frac{V_M}{n_p} \left[1 - \exp\left(-\frac{t}{\tau}\right) \right] \quad (6.11)$$

where τ is the time constant of the reaction. Single exponential behavior implies that the particle growth rate depends only on the monomer concentration, indicating pseudo-first order kinetics for the polymerization. Furthermore, the observed behavior requires the particle concentration to remain approximately constant throughout the growth phase.

Pseudo-first order behavior can take place if the initiator concentration does not change considerably during the reaction. The polymerization was initiated with APS-TEMED system to minimize the effects of oxygen in the stopped-flow instrument. Peroxide-amine redox initiation is typically 1 to 3 orders of magnitude faster than the corresponding peroxide without the accelerator^[32] and rapidly consumes any trace amounts of oxygen in the stopped-flow cuvette. Assuming the rate constant for the redox reaction is in the order of $1.2 \times 10^{-2} \text{ dm}^3 \text{ mol}^{-1} \text{ s}^{-1}$ ^[32] the half-lives of the redox components are approximately 14 h given the concentration of $1.56 \times 10^{-3} \text{ mol dm}^{-3}$ used for both APS and TEMED. For our microgel

syntheses, the volume traces in Figure 6.2A approach plateau after 20 min reaction time, showing that the time necessary to approach full conversion is short in comparison to the initiator half-life. This result supports the notion that the pseudo-first order kinetics arise from negligible initiator consumption.

Particle growth traces for pure APS initiation without the accelerator TEMED is shown in Figure 6.2B. Long and variable induction periods were observed with thermally decomposing initiator. The instrument was always flushed with argon purged D₂O to remove the oxygen from the system prior to loading the deoxygenized reactants to the stopped-flow device. This is however an error prone procedure and trace amounts of oxygen in the instrument are the likely explanation for the initial inhibition of the reaction.

The reaction rate was significantly reduced without the accelerator TEMED, which is seen from the fact the particle volume trace does not level off in a comparable polymerization time frame as in Figure 6.2A. The initial particle growth regime appears linear for all except the highest APS concentration of $9.6 \times 10^{-3} \text{ mol dm}^{-3}$. The same behavior has been earlier reported for *in situ* 3D DLS measurements.^[25] The traces in Figure 6.2B were fitted with a linear model. For the highest APS concentration the fit was limited to the linear section of the trace.

6.5.3 Evolution of particle number density with reaction time

Number of particles with reaction time was calculated from Eq. 6.9 for batches with variable NIPAM and APS concentration, shown in Figure 6.3 A and B, respectively. In all the cases the number of particles in the scattering volume approaches a plateau, confirming that the particle number density stays approximately constant throughout the reaction. The apparent particle number in scattering volume is also affected by possible sedimentation of particles and convection due to temperature gradients in the stopped-flow instrument. Given the scattering volume of $4.8 \times 10^{-5} \text{ dm}^3$, all the particle concentrations in this work settle in the range of 10^{15} dm^{-3} to 10^{16} dm^{-3} , which is compatible with values of 10^{15} dm^{-3} to 10^{17} dm^{-3} reported earlier by Wu et al.^[20]

For three different NIPAM concentrations in Figure 6.3 the final particle concentration varies in a non-linear way. When comparing across batches with variable initial NIPAM concentration, earlier work has indirectly shown that the number of particles n_p in the batch goes through a maximum and then decreases again when the initial NIPAM concentration is increased further.^[23,24] The observed behavior is consistent with these results, but a more comprehensive data set is necessary to validate this observation.

Peroxide initiators (used without accelerator) are known to induce cross-links to PNIPAM particles to the extent that the particles gelate even without additional crosslinker.^[21,22] Lately we have shown that the crosslinks concentrate on

the particle periphery, leading to an inverted crosslinking structure in comparison to conventional PNIPAM microgels.^[19] The particle volume in collapsed state has been shown to increase with potassium persulfate (KPS) concentration,^[22,25] which can be attributed to either decreasing particle concentration or increasing water affinity of the network due to increased number of hydrophilic initiator fragments.

Figure 6.3 B shows systematically decreasing number of particles in the scattering volume with increasing APS concentration. In the case the polymer volume fraction Φ_p in the particles decreased due to increased water affinity, the apparent number of particles should increase according to Equation 6.9. As the opposite behavior is observed in Figure 6.3 B, we conclude that particle number density does indeed decrease with increasing peroxide initiator concentration. Previous work has shown that the increased ionic strength due to peroxide initiator does not significantly promote the coagulation of the nuclei,^[23] and therefore the likely explanation for the decreased particle density is the increased probability of irreversible nuclei aggregation due to peroxide induced crosslinking reactions.

6.5.4 Total volume growth rate is proportional to polymerization rate

Rearrangement of Eq. 6.10 shows that the total volume growth ($n_p \cdot d\bar{V}_p/dt$) rate is proportional to the polymerization rate up to a constant factor V_M^{-1} as

$$R_p(t) \propto n_p(t) \frac{d\bar{V}_p}{dt} \quad (6.12)$$

Figure 6.4 shows total volume growth rate with NIPAM and APS concentration, calculated from Eq. 6.9 and the derivative of Eq. 6.11 at zero reaction time. The total volume growth rate increases when both the monomer and initiator concentration in the batch is increased, being clearly more sensitive to NIPAM concentration in comparison to APS concentration. Earlier work has shown the polymerization rate to be close to power law behavior of radical solution polymerization with $R_p \propto [\text{Monomer}][\text{Initiator}]^{1/2}$ shortly after initiation.^[25,24] This is not surprising given the abundant solubility of NIPAM in water, which implies that significant conversion has to take place in the water phase during the early stages of the reaction.

The power law exponent in respect to NIPAM concentration, determined here as 1.54 ± 0.07 is higher than expected based on the earlier results of 0.94 ± 0.08 ^[25] and 1.05 ± 0.08 .^[24] Given the limited amount of experimental data the value is however in reasonable agreement with previous work. As expected for radical solution polymerization, the power law exponent of 0.42 ± 0.03 in respect to APS

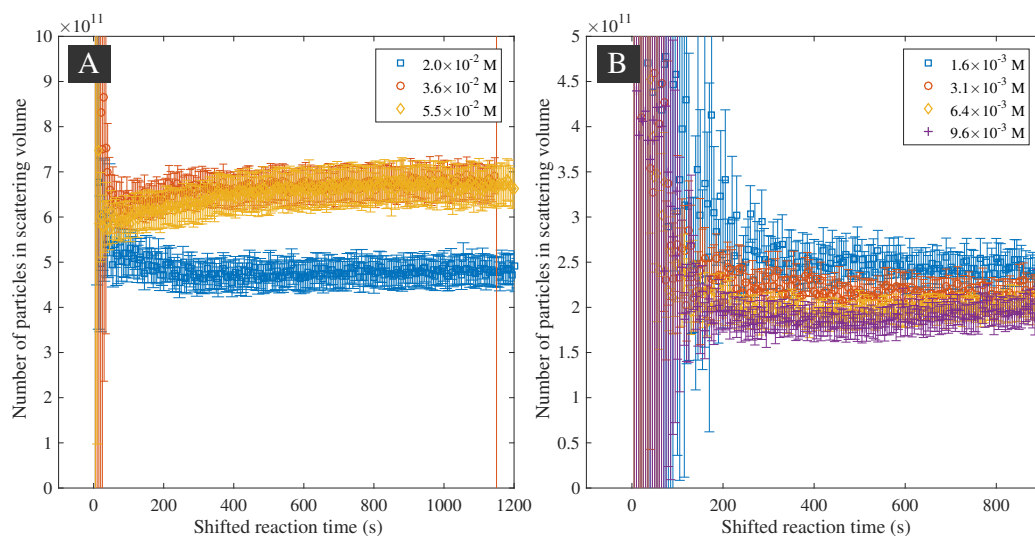


Figure 6.3: Number of particles with reaction time averaged over repetitions. **A:** For various NIPAM concentrations. APS and TEMED concentrations were $1.56 \times 10^{-3} \text{ mol dm}^{-3}$ and $1.56 \times 10^{-3} \text{ mol dm}^{-3}$, respectively. **B:** For various APS concentrations. No TEMED was used in the synthesis. NIPAM concentration was $3.65 \times 10^{-2} \text{ mol dm}^{-3}$.

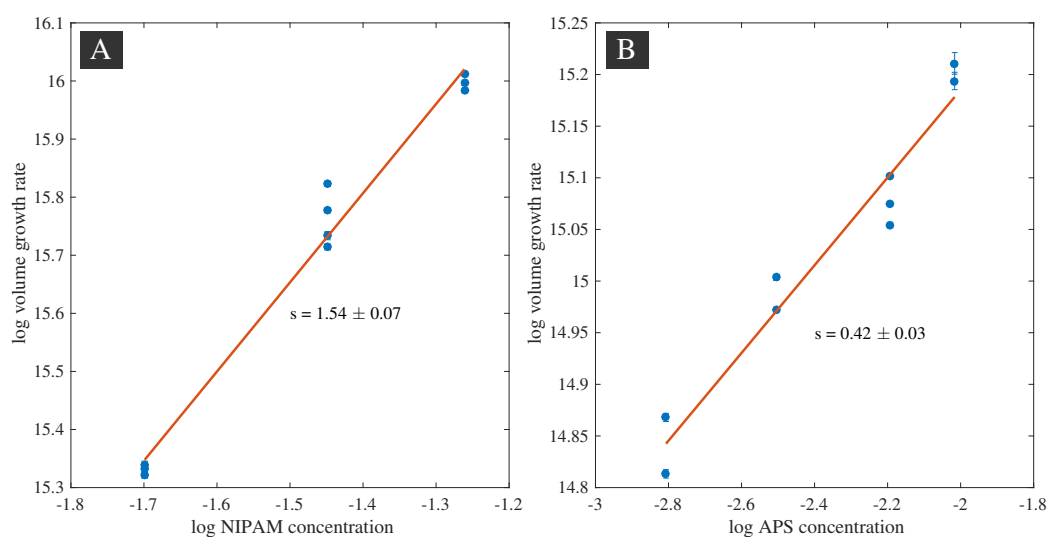


Figure 6.4: Total volume growth rate extrapolated to zero time. **A:** Plotted against NIPAM concentration in log-log presentation. APS and TEMED were used as redox initiation system. Their concentrations were $1.56 \times 10^{-3} \text{ mol dm}^{-3}$ and $1.56 \times 10^{-3} \text{ mol dm}^{-3}$, respectively. **B:** Plotted against APS concentration in log-log presentation. No TEMED was used in the synthesis. NIPAM concentration was $3.65 \times 10^{-2} \text{ mol dm}^{-3}$. Solid lines denote linear fit to the data points.

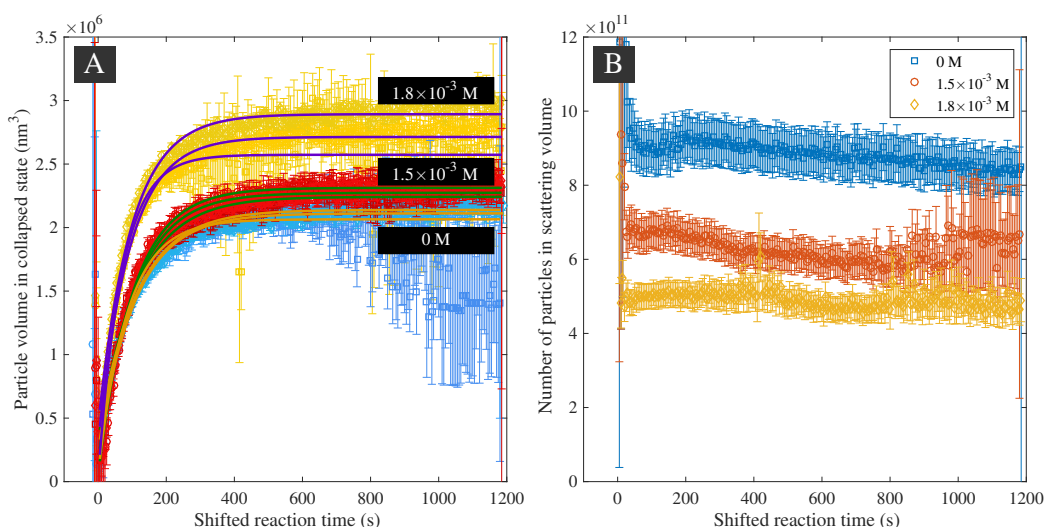


Figure 6.5: A: Average particle volume with reaction time with increasing bisacrylamide concentration. Repetitions with the same reaction conditions are denoted by the color scheme. Traces have been shifted to 0 for clear presentation. In each batch NIPAM concentration was $3.65 \times 10^{-2} \text{ mol dm}^{-3}$, APS concentration $1.56 \times 10^{-3} \text{ mol dm}^{-3}$ and TEMED concentration $3.12 \times 10^{-3} \text{ mol dm}^{-3}$. BIS concentrations are given in the graph. **B:** Number of particles with increasing bisacrylamide concentration.

concentration is close to half an order, in the vicinity of earlier results of 0.46 ± 0.05 ^[25] and 0.56 ± 0.03 .^[24]

6.5.5 Effect of crosslinker bisacrylamide on particle growth rate and number density

N,N'-methylenebisacrylamide (BIS) is a typical crosslinker in microgel synthesis. Copolymerization with BIS increases the particle size of microgels in collapsed state, which has been documented on multiple occasions.^[23,19,20,22] Figure 6.5 A shows that even a small addition of BIS to monomer mixture has a marked effect on the average particle growth, leading to larger final particle volume.

BIS is not expected to significantly alter the water affinity of the network and therefore the likely explanation for the increased particle size is a decrease in the particle number density. This is confirmed in Figure 6.5 B, which shows the decrease of particle number in the scattering volume with increasing BIS concentration.

As the number of particles in the scattering volume stays approximately constant throughout the reaction, the differences in the number of particles arise al-

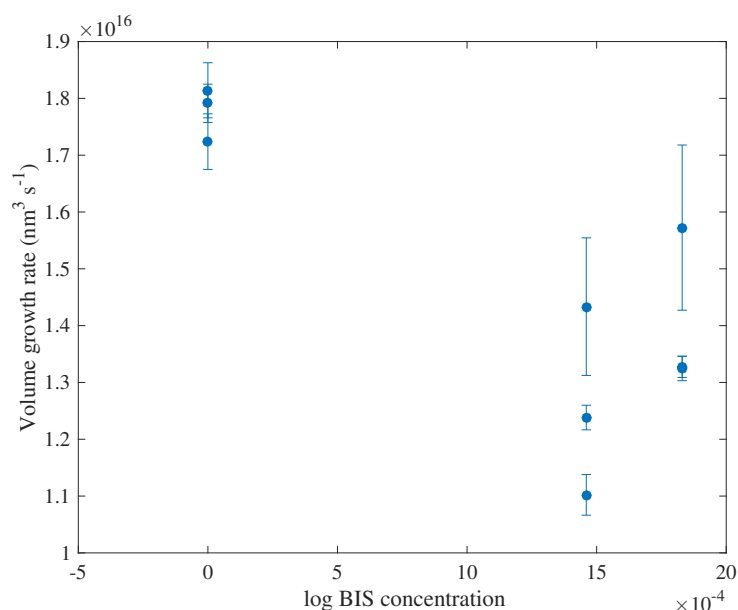


Figure 6.6: Total volume growth rate extrapolated to zero reaction time with increasing BIS concentration.

ready at the onset of the reaction during the nucleation phase. Incorporation of bifunctional bisacrylamide units to the nuclei increase the probability of their irreversible aggregation with each other, which leads to decrease in the particle number density.

Figure 6.6, shows the effect of BIS on the total volume growth rate of the particles, calculated from Eq. 6.12. Even though BIS clearly decreases the number of particles in the batch leading to larger final particle volume, the effect on the reaction rate is clearly less pronounced. A more comprehensive dataset is however necessary for an unambiguous conclusion on this matter.

6.6 Conclusion

In this work we monitored particle growth in precipitation polymerization of N-isopropylacrylamide *in situ* by small-angle neutron scattering. In earlier work features of the reaction have been deduced from the properties of the resulting polymer particles; here we presented data from direct measurements throughout the evolution of growing microgels.

The average particle volume growth was found to adhere to pseudo-first order kinetics, indicating that the polymerization rate is dominated by the amount of unreacted monomer at any given reaction state. Scattering data showed that

monomer, initiator and cross-linker concentration all affect the particle number density in the batch, which in turn determines the final particle volume. Of special note is the effect of cross-linking reactions: Both persulfate initiator induced crosslinking and bifunctional monomer decrease the concentration of particles in the batch, presumably because of increased probability of irreversible aggregation of particle nuclei during the nucleation phase.

Spherical particles could be detected rapidly after the onset of the reaction after which their concentration remained approximately constant. The initial polymerization rate deduced from the total volume growth rate in the reaction was sensitive to both initiator and monomer concentration, in accordance to radical solution mechanism. This and other results presented here support and confirm indirect results from earlier work and solidify our understanding of precipitation polymerization of thermosensitive polymers.

Bibliography

- [1] H. G. Schild, *Progress in Polymer Science*, 1992, **17**, 163–249.
- [2] A. Halperin, M. Kröger and F. M. Winnik, *Angew. Chem.*, 2015, **127**, 15558–15586.
- [3] W. McPhee, K. C. Tam and R. Pelton, *Journal of Colloid and Interface Science*, 1993, **156**, 24–30.
- [4] Z. Meng, M. H. Smith and L. A. Lyon, *Colloid and Polymer Science*, 2009, **287**, 277–285.
- [5] R. Pelton, *Advances in Colloid and Interface Science*, 2000, **85**, 1–33.
- [6] A. Pich and W. Richtering, *Advances in Polymer Science*, 2010, **234**, 1–37.
- [7] W. Richtering, *Langmuir*, 2012, **28**, 17218–17229.
- [8] S. Wiese, A. C. Spiess and W. Richtering, *Angew. Chem. Int. Ed.*, 2012, **52**, 576–579.
- [9] V. Schmitt and V. Ravaine, *Current Opinion in Colloid and Interface Science*, 2013, **18**, 532–541.
- [10] O. S. Deshmukh, D. van den Ende, M. C. Stuart, F. Mugele and M. H. G. Duits, *Advances in Colloid and Interface Science*, 2015, **222**, 215–227.
- [11] T. R. Hoare and D. S. Kohane, *Polymer*, 2008, **49**, 1993–2007.
- [12] T. J. Merkel, S. W. Jones, K. P. Herlihy, F. R. Kersey, A. R. Shields, M. Napier, J. C. Luft, H. L. Wu, W. C. Zamboni, A. Z. Wang, J. E. Bear and J. M. DeSimone, *Proceedings of the National Academy of Sciences of the United States of America*, 2011, **108**, 586–591.
- [13] N. M. B. Smeets and T. Hoare, *Journal of Polymer Science Part A Polymer Chemistry*, 2013, **51**, 3027–3043.
- [14] S. Schmidt, M. Zeiser, T. Hellweg, C. Duschl, A. Fery and H. Möhwald, *Adv. Funct. Mater.*, 2010, **20**, 3235–3243.
- [15] Y. Xia, X. He, M. Cao, C. Chen, H. Xu, F. Pan and J. R. Lu, *Biomacromolecules*, 2013, **14**, 3615–3625.

- [16] L. V. Sigolaeva, S. Y. Gladyr, A. P. H. Gelissen, O. Mergel, D. V. Pergushov, I. N. Kurochkin, F. A. Plamper and W. Richtering, *Biomacromolecules*, 2014, **15**, 3735–3745.
- [17] L. V. Sigolaeva, O. Mergel, E. G. Evtushenko, S. Y. Gladyr, A. P. H. Gelissen, D. V. Pergushov, I. N. Kurochkin, F. A. Plamper and W. Richtering, *Langmuir*, 2015, **31**, 13029–13039.
- [18] M. Stieger, J. S. Pedersen, W. Richtering and P. Lindner, *Journal of Chemical Physics*, 2004, **120**, 6197–6206.
- [19] O. L. J. Virtanen, A. Mourran, P. T. Pinard and W. Richtering, *Soft Matter*, 2016, **12**, 3919–3928.
- [20] X. Wu, R. H. Pelton, A. E. Hamielec, D. R. Woods and W. McPhee, *Colloid and Polymer Science*, 1994, **272**, 467–477.
- [21] J. Gao and B. J. Frisken, *Langmuir*, 2003, **19**, 5212–5216.
- [22] J. Gao and B. J. Frisken, *Langmuir*, 2003, **19**, 5217–5222.
- [23] O. L. J. Virtanen, H. M. Ala-Mutka and W. Richtering, *Macromol. Chem. Phys.*, 2015, **216**, 1431–1440.
- [24] O. L. J. Virtanen, M. Brugnoli, M. Kather, A. Pich and W. Richtering, *Polymer Chemistry*, 2016.
- [25] O. L. J. Virtanen and W. Richtering, *Colloid and Polymer Science*, 2014, **292**, 1743–1756.
- [26] T. Freltoft, J. K. Kjems and S. K. Sinha, *Physical Review B*, 1986, **33**, 269–275.
- [27] J. S. Pedersen and C. Riekel, *J Appl Crystallogr*, 1991, **24**, 893–909.
- [28] O. Spalla, *Neutrons, X-rays and Light: Scattering Methods Applied to Soft Condensed Matter*, Amsterdam: North Holland Delta Series, 2002, pp. 49–71.
- [29] A. Radulescu, N. K. Szekely and M.-S. Appavou, *JLSRF*, 2015, **1**, A29–5.
- [30] M. Rubinstein and R. H. Colby, *Polymer Physics*, Oxford University Press, 2003.
- [31] R. H. Pelton, *Journal of Colloid and Interface Science*, 2010, **348**, 673–674.
- [32] G. Odian, *Principles of Polymerization*, Wiley Interscience, 4th edn, 2004.

7. Structure of ultra-low cross-linked microgels

7.1 Abstract

Cross-linking density and distribution are decisive for mechanical and other properties of stimuli-sensitive poly(N-isopropylacrylamide) microgels. Here we investigate the structure of ultra low cross-linked microgels by static light scattering and scanning force microscopy, and show that they have inverted cross-linking structure with respect to conventional microgels, contrary to what has been assumed previously. The conventional microgels have the largest polymer volume fraction in the core from where the particle density decays radially outwards, whereas ultra low cross-linked particles have the highest polymer volume fraction close to the surface. On solid substrate these particles form buckled shapes at high surface coverage, as shown by scanning force micrographs. The special structure of ultra low cross-linked microgels is attributed to cross-linking of the particle surface, which is exposed to hydrogen abstraction by radicals generated from persulfate initiators during and after polymerization. The particle core, which is less accessible to the diffusion of radicals, has consequently lower polymer volume fraction in swollen state. By systematic variation of the cross-linker concentration it is shown that the cross-linking contribution from peroxide under typical synthesis conditions is weaker than that from the use of 1 mol – % N,N'-methylenebisacrylamide. Soft deformable hydrogel particles are of interest because they emulate biological tissues, and understanding the underlying synthesis principle enables tailoring the microgel structure for biomimetic applications. Deformability of microgels is usually controlled by the amount of added cross-linker; here we however highlight an alternative approach through structural softness.

7.2 Introduction

Stimuli-sensitive poly(N-isopropylacrylamide) (PNIPAM) microgels^[1,2] and derivatives, spherical cross-linked gel particles with radii from tens of nanometers to few micron, have found various application areas including e.g. temperature sensitive microgel coatings^[3,4,5,6] that enable easy cell harvesting from cell culture substrates^[7,8], microlenses^[9], stabilizers for smart emulsions^[10,11,12,13,14,15] and potential biomedical uses.^[16]

A recent development in the field are hollow microgel particles^[17,18,19], which show significantly higher deformability and spreading at interfaces^[20] in comparison to conventional PNIPAM microgels. Ultra low cross-linked (ULC) microgel particles^[21,22] exhibit similar properties; therefore both of these particle types might prove useful in biomimetic^[23] and loading and release^[24,25,26] applications.

Excessive deformability of hollow microgels arises from their unconventional structure^[18]. Therefore the polymer volume fraction (cross-linking) distribution inside the PNIPAM particles determine their mechanical properties and is an important factor for their permeability to guest molecules, such as enzymes.^[27,28] In the case of ultra-low cross-linked microgels, it has been suggested that these particles possess similar structure to conventional microgels^[29], only with significantly lower cross-linking density.^[22] In the previous work ULC microgels were characterized on a solid substrate, where extensive deformation of the particles has been reported.^[3,4,5,30,31,32,33,34] In this contribution we investigate dispersion of particles in swollen state, which leads to a different conclusion: Ultra-low cross-linked microgels have inverted density profile in contrast to conventional fuzzy microgels, i.e., the highest polymer volume fraction is located close to the surface of the particle from where the density decays towards the core.

This unexpected structure can be attributed to hydrogen abstraction and subsequent cross-linking at the particle surface by persulfate initiator radicals^[35,36] during the late stages of the polymerization. To test this hypothesis, we first incubate non-cross-linked PNIPAM particles in potassium persulfate (KPS) solutions and show that the hydrogen abstraction effect is strong enough to create stable gel particles with an inverted structure. In contrast the non-cross-linked particles dissolve to the continuous phase upon cooling below PNIPAM volume phase transition temperature (VPTT). We then compare batches initiated with KPS and a redox initiation system, which doesn't cross-link the particles, and show that under typical reaction conditions the cross-linking extent by KPS is comparable to less than 1 mol – % N,N'-methylenebisacrylamide (BIS) in the batch. Conditions leading to different microgel architectures are schematically depicted in Figure 7.1.

An accurate characterization of the particle structure enables one to establish

detailed structure - properties relationships and ultimately control the synthesis of PNIPAM microgels for the application at hand. A suitable method for structure characterization of microgels of this particle size range in non-disturbed state in dispersion is static light scattering. Typically a model expression for the scattered intensity is required to obtain quantitative structure data of the scatterers, but here we used a more general direct inversion method, which yields the radial density profile for spherical particles. This method is briefly introduced in the next section and is useful for classifying particles whose structure is not known *a priori*. The sections discussing the extent of persulfate cross-linking follow, and are of interest for practitioners involved in synthesis and application of microgels. The light scattering experiments are supplemented by analyzing the topography of the dried microgels on a solid support.

7.3 Model expression for scattered light intensity

Light scattering from particles that are small in comparison to the wavelength of the incident laser radiation or have small refractive index difference to the surrounding solvent can be described by Rayleigh-Debye-Gans (RDG) theory (Chapter 8 by Glatter in^[37]). Large microgel particles described in this work do not fulfill the first condition, but due to being extensively swollen with solvent the overall refractive index of these particles is close to the refractive index of the solvent. Therefore it is unnecessary to account for Mie scattering effects that are observed for large particles with high refractive index mismatch with respect to the matrix. For further discussion regarding the possible Mie effects, see Supporting Information.

In RDG regime the average scattered light intensity from a dispersion of spherical particles with number density ρ_p and particle radius distribution function $D(R)$ at scattering vector magnitude q is given by^[38,29]

$$I(q) = \rho_p \Delta\rho^2 \int_0^\infty D(R) V(R)^2 P(q, R) dR \quad (7.1)$$

Here $V(R)$ and $P(q, R)$ denote the scattering mass and the form factor of a particle with radius R , respectively. $\Delta\rho$ is the scattering contrast, which, in our case, is proportional to the difference between the refractive indices of the solvent swollen particles and the continuous phase. The form factor $P(q, R)$, square of the scattering amplitude F , is given by

$$P(q, R) = F^2 = \left[\frac{b(q, R)}{b(0, R)} \right]^2 \quad (7.2)$$

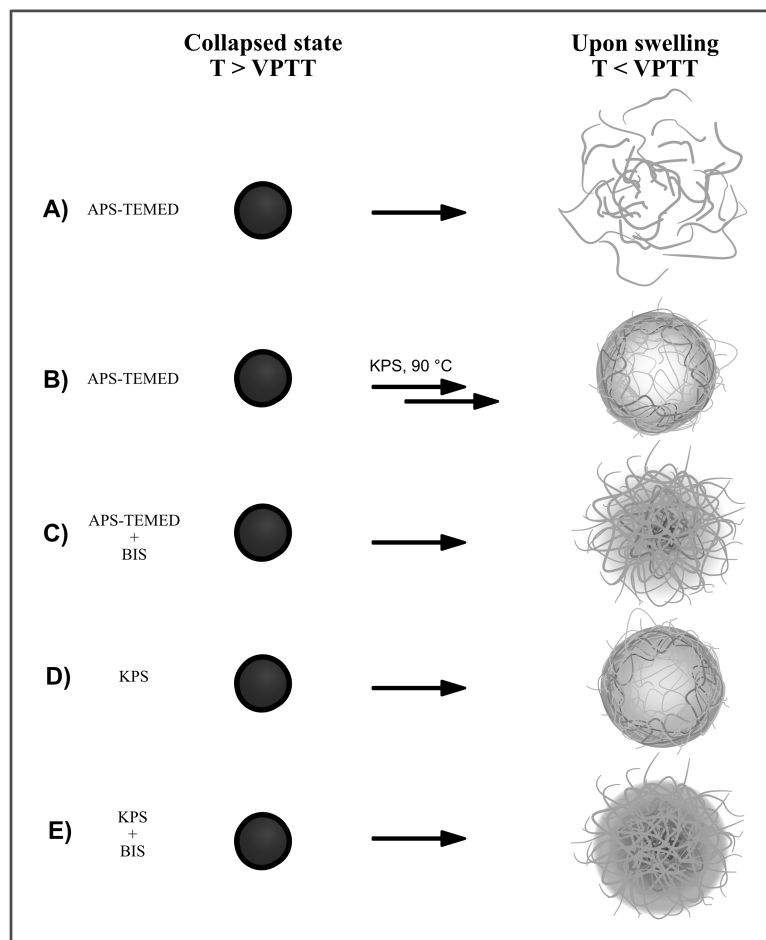


Figure 7.1: The effect of the initiator system and presence of cross-linker on the microgel architecture. Regardless of the initiation method and cross-linker, PNIPAM polymer particles are always homogeneous spheres in the collapsed state at the end of the polymerization. Upon cooling and swelling different structures are realized due to different cross-linking mechanisms: A) APS-TEMED initiated particles without cross-linker break to fragments, B) APS-TEMED initiated particles that are transferred and incubated in hot aqueous KPS solution after the polymerization exhibit an inverted microgel structure due to persulfate cross-linking of the surface, C) APS-TEMED initiated particles polymerized with the cross-linker BIS exhibit a fuzzy sphere structure, D) KPS initiated particles without cross-linker have an inverted structure analogous to B and E) KPS initiated particles with cross-linker BIS show fuzzy structure but with higher surface cross-linking density due to persulfate cross-linking.

where $b(q, R)$ is the scattering length of a particle with radius R . For particles with spherical symmetry, the scattering length depends on the radial excess contrast function $\alpha(r)$.

$$b(q, R) = 4\pi \int_0^R r^2 \alpha(r) \frac{\sin qr}{qr} dr \quad (7.3)$$

For particles made only of PNIPAM, $\alpha(r)$ is proportional to the density (volume fraction) of the polymeric material inside the particle at radial coordinate r .

Discretizing the unknown excess refractive index difference profile function $\alpha(r)$ in Eq. (7.3) to s steps, evaluating the integral and inserting in Eq. (7.2) results in the form factor for a particle with s concentric shells^[38]

$$P_s(q, R, \vec{\alpha}) = \frac{1}{V^2} \left[\alpha_1 V_1(R) F_1(q, R) + \sum_{i=2}^s (\alpha_i - \alpha_{i-1}) V_i(r_i) F_i(q, r_i) \right]^2 \quad (7.4)$$

with V_i , F_i and V given by

$$V_i(r_i) = \frac{4}{3} \pi r_i^3 \quad (7.5)$$

$$F_i(q, r_i) = \frac{3}{(qr_i)^3} [\sin(qr_i) - qr_i \cos(qr_i)] \quad (7.6)$$

$$V = \alpha_1 V_1(R) + \sum_{i=2}^s \alpha_i V_i(r_i) \quad (7.7)$$

Here i refers to the i th concentric shell, with 1st shell being the outermost. V is the total scattering mass of the particle, V_i and F_i are the the scattering mass and the scattering amplitude of a homogeneous sphere with radius r_i , respectively, and α_i are the components of the radial excess contrast vector for each shell.

The absolute refractive index profile and the number of particles ρ_p are not of primary interest for us in this work. Therefore $\Delta\rho(r)^2$ and n are absorbed to a scaling parameter A , so that Eq. (7.1) becomes

$$I_s(q, A, \vec{\alpha}) = A \frac{\int_0^\infty D(R) V(R)^2 P_s(q, R, \vec{\alpha}) dR}{\int_0^\infty D(R) V(R)^2 dR} \quad (7.8)$$

A small intensity fraction η of the incident beam is reflected back from the inside wall of the cuvette, which leads to a scattering process in the opposing direction to the incident beam. Accounting for this phenomenon leads to the model expression for the total scattered intensity

$$I^M(q, A, \eta, \vec{\alpha}) = I_s(q, A, \vec{\alpha}) + \eta I_s(q', A, \vec{\alpha}) \quad (7.9)$$

where q' is the scattering vector magnitude of the back reflected beam observed at q , given by

$$q' = \frac{4\pi n}{\lambda_0} \sin\left(\frac{\pi - \theta}{2}\right) \quad (7.10)$$

Here n is the refractive index of the dispersion, λ_0 the wavelength of the incident radiation in vacuum and θ the scattering angle where the detector is positioned. For the particle radius distribution function $D(R)$ we use Burr Type XII distribution

$$D(R, \vec{d}) = D(R, S, B, C) = \frac{BC}{S} \left(\frac{R}{S}\right)^{B-1} \left[1 + \left(\frac{R}{S}\right)^B\right]^{-C-1} \quad (7.11)$$

where the parameter vector \vec{d} contains parameters S , B and C relating to the scale of the distribution, its width and skewness, respectively. This flexible distribution enables both symmetric and tailed particle size distributions. In prior work^[29] Gaussian function has been used for radius distribution function. Further discussion on its applicability for the particles used in this work can be found in the Supporting Information.

The density profile and the particle size distribution parameters are evaluated by minimizing the regularized chi-squared in respect to total parameter vector \vec{p}

$$\chi_{reg}^2(\vec{q}, \vec{p}, \lambda) = \sum_{j=1}^M \sum_{i=1}^N \left(\frac{I_j^E(q_{ji}) - I_j^M(q_{ji}, A_j, \vec{\alpha}, \vec{d})}{\sigma_{ji}} \right)^2 + \lambda^2 \|L_1 \vec{\alpha}\|_1 \quad (7.12)$$

with

$$\vec{p} = [A_1 \cdots A_M \ \eta_1 \cdots \eta_M \ \vec{\alpha} \ \vec{d}] \quad (7.13)$$

The M datasets recorded at different wavelengths, each consisting of N measurement points $I^E(q_i)$ with experimental uncertainty σ_i , are fitted globally. That is, all the model parameters are shared between the datasets except the scaling and backreflection magnitude parameters.

Finding $\vec{\alpha}(r)$ from Eq. (7.12) is an ill-conditioned problem, i.e., the solution is very sensitive to the unavoidable noise in the data and even rounding errors resulting from finite precision arithmetic. In order to obtain physically meaningful approximations to $\vec{\alpha}(r)$, we use Tikhonov regularization with total variation

smoothing norm (the last term) in Eq. (7.12). Regularization parameter λ determines the smoothness of the solution, L_1 is the discrete first derivative operator, and $\|\cdot\|_1$ stands for the vector 1-norm. When justified, also second derivative smoothing norm $\lambda^2 \|L_2 \vec{\alpha}\|_2$ can be used. Here L_2 is the discrete second derivative operator and $\|\cdot\|_2$ refers to vector 2-norm. A good introduction to discrete inverse problems and regularization is provided by Hansen^[39].

A reasonable value for λ can be evaluated by the so-called L-curve criterion. In this approach, the quality of the fit is evaluated against the regularity of the solution, i.e., the solution is calculated with multiple λ values and the solution norm $\|\vec{\alpha}\|_2$ is plotted against the residual norm of the solution $\|I^M - I^E\|_2$. The curve forms typically an L-shape and a suitable λ value is found at the corner of the curve. This specific solution is usually a good compromise between fitting the data and the regularity of the solution, i.e., not fitting the noise.

The direct inversion method described here is not as general as the indirect transformation methods first described by Glatter^[40] and later e.g. Svergun^[41], which yield the pair distance distribution function, and require additional deconvolution step^[42,43] to obtain the radial profile for spherical particles. The advantage of our procedure however is that it works in our existing software framework, MATLAB[®] program FitIt! and is customizable to our specific requirements. For the program's ability to resolve different particle structures in the presence of noise and systematic distortions typical of static light scattering measurement, the interested reader is referred to performance evaluation by test cases in Supporting Information.

7.4 Experimental

7.4.1 Particle synthesis

Non-stirred precipitation polymerization^[44,45] was used to synthesize all the particles. This is a rapid highly reproducible small-scale synthesis method, which yields microgels with narrow size distribution. For KPS initiated batches master solutions of NIPAM, BIS and KPS were prepared. The master solutions were diluted and mixed in a way that 5 samples with varying BIS concentration (0, 0.4, 0.8, 2.0, 3.5 and 5.1 mol-%) but constant NIPAM (7.1×10^{-2} mol·dm⁻³) and KPS (3.1×10^{-3} mol·dm⁻³) concentrations were obtained. One milliliter of reaction mixtures were transported to eight test tubes with 10 mm diameter and sealed with rubber septa. All the eight tubes were purged with nitrogen for 30 minutes and then immersed into an oil bath tempered at 60 °C. The tubes were let to react overnight and transferred to an oven without letting them cool down below PNIPAM VPTT. APS-TEMED initiated batches were prepared similarly,

but APS solutions were held separate from the NIPAM-BIS-TEMED solutions. After immersion to the oil bath, 0.5 ml of deoxygenated APS solution was injected to 0.5 ml monomer-TEMED solution by 1 ml syringes in order to initiate the polymerization. The end concentrations of NIPAM, APS and TEMED were 1.5×10^{-1} , 3.1×10^{-3} and $4.7 \times 10^{-3} \text{ mol} \cdot \text{dm}^{-3}$, respectively. BIS concentrations for APS-TEMED batches were 0.4, 0.8, 1.9, 3.0, 4.1 and 5.1 mol – %. NIPAM concentration was doubled to compensate for the faster initiation rate with APS-TEMED system. BIS mole percentages were kept the same, except 0 mol – % BIS was replaced with 0.4 mol – % After taking samples for DLS analysis, the samples were ultracentrifuged 1 h at 30 000 rpm three times to remove any unreacted monomer and non-attached polymer.

7.4.2 Dynamic light scattering

All the particles were analyzed in collapsed state at 50 °C without letting them cool down below PNIPAM VPTT between synthesis and characterization. Particle dispersions were diluted by hot double distilled water to avoid multiple scattering. For DLS measurements, a 3D-DLS goniometer with one beam blocked $\lambda = 633 \text{ nm}$ was used. Typically 25 correlograms were acquired from 45 deg to 120 deg with the minimum acquisition time of 90 s. 2nd order cumulant expansion was fitted to the electric field correlation functions and the mean diffusion coefficient was solved by linear fit to

$$\Gamma_2 = Dq^2 \quad (7.14)$$

Here Γ_2 is the mean decay rate of the correlation function from the 2nd order cumulant fit, D the mean diffusion coefficient and q the magnitude of the scattering vector. Hydrodynamic volume was calculated from Stokes-Einstein relation and hydrodynamic volume by assuming the particles to be spheres with the radius of the hydrodynamic radius.

7.4.3 Static light scattering

Three sealed construction goniometers were used to measure form factors, all supplied by SLS-Systemtechnik GmbH. FICA and SOFICA type goniometers were equipped with diode lasers with wavelengths of 658 nm (15° to 146°, 1° increments) and 405 nm (25° to 145°, 1° increments), respectively. New SLS Type 3 goniometer, which has improved optics and electronics, accommodates three lasers that can be rotated to change the measurement wavelength. Wavelengths of 404 nm and 642 nm (15° to 155°, 1° increments) were used. All the samples were diluted from the purified dispersions and measured in 20 mm diameter cuvettes at 20 °C in water. Solvent trace was subtracted from all the measurements.

Minimum two datasets with different wavelengths were acquired from each batch. Typically different concentrations for blue and red lasers were used to avoid multiple scattering in the blue laser measurements. The scattering traces were imported to program FitIt! and inverted using 20 point discretization. The regularization parameter was determined from the L-curve, which was calculated for each batch.

7.4.4 Scanning force microscopy

The microgels were measured on a hydrophilic silicon wafer (cleaned by ultrasonication in isopropanol, dried, and treated with UV/O₂ for 12 min). Typically 200 μ l of purified microgel dispersion was deposited on the silicon wafer surface and the wafer was rotated at a speed of 3000 rpm for 4 minutes to spread the particles on the surface. Surface coverage was varied by the diluting the master dispersion. Scanning force microscopy (AFM) images were recorded on a Nanoscope V (Bruker) instrument in tapping mode. Cantilevers with resonance frequencies of 250 – 300 kHz and spring constants around 42 N/m were used. NanoScope Analysis v.1.50 software (Bruker) was used to analyze the AFM micrographs.

7.4.5 Scanning electron microscopy

Images were acquired in a scanning electron microscope, JEOL JXA8530F, to visually determine the size distribution of the macromolecules. The solutions were dried on GaAs wafer and observed using an accelerating voltage of 15 kV and an approximate beam current of 5 nA. The magnification was varied between 5000 to 7000. A image analysis routine written in Python using the *scipy*^[46] and *scikit-image*^[47] libraries was developed to identify every macromolecule while minimizing artifacts such as agglomerated molecules or surface debris. After a median filter to remove image noise, images were threshold using the Otsu algorithm. Molecules with an area less than 1 μ m², with a circularity

$$4 \times \text{area} / (\pi \times (\text{max.diameter})^2)$$

less than 0.75 and with a sphericity

$$4\pi \times \text{area} / (\text{perimeter})^2$$

less than 0.5 were discarded.

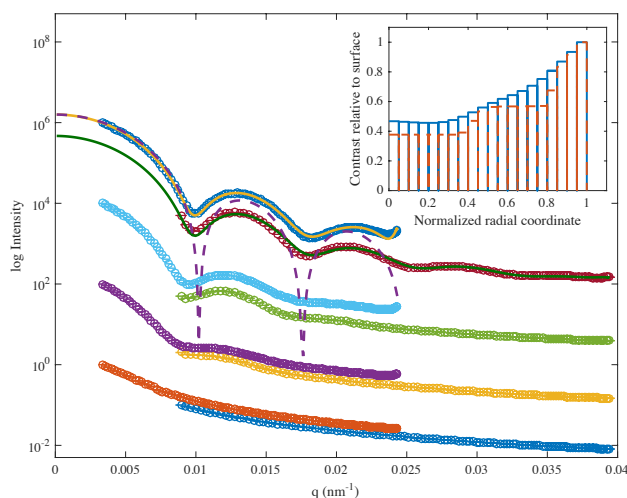


Figure 7.2: Form factors of initially non-cross-linked PNIPAM particles incubated in KPS solutions, in the swollen state at 20 °C in water. Intensities are scaled arbitrarily for clear presentation. KPS concentrations from top down: 3.12×10^{-3} , 1.57×10^{-3} , 7.78×10^{-4} and 0 mol·dm⁻³. In each sample the low q range was measured with wavelength of 658 nm and the high q range with 405 nm. The solid lines are the global fit on the particles formed at the highest KPS concentration calculated using 2nd derivative smoothing norm. The dashed line is reference form factor of a monodisperse hard sphere with the same mean square radius of gyration as the KPS cross-linked particles. The inset shows solutions to the density profile of the particles normalized to the shell contrast. Solid line is the solution with $\log \lambda = 2.8$ using second derivative smoothing norm, and the dashed line with $\log \lambda = 2.5$ using total variation smoothing norm.

7.5 Results and Discussion

7.5.1 KPS induces cross-links to the particle periphery leading to core depleted particle structure

To demonstrate the cross-linking capability of the KPS initiator, non-cross-linked PNIPAM particles were prepared using the APS-TEMED redox initiation system. The resulting batch was kept hot and divided to hot aqueous KPS solutions under argon atmosphere without letting the particles cool down below PNIPAM VPTT in between. Hot water was used as a reference. Figure 7.2 shows the form factors of the particles measured in swollen state at 20 °C after 3.5 h incubation in collapsed state at 90 °C.

The lowest featureless form factor in Figure 7.2 shows that particles incubated

in hot water redisperse to fragments of various sizes upon swelling below PNIPAM VPTT (Figure 7.1 case A). In contrast to the particles which only suffered the hot water treatment, KPS incubated particles exhibit signs of cross-linking. With increasing KPS concentration, forward scattering intensifies indicating the increasing molecular weight of the scatterers, and oscillations characteristic of spherical particles emerge.

Given that the surface of the collapsed particles is the most exposed to the hydrogen abstraction of the KPS radicals, one expects the cross-linking density, and the polymer volume fraction, to be the highest at the periphery of the KPS cross-linked microgels. This assumption is supported by comparison of the experimental data to a scattering pattern of a homogeneous sphere with the same mean square radius of gyration as the KPS incubated particles. As can be seen in Figure 7.2, the first maximum of the experimental data protrudes to higher intensity than that of the homogeneous reference particle. This behavior is characteristic of spherical structures that are core depleted, i.e., that are less dense in the core in contrast to the periphery of the particle.

Solutions to the density profile of particles calculated with total variation and 2nd derivative smoothing norms are shown in the inset of Figure 7.2. Both solutions agree with the features already observed in the q space; the polymer volume fraction is the highest at the surface and decays with distance to the core. Total variation smoothing norm characteristically produces a less smooth solution than 2nd derivative smoothing norm; we however assume the latter to be a better approximation to the real density profile as there is no reason to expect a discontinuous particle structure.

It is reasonable to expect that the diffusion of the radicals to the core of the dense collapsed polymer particles becomes increasingly difficult with the radial distance from the surface, and consequently the radicals create more active sites near the surface, which can further react to cross-links. Therefore the cross-linking density decreases continuously with distance towards the core. Upon swelling loosely attached polymer chains (sol fraction) likely diffuse out of the network resulting in a rather sparse structure with an inverted cross-linking distribution in respect to conventional microgels (Figure 7.1 case B).

7.5.2 How strong is the KPS cross-linking effect?

The cross-linking effect of the initiator can be strong enough to exceed the gel point in the particles. The natural question that follows is how the cross-linking density compares to the explicit use of cross-linker, such as BIS. Strong additional cross-linking contribution will affect the particle properties such as mechanical strength, swelling ratio and loading and release characteristics, possibly in detrimental way if not accounted for.

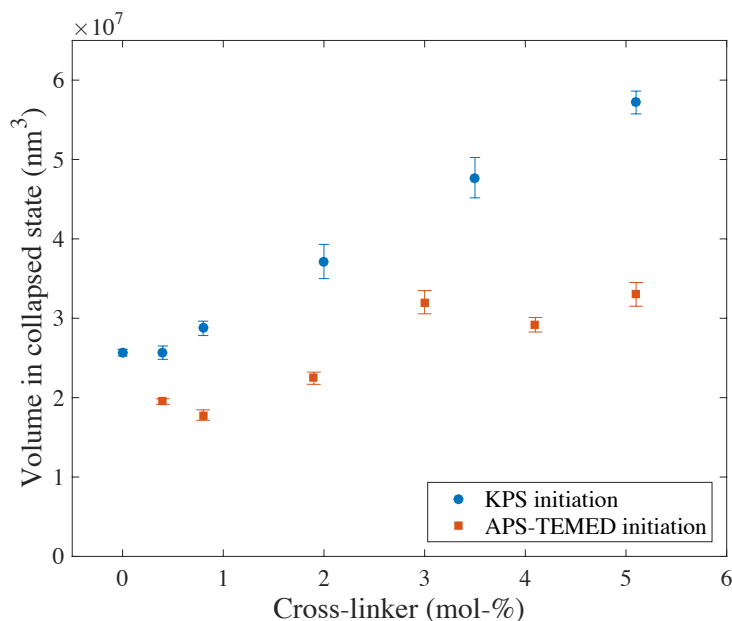


Figure 7.3: Hydrodynamic volume of particles initiated by KPS or APS-TEMED system at 60 °C, measured in the collapsed state at 50 °C. The particles were not let to cool below VPTT between the synthesis and characterization. NIPAM concentration in each batch was $7.1 \times 10^{-2} \text{ mol}\cdot\text{dm}^{-3}$ for KPS initiated batches and $1.5 \times 10^{-1} \text{ mol}\cdot\text{dm}^{-3}$ for APS-TEMED initiated batches to compensate for the faster initiation rate and lack of spontaneous cross-linking. KPS concentration was $3.1 \times 10^{-3} \text{ mol}\cdot\text{dm}^{-3}$ and APS and TEMED concentrations were $3.1 \times 10^{-3} \text{ mol}\cdot\text{dm}^{-3}$ and $4.7 \times 10^{-3} \text{ mol}\cdot\text{dm}^{-3}$, respectively.

As KPS and BIS create cross-links specifically to the periphery and core of the particle, respectively, the cross-linking efficiency of KPS can be accounted for by synthesizing particles with varying BIS concentration but the same KPS concentration. At the point where both contributions are comparable, one expects the particles to have a rather homogenous structure, i.e., similar to that of hard sphere. In the absence of initiator induced cross-links, particles initiated with APS-TEMED system should instead always show a fuzzy microgel structure.

Figure 7.3 shows hydrodynamic volume of KPS and APS-TEMED initiated batches in the collapsed state after the reaction. The particles in the collapsed state are assumed to have homogeneous structure and therefore the volume in the collapsed state reflects the mass of the particles. The molecular weight of the particles clearly increases with the amount of BIS, which we earlier attributed to the decrease of particle number density with BIS concentration.^[45] All the KPS initiated batches appear turbid in swollen state at room temperature (Figure 7.4), which confirms that colloidal particles form even when no additional cross-linker

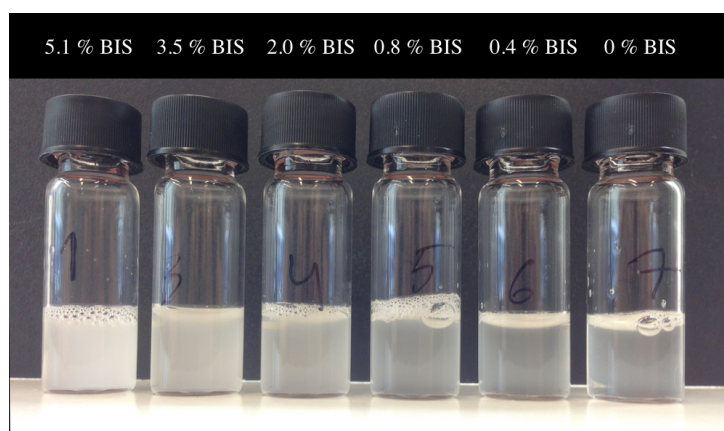


Figure 7.4: Microgel dispersions initiated by KPS after purification by centrifugation at room temperature. Turbidity of the dispersions indicates that colloidal particles are present regardless of the amount of cross-linker BIS in initial the reaction mixture.

is present in the initial monomer mixture.

Figure 7.5 shows the scattering data acquired for the KPS initiated batches. The initial visual inspection reveals that all of the samples have narrow particle size distributions, which can be seen from the multiple distinguished minima throughout the q range. For selected samples form factors of homogeneous spheres with the same mean square radius of gyration are plotted for reference. In the case of 0 mol – % BIS sample, which is the limiting case for the ultra low cross-linked microgels, it can be seen that the first maximum protrudes to higher intensity than that of the homogeneous sphere, which indicates core depleted, or inverted, structure, similar to externally cross-linked particles. For the samples other than 0 mol – % BIS, the form factors decay faster than those of homogeneous spheres, which implies fuzzy sphere structure^[29].

The computed solutions for density profiles of the KPS initiated batches are shown in Figure 7.6. Detailed discussion of the routine's ability to resolve fuzzy structures is included in Supporting Information. Briefly, in a (experimentally) limited q range fuzzy structures generate similar scattering patterns as core shell particles, which is reflected in these reconstructions. All the solutions except with higher than 0.8 mol – % BIS indicate a low density region at the periphery of the particles. This is a generally accepted feature of swollen microgels, which arises from the fact that the cross-linker BIS reacts faster than NIPAM, resulting in higher cross-linking density in the core of the particles (Figure 7.1 case E). The final structure of the microgels is attained when the non-cross-linked sol fraction of the polymer detaches from the gel fraction upon particle swelling below VPTT. The sol fraction has been shown to approach 50% for *N*-isopropylmethacrylamide

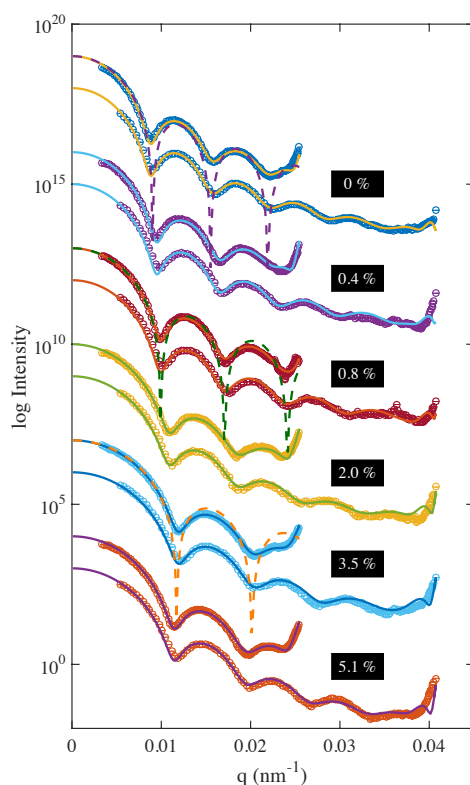


Figure 7.5: KPS initiated batches measured at 20 °C in water. From the top down 0, 0.4, 0.8, 2.0, 3.5, 5.1 mol – % BIS. Two datasets per sample were acquired; datasets belonging to the same sample are grouped together. Solid lines are the global fits to data. Dashed lines show form factors of homogeneous spheres with the same mean square radius of gyration as the corresponding particles.

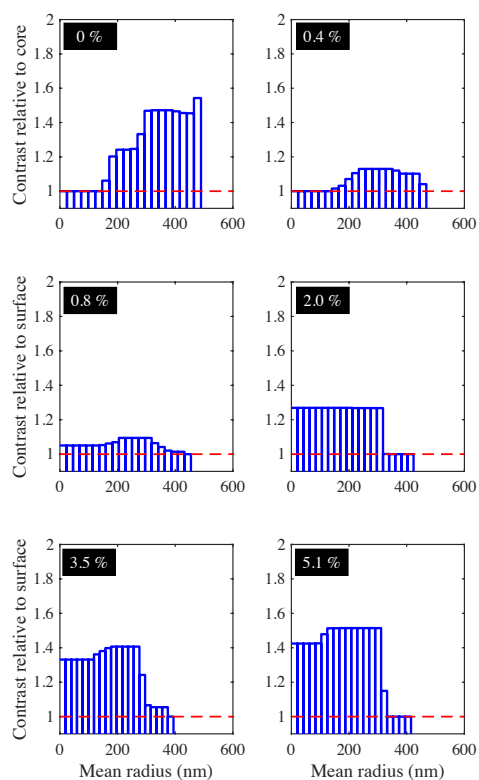


Figure 7.6: Solutions to the density profiles for KPS initiated batches calculated using total variation smoothing norm with 20 point discretization.

particles with 2 mol – % BIS^[48], indicating that the actual gel particles are just rather thin scaffolds in comparison to the mass of the particles in the collapsed state at the end of the polymerization. Stieger et al.^[29] successfully described the resulting swollen, fuzzy particle structure with a radially decaying density profile in their scattering model.

In the lack of additional cross-linker in the batch, we have no mechanistic reason to expect radially decaying density profile. On the contrary, as we have shown, exposure of polymer particles to initiator radicals induces cross-links to the periphery of the particles. Analogously to KPS incubated initially non-cross-linked particles, 0 mol – % BIS particles also exhibit core depleted structure. Because the microgels synthesized by precipitation polymerization grow from the core outwards, it is reasonable to expect that cross-linker free KPS initiated particles always have a certain amount of cross-links in their core due to transfer reactions during the polymerization (Figure 7.1 case D). Given that all the particles in Figure 7.5 were synthesized at 60 °C, this experiment shows that initiator cross-linking is a significant process even at typical synthesis temperatures, in contrast to 90 °C, which was used for incubation.

The inversion routine determines the scattering contrast relative to the outermost layer of the particles. The solutions in Figure 7.6 show that the turn over point from inverted (hollowish) to fuzzy takes gradually place between 0 and 2.0 mol – % BIS. The particles with 0.8 mol – % BIS exhibit a rather homogeneous structure; the difference in the periphery and the core of particles is clearly more pronounced for batches with 2.0 mol – % and higher BIS content, indicating a fuzzy microgel structure. Under these reaction conditions the cross-linking contribution from KPS is comparable to the contribution from BIS for the 0.8 mol – % BIS batch but diminishes rapidly afterwards when cross-linker concentration is increased.

AFM micrographs of 0, 0.4 and 2.0 mol – % BIS batches in Figure 7.7 show that at high surface coverage 0 mol – % BIS particles deform and buckle, whereas buckling is not seen for 0.4 mol – % and higher BIS batches. Buckling was inferred from the non-uniform height profile of the microgel, they exhibit an elevated edge or an ellipsoidal shape deflated in the center. Similar buckled shapes were reported by Bachman et al. in their AFM study on ultra-low cross-linked particles^[22]. Buckling of cross-linker free particles is in line with the static scattering result that indicated the cross-linker free particles having the highest polymer volume fraction (cross-linking density) at the particle surface. As the particle surface is somewhat stiffer and denser in comparison to particle core, the soft spheres adopt a buckled shape whenever a high particle surface density limits their deformation and spreading.

When this spatial constrain is removed 0 mol – % BIS particles demonstrate their high deformability and extensive spreading on the substrate (Figure 7.8).

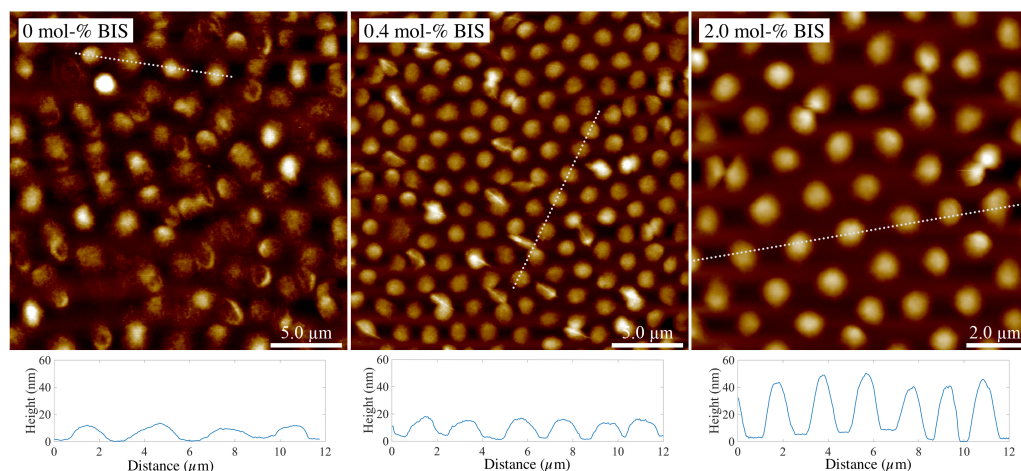


Figure 7.7: AFM micrographs and selected cross-sections of KPS initiated 0, 0.4 and 2.0 mol – % BIS samples at high surface coverage deposited on SiO₂ substrate. The height of the particles on the substrate increase with increasing BIS content, indicating that more polymer is retained in the gel fraction at higher cross-linking degrees.

In the crowded environment the 0 mol – % BIS particles protrude approximately 10 nm from the substrate, whereas on uncrowded substrate the particles spread over several square micrometers and protrude only 3–7 nm from the substrate. No buckling can be observed under these circumstances; however, excessive spreading on the substrate may even cause mechanical failure of the ultrasoft microgels. This is evidenced by the extremely flat, somewhat irregular shapes in Figure 7.8. The form factors in Figure 7.5 show beyond doubt that 0 mol – % BIS particles adopt a spherical shape in dispersion, and their thickness of only 3–7 nm on the substrate indicates that the KPS cross-linked particles possess a thin, vesicle-like geometry in the swollen state. These results contradict the notion of core-localized cross-linking profile, which has been proposed in the literature^[22,49].

7.5.3 All APS-TEMED redox initiated particles exhibit fuzzy structure

Reference measurements for APS-TEMED initiated batches are shown in Figure 7.9 and the solutions to the density profile in Figure 7.10. The BIS fractions were kept the same except the 0 mol – % BIS KPS batch, which was replaced with 0.4 mol – % BIS for obvious reasons. For specific samples the equivalent homogeneous sphere has been plotted; in all the cases the experimental data decays faster than the form factors of homogeneous particles implying fuzzy structures. Reconstructions of the density profiles in Figure 7.10 are compatible with the fea-

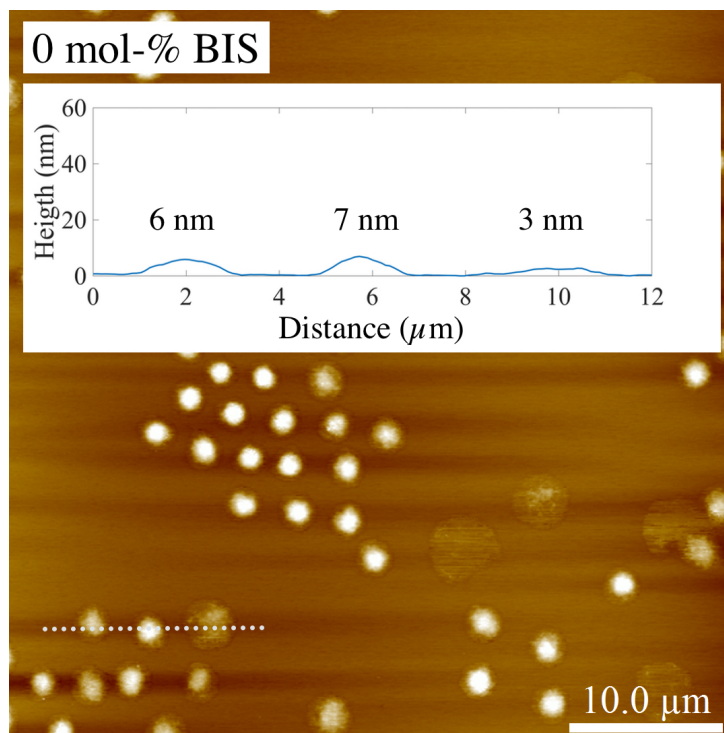


Figure 7.8: AFM micrograph of KPS initiated 0 mol – % BIS sample at low surface coverage.

tures observed in q space; all solutions indicate low density periphery typical of fuzzy microgels.

The two low cross-linker concentration batches 0.4 mol – % and 0.8 mol – % BIS appear to have an extensive low density region in contrast to higher BIS concentration batches. As concluded earlier, at such low BIS contents the cross-linking density resulting from KPS is likely comparable to that of explicit cross-linker, giving more definition to KPS initiated batches. In the lack of KPS, the low BIS concentration in the batch results in an excessively fuzzy structure.

7.5.4 Swelling characteristics of the ultra low cross-linked particles

An important question is whether the high swelling of the ultra low cross-linked microgels is due to the structure of the particles, which qualitatively differs for KPS initiated batches depending on the BIS content, or the overall cross-linking density. Comparison of the swelling capability of KPS and APS-TEMED initiated batches, which always have fuzzy sphere architecture regardless of the amount of

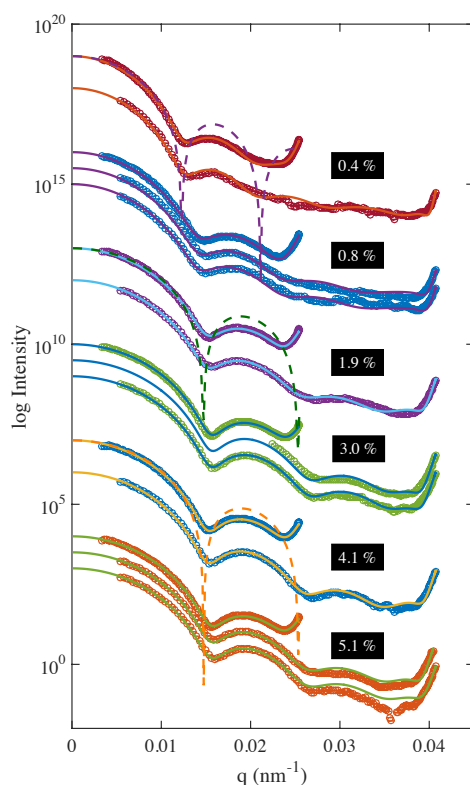


Figure 7.9: APS-TEMED initiated batches measured at 20 °C in water. From the top down 0.4, 0.8, 1.9, 3.0, 4.1, 5.1 mol – % BIS. Minimum two datasets per sample were acquired; datasets belonging to the same sample are grouped together. Solid lines are the global fits to data. Dashed lines show form factors of homogeneous spheres with the same mean square radius of gyration as the corresponding particles.

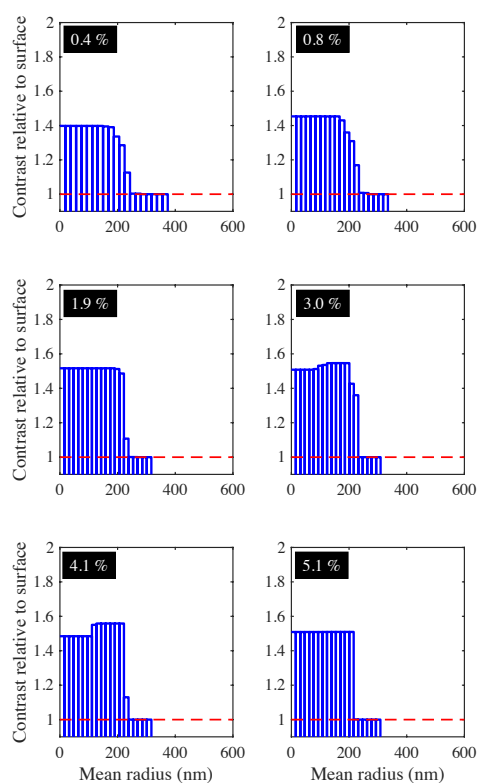


Figure 7.10: Solutions to the density profiles for APS-TEMED initiated batches calculated using total variation smoothing norm with 20 point discretization.

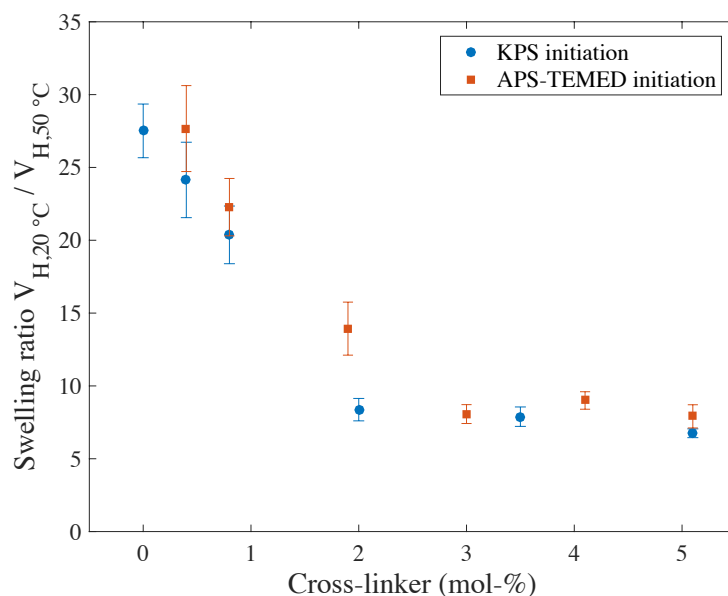


Figure 7.11: Swelling ratio $(R_{H,20^\circ\text{C}}/R_{H,50^\circ\text{C}})^3$ for purified KPS and APS-TEMED initiated batches with the initial cross-linker content in the reaction mixture.

BIS, is shown in Figure 7.11. Interestingly, regardless of initiation method, the swelling ratio of the microgels stays constant at 6-7 above 2 mol – % BIS, but increases rapidly with decreasing BIS content below the 2 mol – % threshold. In the interval of 0 to 2 mol – % BIS the particle structure of the KPS initiated particles changes from inverted to fuzzy, whereas APS-TEMED initiated particles remain fuzzy. Nevertheless high swelling ratios are observed for both particle types, and therefore this behavior cannot be due to the particle architecture but the overall cross-linking density. For KPS initiated batches the change in the particle architecture was not observed to affect the VPTT behavior (Supporting information).

The distinction between particles initiated by initiators that do and do not induce cross-links on the particle periphery should be kept in mind in experimental design. APS-TEMED initiated particles adhere to the conventional notion of PNIPAM microgels. These particles always exhibit a fuzzy sphere structure, where the overall particle density is controlled by the amount of explicit cross-linker in the batch. In contrast, a series of particles initiated by KPS with varying BIS concentration not only have an additional cross-linking contribution from the persulfate initiator, but also change particle architecture at low BIS end of the spectrum. Persulfate initiated batches (we have also confirmed this effect for ammonium persulfate), start as sparse, inverted, structures if no cross-linker is used, go through a rather homogeneous structure at the point where persulfate and BIS contribu-

tions are comparable, and end up in fuzzy sphere structure when the cross-linking contribution of BIS is higher than that of the persulfate initiator. These considerations are important for works that investigate microgel properties as a function of cross-linker content in order to avoid misinterpretation of data.

7.6 Conclusions

In this contribution we investigated the structure of ultra low cross-linked, deformable PNIPAM microgels, which are synthesized by cross-linker free precipitation polymerization. Static light scattering data showed that these particles possess an inverted polymer volume fraction profile in contrast to conventional microgels, i.e., polymer density in the particles was the highest close to the particle surface and decayed radially towards the core. SFM micrographs of the same particles revealed buckled shapes at high surface coverage, which supports the idea of an ultra soft microgel consisting of a thin shell. This result contradicts the earlier notion according to which cross-linker free synthesis results in weakly cross-linked conventional microgel particle structure. Incubation of non-cross-linked PNIPAM particles in aqueous KPS solutions at elevated temperatures showed that the core-depleted structure can be attributed to the hydrogen abstraction induced surface cross-linking by the KPS radicals at the late stages of the reaction. Increasing the cross-linker content gradually showed that the crosslink density from the initiator cross-linking corresponded to use of less than 1 mol – % BIS in our specific case. Under typical polymerization conditions one should be aware that synthesis below 1 mol – % threshold can lead to untypical particle structure, and can have consequences regarding the intended application of the particles as many properties of microgels are determined by the cross-linking distribution.

Understanding the structure of cross-linker free PNIPAM microgels may open the way for further applications. Hollow microgel particles^[17,18,19] have attracted interest due to their high deformability at interfaces^[20] and possible transport properties. Ultra low cross-linked particles might share some of the properties of the hollow particles, with the benefit of being easy to synthesize in a simple batch process. As we have shown, it is also possible to synthesize non-cross-linked monodisperse PNIPAM particles, which dissolve to the solution upon cooling below PNIPAM VPTT. A straightforward step further would be to use these particles as scaffolds for hollow microgels in two step batch process. Typically inorganic cores, which require harsh and cumbersome removal processes, are used for this purpose.

7.7 Supporting Information

7.7.1 Mie scattering

Rayleigh-Debye-Gans (RDG) theory is applicable only if the electric field of the incident radiation thoroughly penetrates the particles of interest, i.e., if the magnitude of the electric field vector inside and around the particle is identical to the incident wave^[50]. If this is not the case, the scattered field has to be calculated using Mie equations^[51], which significantly complicates the situation.

Glatter^[50] writes that for the RDG theory to be applicable, the particles must not reflect the incoming light and the phase shift caused by the particles must be negligible. For this to be the case $2\alpha|m - 1| \ll 1$, where α is a parameter related to the size of the particles

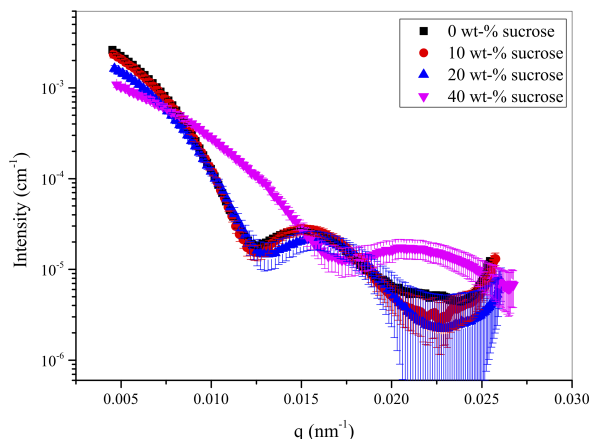
$$\alpha = \frac{2\pi R}{\lambda_0} \quad (7.15)$$

with R the radius of the particle and λ_0 wavelength of the incident beam in vacuum, and m is the ratio of real parts of the refractive indices of the particle and solvent.

For scattering experiment with laser wavelength of 633 nm involving pure polystyrene (PS) particles in water, $m = 1.587^{[52]}/1.332 = 1.191$. Calculations by Glatter^[50] show that Mie effects for such ratio and particles with radii of several hundred nanometers would be likely observable as smearing of the form factor minima and their slight shift towards smaller q values.

In contrast to PS particles, PNIPAM microgels are hydrogel particles extensively swollen by the solvent. Stieger et al.^[29] found that the volume fraction of polymer inside PNIPAM particles in the swollen state is typically 20 % and below. We can estimate the m ratio for PNIPAM particles by a simple back of the envelope calculation. Assuming the refractive index for PNIPAM is of the same magnitude as that of poly(methylmethacrylate), $n = 1.489^{[52]}$ at 633 nm and that the refractive index of the overall particle can be described by a simple superposition, $m \approx (0.2 \cdot 1.489 + 0.8 \cdot 1.332)/1.332 = 1.024$. Given that $m = 1.000$ is the ideal value for RDG regime, we expect that the Mie effects for the swollen microgels used in this work are negligible or small. Given that particle counting from scanning electron micrographs showed that the PDI of the particle radius distributions were 10 % and below, the experimentally measured form factors should have been significantly more smeared out in the case that strong Mie effects are present.

Nevertheless we attempted a contrast matching experiment with 7.2 mol – % BIS KPS particles in aqueous sucrose solutions to see whether the form factors



Supporting Figure 7.12: 7.2 mol – % KPS batch measured in water and at various sucrose concentrations at 642 nm.

would become less smeared when the solvent refractive index was increased, i.e. the refractive index difference between particles and solvent was made smaller.

Supporting Figure 7.12 shows scattered intensity from 7.2 mol – % KPS batch at various sucrose concentrations. The highest BIS content batch was chosen as reference as it is expected to have the highest polymer volume fraction and therefore exhibit the strongest Mie effects, if present. For particles with lower BIS contents, these effects would be expected to be smaller. As seen in Supporting Figure 7.12, the overall scattering intensity diminishes with increasing sucrose concentration, as expected for lowering contrast. The problem proves to be the fact that sucrose forces the water out of the hydrogel particles, and consequently they shrink at high sucrose concentrations. This makes it impossible to evaluate reliably whether the form factors become sharper with diminishing contrast, even though this does not appear to be the case. Based on considerations presented here, we conclude that any Mie effects, if present, are small and do not change the overall interpretation of the results presented in this work.

7.7.2 Test cases

Introduction

The performance of the direct inversion method was evaluated by inverting artificial test datasets that simulate real world data to different degrees. All the datasets include permutations typical of a light scattering measurements, such as incorrect

background subtraction (the actual background was higher than what was subtracted), shifts in laser wavelengths and dispersion refractive indices in respect to their nominal values, higher number of integration points for the particle radius distribution (150 vs 50) and the excess contrast profile (150 vs 20). In addition Gaussian PSD was used for the radius distribution function whereas Burr Type XII distribution were used for fitting. These permutations lead to wrong q values, additional background in the data and introduce a small model mismatch.

Inversion method was tested against two particle types: I) fuzzy sphere conforming to the classical notion of PNIPAM microgel structure and II) partially hollow fuzzy sphere, each with three different noise levels (scaled Poisson noise). These particle types were chosen to investigate whether the assumed characteristics of our actual samples would be detectable by the direct inversion method. Furthermore, in order to compare the suitability of different smoothing norms on these specific particle structures, all datasets were fitted with total variation and 1st and 2nd derivative smoothing norms.

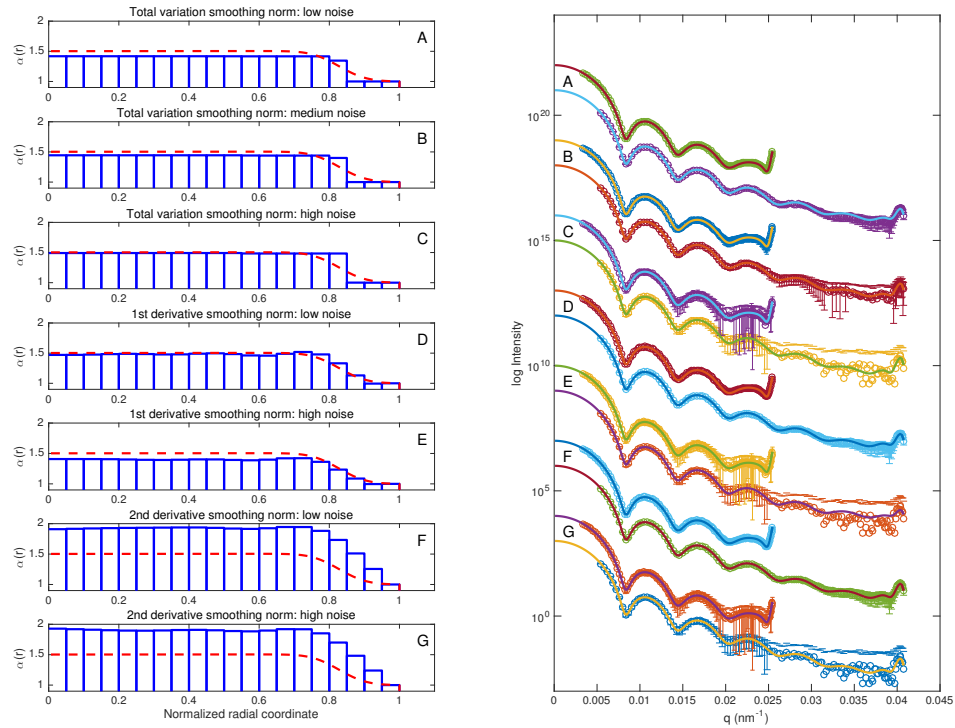
For each test problem and noise level two form factors were created, one with nominal wavelength of 642 nm and another one with 404 nm. For each noise level both traces were fitted globally and the regularization parameter λ values were varied in order to find out the optimal level of filtering according to the L-curve criterion^[39].

Fuzzy sphere particles

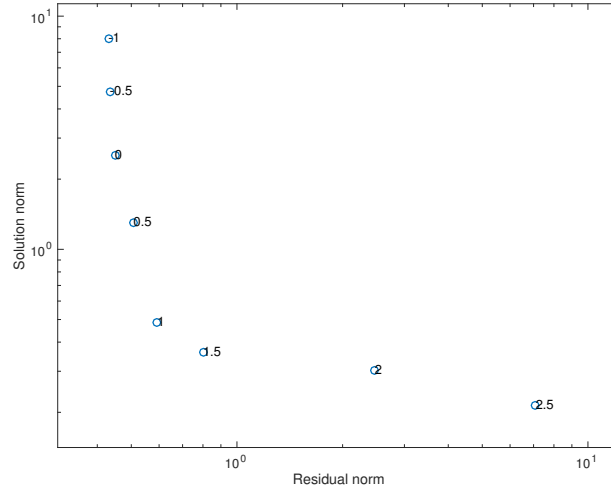
Supporting Figure 7.13 shows the generated datasets, fits, solutions and the exact solution for the fuzzy sphere test problem. Typical L-curve is shown in Supporting Figure 7.14 (test case D in Supporting Figure 7.13). For all the solutions the λ value was chosen close to the L-curve corner, from the right hand side.

Supporting Figure 7.13 shows that all the smoothing norms capture the essence of the exact solution for all the used noise levels, i.e., the constant density core and low density periphery of the fuzzy particle. The details of the solutions reveal distinctive characteristics of the different smoothing norms. Total variation smoothing norm can accommodate steep gradients, and consequently the solutions are reduced to their bare minimum. Fuzzy particles appear as core-shell structure with less dense shell in comparison to the core. This simplicity of solutions is generally preferable, as the solution contains the minimum amount of features to fit the data and therefore the details of the solution are less likely to be artifacts^[53].

The first derivative smoothing norm clearly produces the most faithful reproduction of the exact solution. At low noise level the relative contrast difference between the particle core and particle periphery is estimated correctly, whereas at high noise level it is somewhat underestimated. This is understandable as the increased noise in combination with filtering gives less weight to high q data points.



Supporting Figure 7.13: Solutions (left) and form factor fits (right) to the fuzzy sphere test problem. Dashed red line in the solutions denotes the exact solution that was used to create the test cases. Solid lines on the right indicate the fit function. Solutions to test cases A-C were obtained with total variation smoothing norm, D-E with 1st derivative smoothing norm and F-G with 2nd derivative smoothing norm. Relative noise levels in test cases were A: 1.7×10^{-4} and 2.3×10^{-4} , B: 6.1×10^{-4} and 6.4×10^{-4} , C: 1.9×10^{-3} and 2.8×10^{-3} , D: 1.7×10^{-4} and 2.3×10^{-4} , E: 1.9×10^{-3} and 2.8×10^{-3} , F: 1.7×10^{-4} and 2.3×10^{-4} , G: 1.9×10^{-3} and 2.8×10^{-3} .



Supporting Figure 7.14: L-curve for test case D in Supporting Figure 7.13. Numbers beside the points denote the $\log \lambda$ value.

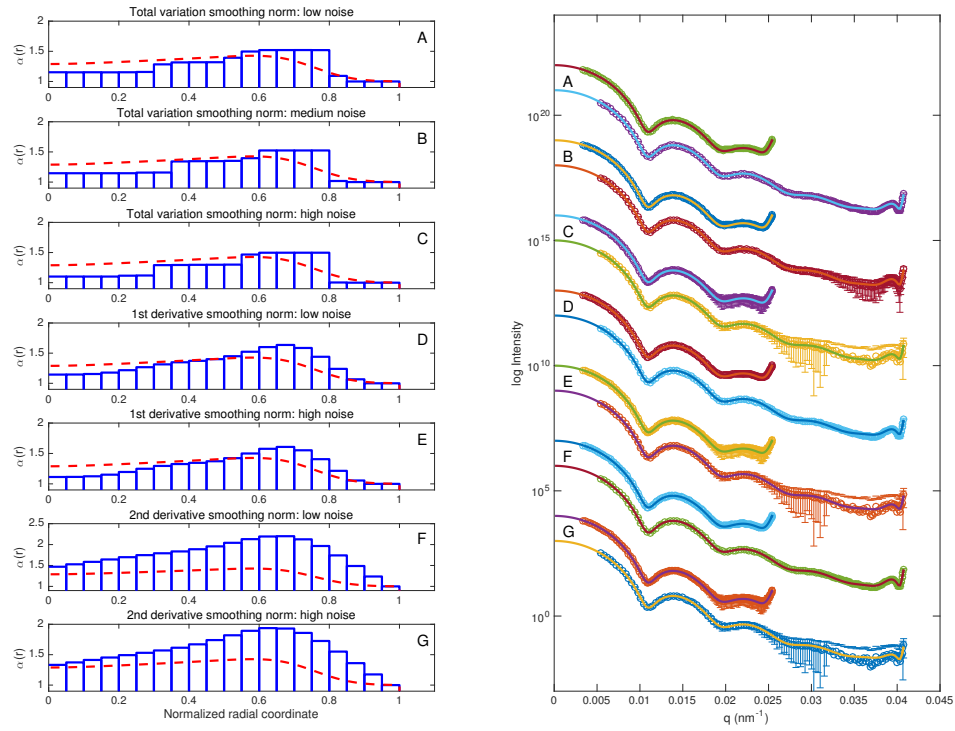
Fuzzy particles are characterized by the fast decay of the form factor^[29], and disregarding the high q data reduces the apparent fuzziness. Finally, the second derivative smoothing norm forces excessive smoothness, which leads to overestimation of the relative difference between the particle core and particle periphery, but nevertheless captures correctly the overall particle structure.

Partially hollow fuzzy sphere particles

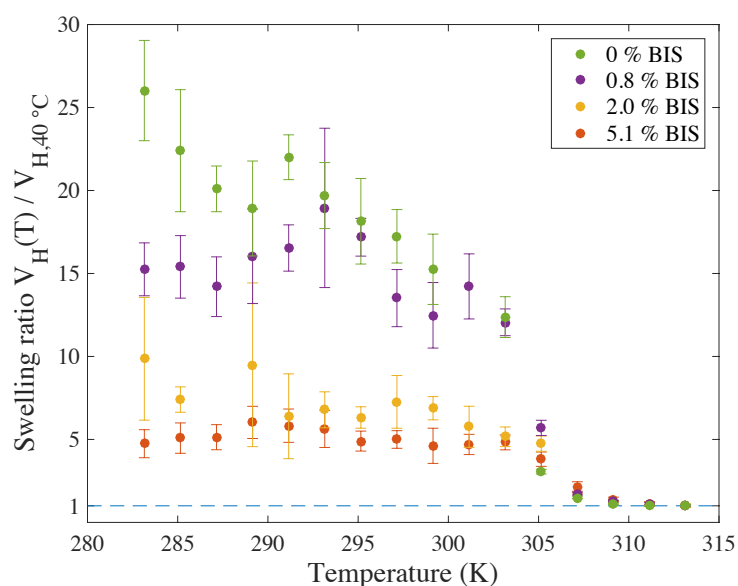
Supporting Figure 7.15 shows the solutions and fits for the partially hollow fuzzy particle test problem. Generally this test problem proves to be more challenging for the inversion routine, but the main features come across for all the noise levels and smoothing norms. All the solutions tend to overestimate the relative excess contrast function at the maximum and underestimate it at the core. The second derivative smoothing norm suffers from the same problem as in the fuzzy sphere test case, i.e., the relative excess contrast function is overestimated because of insufficient flexibility due to excessive smoothing.

Conclusion

Both the test cases, fuzzy sphere and partially hollow fuzzy sphere structures, show that the direct inversion method is able to resolve the main features of this type of particles in the presence of noise and permutations. The recovered relative



Supporting Figure 7.15: Solutions (left) and form factor fits (right) to the partially hollow fuzzy sphere test problem. Dashed red line in the solutions denotes the exact solution that was used to create the test cases. Solid lines on the right indicate the fit function. Solutions to test cases A-C were obtained with total variation smoothing norm, D-E with 1st derivative smoothing norm and F-G with 2nd derivative smoothing norm. Relative noise levels in test cases were A: 1.3×10^{-4} and 1.1×10^{-4} , B: 4.5×10^{-4} and 5.1×10^{-4} , C: 1.8×10^{-3} and 1.9×10^{-3} , D: 1.3×10^{-4} and 1.1×10^{-4} , E: 1.8×10^{-3} and 1.9×10^{-3} , F: 1.3×10^{-4} and 1.1×10^{-4} , G: 1.8×10^{-3} and 1.9×10^{-3} .



Supporting Figure 7.16: Volume phase transition behavior of selected KPS initiated batches.

excess contrast functions do not necessarily provide "exact" reconstructions but are sufficient to classify particles based on main characteristics. It is clear that one should avoid the interpretation of minute details of the solutions. In this respect the total variation smoothing norm provides the best compromise between obtaining a useful reconstruction but avoiding artifacts resulting from the inversion process.

7.7.3 Volume phase transition behavior of ultra low cross-linked particles

Supporting Figure 7.16 shows the volume phase transition behavior of 0, 0.8, 2.0 and 5.1 mol – % KPS initiated batches. Relatively high error in the hydrodynamic volumes of batches with low cross-linker amount is due to large swollen size and low scattering contrast at low temperatures. Regardless of cross-linker content the most rapid collapse takes place between 305 and 307 K, where PNIPAM VPTT is typically reported.^[2] The particle architecture changes from inverted to fuzzy between 0 and 2.0 mol – %, but the difference in the particle structure does not affect the VPTT behavior.

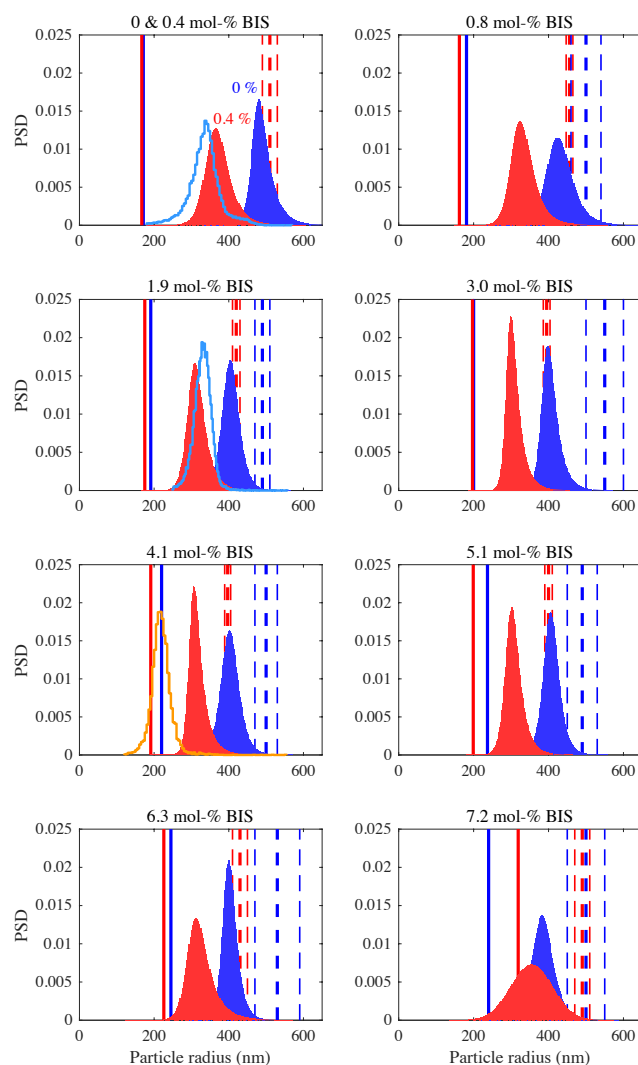
7.7.4 Is Gaussian function a good approximation for the radius distribution?

The particle nucleation phase in precipitation polymerization of NIPAM appears to be sensitive to the charge density of polymer generated under given polymerization conditions^[45], and its duration has to be short, which can be deduced from the fact that the experimentally observed particle size distributions are narrow. Consequently also no particle aggregation take place under typical reaction conditions.

The exact shape of the radius size distribution function is determined by the nucleation mechanism and the ability of different size fractions to capture material in the subsequent growth phase. In previous work Gaussian approximation has been used for the radius size distribution function in microgel form factor fitting^[29]. Particle radius distributions fitted using Burr type XII distribution, are shown in Supporting Figure 7.17. Numerical values are given in Table 7.1. Especially for APS-TEMED initiated batches (red histograms), the optimization routine finds slightly right tailed solutions. KPS initiated batches (blue histograms) appear to retain their polydispersity regardless of the cross-linker concentration in the batch, typically under 10 %, whereas APS-TEMED initiated batches seem to have minimum polydispersity at below 10 % between 1.9 and 5.1 mol – % BIS. It is possible that particle nucleation differs between KPS and APS-TEMED initiated batches because of different cross-linking characteristics of these systems and initiation rate, which is typically an order of magnitude higher for redox initiation^[54] in comparison to thermally decomposing initiator.

Hydrodynamic radii measured in the swollen state (dashed red and blue lines in Supporting Figure 7.17 for APS-TEMED and KPS initiated batches, respectively) align with the largest particle size fractions of the corresponding particle size distributions. This is to be expected for two reasons. First, correlograms could be acquired only at low q because of the fast decay of form factors. In this region the scattered intensity is dominated by the large particle size fractions due to the underlying physical process, leading to apparent hydrodynamic radii reflecting this bias. Second, hydrodynamic interactions of the particles are strongly affected by the dangling chains at the surface, increasing the apparent hydrodynamic radius further.

For selected batches particles were dried on wafer and imaged with scanning electron microscope in an effort to obtain more insight into the shape of the particle size distributions. For batches 0 and 1.9 mol – % KPS the radii of 22414 and 18390 particles were automatically counted; for batch 4.1 mol – % APS-TEMED 8787 particles were counted. Large particle counts are necessary to obtain meaningful statistics. The particle count histograms are included in Supporting Figure 7.17, representative examples of micrographs are shown in Supporting Figure



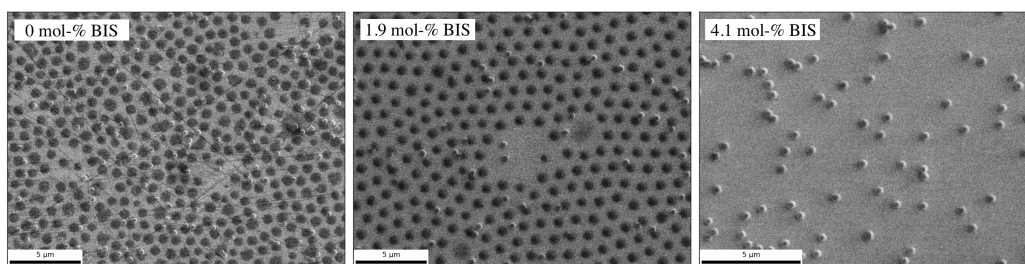
Supporting Figure 7.17: Particle size distributions from the fit data. Dark blue and red denote distributions from KPS and APS-TEMED initiated batches at 20 °C, respectively. Vertical solid lines with the same color coding show the mean hydrodynamic radii in the collapsed state measured by DLS at 50 °C. Dashed thick and thin lines denote hydrodynamic radii and corresponding standard deviations measured at 20 °C. Light blue and orange histograms are the results from SEM image analysis for KPS and APS-TEMED initiated batches in dry state, respectively.

Supporting Table 7.1: Particle size parameters for KPS and APS-TEMED (A-T) initiated batches. The KPS batches are different than those presented in the paper. Mean and PDI are the values in swollen state at 20 °C obtained from the inversion routine. Hydrodynamic radii with standard deviations were determined experimentally for all particles in collapsed state at 50 °C and for APS-TEMED initiated batches in swollen state at 20 °C. The swollen hydrodynamic radii contain significant systematic error due to the physics of the scattering process; see text for discussion.

Initiator	BIS (%)	Mean _{20°C} (nm)	PDI (%)	$R_{h,50°C}$ (nm)	$R_{h,20°C}$ (nm)
KPS	0	492	7	171 ± 2	-
KPS	0.8	432	10	181 ± 1	500 ± 40
KPS	1.9	406	7	191 ± 3	490 ± 20
KPS	3.0	407	7	200 ± 4	550 ± 50
KPS	4.1	404	7	220 ± 2	500 ± 30
KPS	5.1	408	6	237 ± 2	490 ± 40
KPS	6.3	404	6	245 ± 1	530 ± 60
KPS	7.2	386	9	240 ± 2	500 ± 50
A-T	0.4	374	10	167 ± 1	510 ± 20
A-T	0.8	334	11	162 ± 2	456 ± 9
A-T	1.9	317	9	175 ± 2	420 ± 10
A-T	3.0	309	8	197 ± 3	395 ± 9
A-T	4.1	317	8	191 ± 2	397 ± 8
A-T	5.1	308	8	199 ± 3	400 ± 10
A-T	6.3	326	12	226 ± 2	430 ± 20
A-T	7.2	356	15	319 ± 7	490 ± 20

7.18.

The particle radii obtained in dry state on wafer are clearly smaller than those obtained from the fit routine at the swollen state and appear symmetric. For KPS initiated batches however, the mean dry radius is clearly far away from the collapsed hydrodynamic radius recorded at 50 °C. This discrepancy can be explained by the deformation of the microgels on the wafer: Particles with low cross-linking densities have low mechanical strength, which makes them highly deformable. The deformation of microgel particles in dry and wet states on substrate has been reported in many contexts^[30,31,3,4,5,32,33,22,34]. This can be especially expected in the case for the core-depleted particles, which lack internal support. Interaction with the substrate causes them to spread on the wafer (Supporting Figure 7.18, 0 and 1.9 mol – % BIS), drastically increasing the apparent radius when imaged from above. The deformation is a non-trivial non-linear process, and therefore we do not expect the particle radius distribution in the dry state on the wafer directly



Supporting Figure 7.18: Scanning electron micrographs from 0 mol – % BIS KPS, 1.9 mol – % BIS KPS and 4.1 mol – % BIS APS-TEMED. In micrographs A and B contamination from the preparation is visible, but these small particles could be easily excluded from the particle counting. Low cross-linking density batches are spread on the wafer whereas 4.1 mol – % particles protrude from the substrate. Cross-link density in 0 mol – % BIS KPS is low, as the scratches in the substrate show through the particles.

reflect the distribution in the swollen state.

The mean of the distribution for 4.1 mol – % APS-TEMED is in the close vicinity of the solid red line denoting the hydrodynamic radius in the collapsed state. The higher cross-linking density in this batch enhances the mechanical strength of the particles and consequently they do not deform as strongly on the wafer in the dry state^[3]. This is also visible in Supporting Figure 7.18, where the 4.1 mol – % APS-TEMED particles clearly protrude from the substrate. The dry state distribution also looks symmetric, as do the KPS histograms, whereas the solution obtained by the fit routine is slightly right skewed. Similar SEM histograms were obtained by von Nessen et al.^[55], with approximately 300 particles per histogram. To summarize, the experimental data shows that the distributions are monomodal and close to symmetric, but further theoretical and improved experimental work are required to settle the matter in the future. The best approach will be likely particle counting from cryo-TEM micrographs, where particle dimensions are not distorted by the interaction with substrate.

Bibliography

- [1] R. H. Pelton and P. Chibante, *Colloids and Surfaces*, 1986, **20**, 247–256.
- [2] R. Pelton, *Advances in Colloid and Interface Science*, 2000, **85**, 1–33.
- [3] S. Schmidt, H. Motschmann, T. Hellweg and R. von Klitzing, *Polymer*, 2008, **49**, 749–756.
- [4] C. D. Sorrell and L. A. Lyon, *Langmuir*, 2008, **24**, 7216–7222.
- [5] A. Burmistrova and R. von Klitzing, *J. Mater. Chem.*, 2010, **20**, 3502–6.
- [6] A. Burmistrova, R. Steitz and R. von Klitzing, *Chemphyschem*, 2010, **11**, 3571–3579.
- [7] S. Schmidt, M. Zeiser, T. Hellweg, C. Duschl, A. Fery and H. Möhwald, *Adv. Funct. Mater.*, 2010, **20**, 3235–3243.
- [8] Y. Xia, X. He, M. Cao, C. Chen, H. Xu, F. Pan and J. R. Lu, *Biomacromolecules*, 2013, **14**, 3615–3625.
- [9] M. J. Serpe, J. Kim and L. A. Lyon, *Adv. Mater.*, 2004, **16**, 184–187.
- [10] W. Richtering, *Langmuir*, 2012, **28**, 17218–17229.
- [11] S. Wiese, A. C. Spiess and W. Richtering, *Angew. Chem. Int. Ed.*, 2012, **52**, 576–579.
- [12] V. Schmitt and V. Ravaine, *Current Opinion in Colloid and Interface Science*, 2013, **18**, 532–541.
- [13] S. Wellert, M. Richter, T. Hellweg, R. von Klitzing and Y. Hertle, *Zeitschrift für Physikalische Chemie*, 2015, **229**, 1–26.
- [14] Z. Li, D. Harbottle, E. Pensini, T. Ngai, W. Richtering and Z. Xu, *Langmuir*, 2015, **31**, 6282–6288.
- [15] O. S. Deshmukh, D. van den Ende, M. C. Stuart, F. Mugele and M. H. G. Duits, *Advances in Colloid and Interface Science*, 2015, **222**, 215–227.
- [16] Y. Guan and Y. Zhang, *Soft Matter*, 2011, **7**, 6375.
- [17] V. Lapeyre, N. Renaudie, J.-F. Dechezelles, H. Saadaoui, S. Ravaine and V. Ravaine, *Langmuir*, 2009, **25**, 4659–4667.

- [18] J. Dubbert, T. Honold, J. S. Pedersen, A. Radulescu, M. Drechsler, M. Karg and W. Richtering, *Macromolecules*, 2014, **47**, 8700–8708.
- [19] R. Contreras-Cáceres, L. Schellkopf, C. Fernández-López, I. Pastoriza-Santos, J. Pérez-Juste and M. Stamm, *Langmuir*, 2015, **31**, 1142–1149.
- [20] K. Geisel, A. A. Rudov, I. I. Potemkin and W. Richtering, *Langmuir*, 2015, **31**, 13145–13154.
- [21] Z. Meng, M. H. Smith and L. A. Lyon, *Colloid and Polymer Science*, 2009, **287**, 277–285.
- [22] H. Bachman, A. C. Brown, K. C. Clarke, K. S. Dhada, A. Douglas, C. E. Hansen, E. Herman, J. S. Hyatt, P. Kodlekere, Z. Meng, S. Saxena, M. W. Spears Jr, N. Welsch and L. A. Lyon, *Soft Matter*, 2015, **11**, 2018–2028.
- [23] T. J. Merkel, S. W. Jones, K. P. Herlihy, F. R. Kersey, A. R. Shields, M. Napier, J. C. Luft, H. L. Wu, W. C. Zamboni, A. Z. Wang, J. E. Bear and J. M. DeSimone, *Proceedings of the National Academy of Sciences of the United States of America*, 2011, **108**, 586–591.
- [24] S. Berger, H. Zhang and A. Pich, *Adv. Funct. Mater.*, 2009, **19**, 554–559.
- [25] G. Agrawal, A. Ülpenich, X. Zhu, M. Möller and A. Pich, *Chem. Mater.*, 2014, **26**, 5882–5891.
- [26] T. Kureha, T. Sato and D. Suzuki, *Langmuir*, 2014, **30**, 8717–8725.
- [27] L. V. Sigolaeva, S. Y. Gladyr, A. P. H. Gelissen, O. Mergel, D. V. Pergushov, I. N. Kurochkin, F. A. Plamper and W. Richtering, *Biomacromolecules*, 2014, **15**, 3735–3745.
- [28] L. V. Sigolaeva, O. Mergel, E. G. Evtushenko, S. Y. Gladyr, A. P. H. Gelissen, D. V. Pergushov, I. N. Kurochkin, F. A. Plamper and W. Richtering, *Langmuir*, 2015, **31**, 13029–13039.
- [29] M. Stieger, J. S. Pedersen, W. Richtering and P. Lindner, *Journal of Chemical Physics*, 2004, **120**, 6197–6206.
- [30] S. Höfl, L. Zitzler, T. Hellweg, S. Herminghaus and F. Mugele, *Polymer*, 2007, **48**, 245–254.
- [31] O. Tagit, N. Tomczak and G. J. Vancso, *Small*, 2008, **4**, 119–126.

- [32] S. Wellert, Y. Hertle, M. Richter, M. Medebach, D. Magerl, W. Wang, B. Demé, A. Radulescu, P. Müller-Buschbaum, T. Hellweg and R. von Klitzing, *Langmuir*, 2014, **30**, 7168–7176.
- [33] F. Schneider, A. Balaceanu, A. Feoktystov, V. Pipich, Y. Wu, J. Allgaier, W. Pyckhout-Hintzen, A. Pich and G. J. Schneider, *Langmuir*, 2014, **30**, 15317–15326.
- [34] S. Wellert, D. Kesal, S. Schön, R. von Klitzing and K. Gawlitza, *Langmuir*, 2015, **31**, 2202–2210.
- [35] J. Gao and B. J. Frisken, *Langmuir*, 2003, **19**, 5212–5216.
- [36] J. Gao and B. J. Frisken, *Langmuir*, 2003, **19**, 5217–5222.
- [37] *Neutrons, X-rays and Light: Scattering Methods Applied to Soft Condensed Matter*, ed. P. Lindner and T. Zemb, Amsterdam: North Holland Delta Series, 2002.
- [38] J. S. Pedersen, *Advances in Colloid and Interface Science*, 1997, **70**, 171–210.
- [39] P. C. Hansen, *Discrete inverse problems: insight and algorithms*, Society for Industrial and Applied Mathematics, Philadelphia, 2010.
- [40] O. Glatter, *J Appl Crystallogr*, 1977, **10**, 415–421.
- [41] D. I. Svergun and IUCr, *J Appl Crystallogr*, 1992, **25**, 495–503.
- [42] O. Glatter, *J Appl Crystallogr*, 1981, **14**, 101–108.
- [43] O. Glatter and B. Hainisch, *J Appl Crystallogr*, 1984, **17**, 435–441.
- [44] O. L. J. Virtanen and W. Richtering, *Colloid and Polymer Science*, 2014, **292**, 1743–1756.
- [45] O. L. J. Virtanen, H. M. Ala-Mutka and W. Richtering, *Macromol. Chem. Phys.*, 2015, **216**, 1431–1440.
- [46] E. Jones, T. Oliphant, P. Peterson and others, *SciPy: Open source scientific tools for Python*, 2001.
- [47] S. van der Walt, J. L. Schonberger, J. Nunez-Iglesias, F. Boulogne, J. D. Warner, N. Yager, E. Gouillart, T. Yu and S. I. Contributors, *scikit-image: image processing in Python*, 2014, <https://peerj.com/articles/453>.

- [48] D. Duracher, A. Elaissari and C. Pichot, *Journal of Polymer Science Part A Polymer Chemistry*, 1999, **37**, 1823–1837.
- [49] A. C. Brown, S. E. Stabenfeldt, B. Ahn, R. T. Hannan, K. S. Dhada, E. S. Herman, V. Stefanelli, N. Guzzetta, A. Alexeev, W. A. Lam, L. A. Lyon and T. H. Barker, *Nat Mater*, 2014, **13**, 1108–1114.
- [50] O. Glatter, *Neutrons, X-rays and Light: Scattering Methods Applied to Soft Condensed Matter*, Amsterdam: North Holland Delta Series, 2002.
- [51] G. Mie, *Annalen der Physik*, 1908, **25**, 377–445.
- [52] N. Sultanova and S. Kasarova, *Acta Physica Polonica- ...*, 2009.
- [53] S. W. Provencher, *Computer Physics Communications*, 1982, **27**, 213–227.
- [54] G. Odian, *Principles of Polymerization*, Wiley Interscience, 4th edn, 2004.
- [55] K. von Nessen, M. Karg and T. Hellweg, *Polymer*, 2013, **54**, 5499–5510.

8. Conclusions and outlook

Poly(*N*-isopropylacrylamide) (PNIPAM) microgels lie in the intersection of several scientific fields, which makes them a rich and rewarding topic. Manufacturing these particles is a subject well within polymer and colloid chemistry. Properties of the particles, their behavior and interaction with the surroundings are problems related to polymer physics, physical chemistry and colloid science. The ability of the microgels to change size in response to changing environment or other stimuli has been used in various applications related to material science and biology. Many of the applications have been listed in the preceding chapters.

Synthesis of these particles is deceptively simple; heating deoxygenized aqueous *N*-isopropylacrylamide (NIPAM) solution over the lower critical solution temperature (LCST) of PNIPAM and initiating the solution with a radical source leads to formation of monodisperse particles. However, a variety of sophisticated physical aspects and chemical processes are in play during the formation of microgels. These include the chain growth, transfer reactions, phase behavior of PNIPAM and colloidal stability of the polymer particles. The structure of microgels is in addition affected by the cross-link distribution, which is decisive for the radial polymer volume fraction inside the particles after the sol fraction has been removed.

The objective of this work was to address open questions regarding the polymerization and particle formation mechanism in a microgel synthesis, with emphasis on the connection of these two. Three important discoveries were made:

1) The final particle volume of microgels exhibit power law behavior in respect to batch monomer and initiator concentration. The final particle volume in the collapsed state after the reaction was shown to increase with $5/3$ power in respect to NIPAM concentration, and decrease with $-4/3$ power in respect to ammonium persulfate concentration (APS) when constant amount of accelerator *N,N,N',N'*-tetramethylethylenediamine (TEMED) was present. The power law behavior was explained by accumulation rate of ionic initiator fragments that accumulate to the polymer, effectively regulating the particle stabilization and therefore the number

of particles under given reaction conditions.

2) Furthermore, strong evidence was collected in support of the early precipitation polymerization following radical solution polymerization mechanism. Polymerization rate, defined as the disappearance rate of the monomer ($-d[M]/dt$) typically shows power law dependence on the monomer and initiator concentration. *In situ* 3D-DLS and reaction calorimetric measurements effectively gave the power law exponents as 1 and 1/2 for NIPAM and initiator concentration, respectively, which is the expected result for radical solution polymerization.^[1,2] *In situ* small-angle neutron scattering (SANS) experiments revealed the particle growth to follow pseudo-first order kinetics, which implies that the instantaneous reaction rate is regulated by the available unreacted monomer, and consumption of initiator during the reaction is typically negligible. In addition, *in situ* 3D-DLS measurement did not show difference in the reaction rates when the particle number density was increased with the surfactant sodium dodecyl sulfate, effectively excluding emulsion polymerization mechanism. This behavior has been also reported in earlier work.^[3] The kinetic scheme of the polymerization reaction is the underlying mechanism that explains the power law behavior of the final particle size.

3) Finally, it was shown that peroxide initiators may gelate the microgel surface. Multiple authors have obtained stable gel particles without using multifunctional comonomer by initiating a NIPAM solution with standard peroxide initiators.^[4,5,6,7] In this work it was shown by elaborate static light scattering experiments that such particles have an inverted cross-linking structure, i.e., the highest polymer volume fraction is located at the surface of the particles in contrast to conventional microgels with the densest part in the core. The underlying explanation for this outcome are the transfer reactions induced by the initiator radicals, which create active centers on the polymer backbone at the particle surface. These active sites react further to cross-links to form a "skin" layer on top of the particles. After the significant non-cross-linked polymer fraction dissolves to continuous phase when the gel particles are let to swell, vesicle-like PNIPAM shells are obtained.

Instrumental to these discoveries was the development of non-stirred small-scale test tube polymerization method, in which 6 to 10 1 ml batches can be polymerized simultaneously at a well-regulated reaction temperature. It was found out that this highly reproducible process produces PNIPAM particles of narrow size distribution. An order of magnitude higher throughput in comparison to conventional single batch setup enabled rapid experimentation, the high reproducibility being a prerequisite for the discovery of the power law behavior of the final particle volume.

Rapid particle synthesis also requires efficient analysis methods. A program was written for a multi-angle cumulant analysis of dynamic light scattering data, which enabled processing of hundreds of measurement files in a matter of minutes.

More notably, a MATLAB program was developed for analysis of static scattering data. The modular, object oriented design allows for rapid and easy addition of new scattering models as well as scripting to fit large numbers of data files. This was crucial e.g. in the case of SANS study in Chapter 6, where approximately 15000 scattering patterns had to be fitted in an automatic manner.

Concrete and fundamental progress was achieved in this work in respect to understanding reaction and particle formation mechanism in precipitation polymerization of NIPAM. Nevertheless, open questions and ambiguous aspects remain. One of these is the role of particles in the polymerization reaction: Even though the reaction starts in water phase as a radical solution polymerization, it is possible that at later stages when the particles have a significant size the locus of polymerization partially moves to the particle surface. Active centers on the particle surface could be realized either by adsorption of propagating globules or chains from the continuous phase, or by peroxide initiator induced transfer reactions. As the large particles repel each other and the mobility of the chains on the collapsed surface is likely significantly reduced, it is possible that long lived radicals exist on the particle surface. Such species should be readily detectable by electron paramagnetic resonance (EPR) spectroscopy, as demonstrated in earlier work on heterogeneous polymerization.^[8,9]

Further investigation is needed to elaborate the connection between polymer charge density (average initiator fragment concentration per repeating units) and the number density of resulting polymer particles when a solution of PNIPAM of certain charge density is heated above the PNIPAM LCST. In Chapter 5 the power laws for the final particle volume were derived based on the simplistic assumption that the particle number density in a batch is directly proportional to the surface charge density of single chain globules. The polymer charge density can be readily modulated by the kinetic parameters of the polymerization,^[1,2] and the effect on the particle number density can be investigated by methodology demonstrated by Chan et al.^[10]

The batches in this work were synthesized in ion exchanged water without additional surfactant. The effect of ionic strength and stabilizer concentration on the number of particles were not investigated in detail. The non-stirred small-scale synthesis method is however well suited to investigate these contributions and present a straightforward extension of the current work. High reproducibility of the small-scale synthesis likely makes it possible to collect high quality data sets on these fundamental aspects of colloid chemistry and physics so that the experiment can be compared to the theoretical framework, namely, the DLVO theory.

To summarize, precipitation polymerization is a highly dynamic system that combines features from homogenous and heterogeneous polymerization as well as aspects of colloidal stabilization. The ultimate understanding of this complex

process requires successful interconnection of the different facets through computer simulation. The experimental work presented in this thesis supports this goal by recognizing the important aspects of precipitation polymerization. These include the early reaction polymerization mechanism, surface charge density differences arising from the response of the system to reaction conditions, number of particles as the determining factor for the final particle size and role of persulfate initiator induced crosslinking on the particle properties and final particle size. This insight generally enlightens the inner workings of precipitation polymerization of thermosensitive polymers and facilitates the development of new particle architectures and industrial processes for stimuli-sensitive microgel particles.

Bibliography

- [1] P. J. Flory, *Principles of Polymer Chemistry*, Cornell University Press, 1953.
- [2] G. Odian, *Principles of Polymerization*, Wiley Interscience, 4th edn, 2004.
- [3] X. Wu, R. H. Pelton, A. E. Hamielec, D. R. Woods and W. McPhee, *Colloid and Polymer Science*, 1994, **272**, 467–477.
- [4] W. McPhee, K. C. Tam and R. Pelton, *Journal of Colloid and Interface Science*, 1993, **156**, 24–30.
- [5] J. Gao and B. J. Frisken, *Langmuir*, 2003, **19**, 5212–5216.
- [6] J. Gao and B. J. Frisken, *Langmuir*, 2003, **19**, 5217–5222.
- [7] J. Gao and B. J. Frisken, *Langmuir*, 2005, **21**, 545–551.
- [8] M. Ueda, S. Shouji, T. Ogata, M. Kamachi and C. U. Pittman, *Macromolecules*, 1984, **17**, 2800–2804.
- [9] T. Sato, J. Miyamoto and T. Otsu, *Journal of Polymer Science: Polymer Chemistry Edition*, 1984, **22**, 3921–3932.
- [10] K. Chan, R. Pelton and J. Zhang, *Langmuir*, 1999, **15**, 4018–4020.

A. Symbols and abbreviations

	Explanation
$\ \cdot\ _2$	Vector 2-norm
APS	Ammonium persulfate
b	Scattering length
b_k	Kuhn length
BIS	N,N'-methylenebisacrylamide
CTAB	Cetyl trimethyl ammonium bromide
$E_{\bar{X}}$	Composite activation energy of kinetic chain length
$[I]_0$	Initial initiator concentration in the batch
LCST	Lower critical solution temperature
$[M]_0$	Initial monomer concentration in the batch
NIPAM	<i>N</i> -isopropylacrylamide
ν	Kinetic chain length
ν_e	Excluded volume
\mathbf{k}	Incident radiation wavevector
k_d	Rate constant of initiator dissociation
k_p	Rate constant of propagation
\mathbf{k}_s	Scattered radiation wavevector
KPS	Potassium persulfate
k_t	Rate constant of termination
λ	Regularization parameter
λ_0	Wavelength of radiation in vacuum
n_0	Refractive index of a dispersion
n_p	Number of particles
$P(q)$	Form factor
PNIPAM	Poly(<i>N</i> -isopropylacrylamide)
PNIPMAM	Poly(<i>N</i> -isopropylmethacrylamide)
PVCL	Poly(<i>N</i> -vinylcaprolactam)
\mathbf{q}	Scattering vector
R	Gas constant
R	Radius
R_g	Radius of gyration
R_h	Hydrodynamic radius
R_p	Propagation rate
ρ_p	Number density of particles
$S(q)$	Structure factor
SDS	Sodium dodecyl sulfate
σ_s	Particle fuzziness parameter
T	Temperature
VPTT	Volume phase transition temperature
V_p	Volume of the polymer particle in the collapsed state
V_M	Volume of network polymerized of 1 mol of monomer

B. Program FitIt!

B.1 General description

MATLAB program FitIt! was written for fitting static scattering data. The program requires MATLAB R2014b and newer as FitIt! heavily relies on the new object oriented graphics system introduced in R2014b. Figure B.1 shows the graphical user interface (GUI) of FitIt! The GUI projects the model parameters on the left; any changes to the parameters are instantaneously reflected to the predicted scattering pattern in the middle pane. Certain general model parameters, such as particle size distribution, background scattering and cuvette backreflection for static light scattering can be toggled on or off independently of the principal scattering model describing the geometry of the scatterers. Useful visual feedback, such as the contrast density profile of spherical geometries and the particle radius distribution function are provided on the right hand side of the GUI.

The program implements instrument resolution function relevant to small-angle scattering data. Global fitting of scattering patterns of the same sample but different resolution parameters is possible. This feature was used in Chapter 7, where the microgel samples were measured with different laser wavelengths to increase the number of data points and expand the q range.

Furthermore, the program features loading of large number of independent data sets and automatic fitting, accessed through a separate GUI window. This functionality was crucial for the results presented in Chapter 6, where *in situ* SANS measurements resulted in approximately 15000 separate datasets, which all had to be fitted with the same model. Due to sheer amount of data the GUI option was not used but specific scripts were written to handle loading, saving and fitting of the datasets using the flexible framework provided by the program.

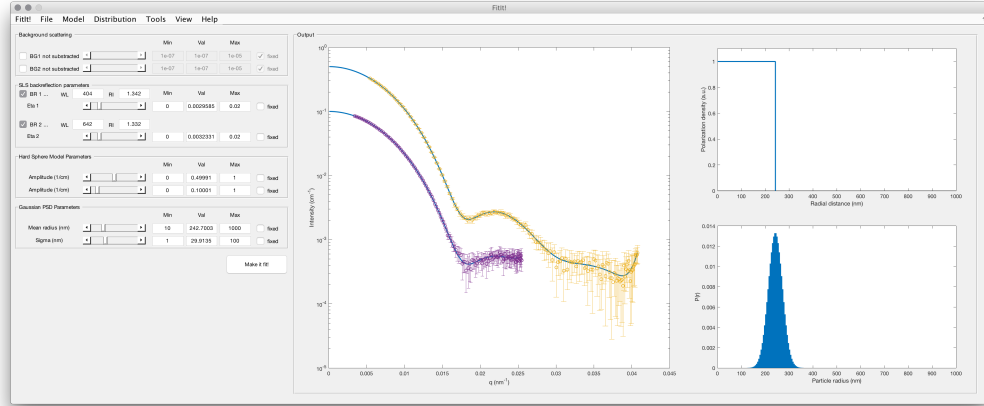


Figure B.1: Main window of MATLAB program FitIt!

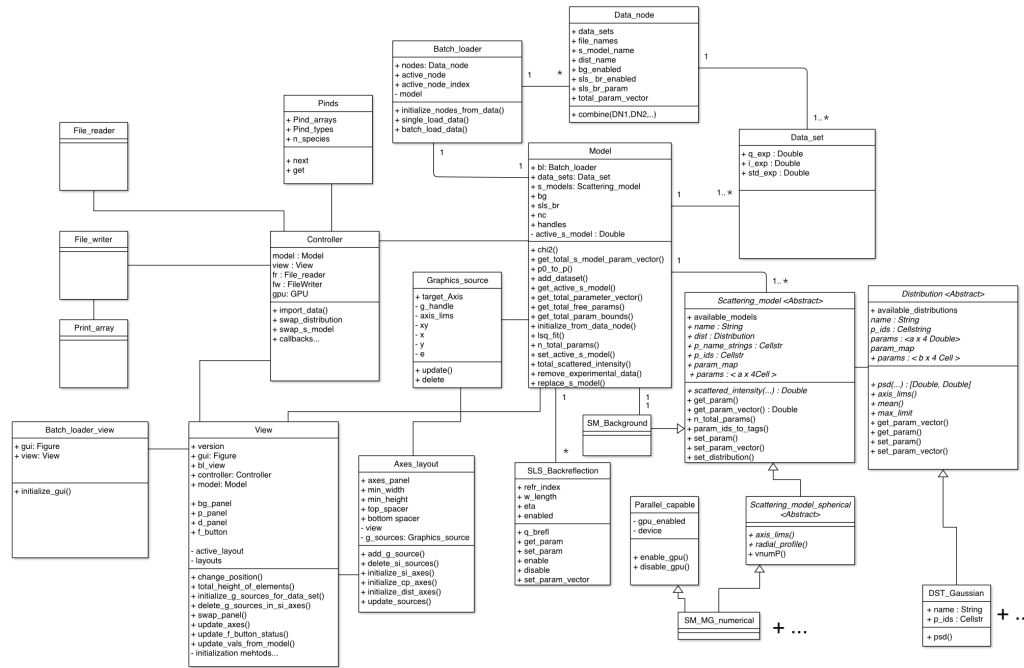


Figure B.2: UML (unified modelling language) schematic of FitIt! class structure.

B.2 Program structure

The program has a modular, object oriented design, which allows for easy modification and expansion of features. The basic structure is based on model-view-controller (MVC) scheme. Class diagram depicting the program structure is presented in Figure B.2. Special emphasis was laid on easy addition of new scattering models, which can be included using the provided abstract type interface. In practice this means implementing the abstract class *Scattering_model* or the more specific *Scattering_model_spherical* for spherically symmetric particles. For particle size distributions the abstract class *Distribution* has to be implemented. The abstract type interface makes sure that the models and distributions implement functionality necessary to be compatible with the larger FitIt! framework.

B.3 Form factors relevant to microgels

A good reference for different approaches to analysis of scattering data is provided by Pedersen.^[1] In simple terms, for a collection of dispersed particles, one can either attempt a Fourier inversion of the scattering pattern to obtain the pair-distance distribution function, which often exhibits distinguishable features specific to certain geometries,^[2] or, try to model the scattering pattern with an analytical solution to certain geometries.

Program FitIt! emphasizes the latter approach, even though it is fully possible to implement more general inversion methods to the program. The full expression for the scattered intensity has been given at multiple points throughout this work in Chapters 3, 6 and 7; this listing contains two examples of form factors relevant to microgel particles implemented by FitIt!

Homogeneous sphere form factor is sufficient to describe collapsed microgel particles

$$P(q) = \left[\frac{3(\sin(qR) - qR\cos(qR))}{(qR)^3} \right]^2 \quad (\text{B.1})$$

where q is the magnitude of the scattering vector and R is the radius of the sphere.

Fuzzy sphere structure is applicable to N,N' -methylenebisacrylamide crosslinked fuzzy particles.^[3] The radial profile of fuzzy sphere is depicted in Figure B.3, and mathematically given by

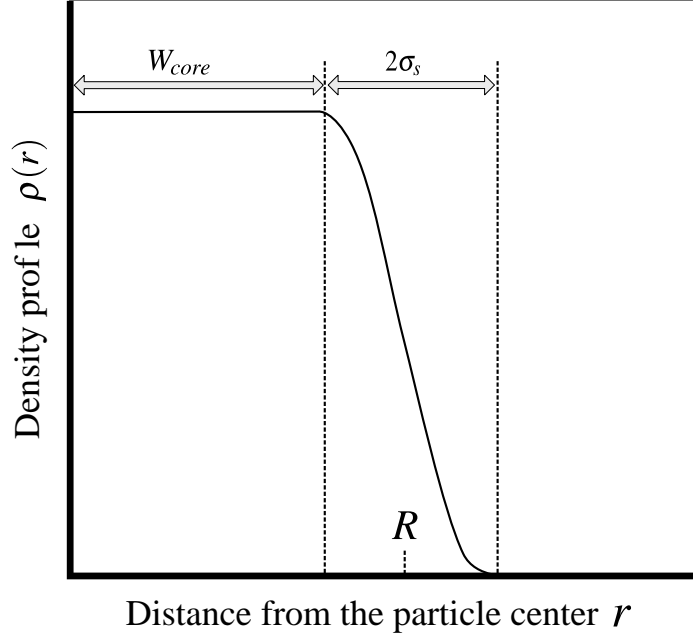


Figure B.3: Density profile of a fuzzy sphere particle. W_{core} denotes the width of the constant density core, $2\sigma_s$ defines the width of the fuzzy surface, and R is the overall size parameter used in Equations B.2 and B.3.

$$\rho(r) = 1 \quad r \leq (R - \sigma_s) \quad (\text{B.2a})$$

$$\rho(r) = 1 - \frac{1}{2} \frac{[(r - R) + \sigma_s]^2}{\sigma_s^2} \quad (R - \sigma_s) < r \leq R \quad (\text{B.2b})$$

$$\rho(r) = \frac{1}{2} \frac{[(R - r) + \sigma_s]^2}{\sigma_s^2} \quad R < r \leq (R + \sigma_s) \quad (\text{B.2c})$$

$$\rho(r) = 0 \quad (R + \sigma_s) < r \quad (\text{B.2d})$$

The Fourier transformation of the particle density profile is given by

$$\begin{aligned}
\Phi = & \frac{1}{V_n} \left[\left(\frac{R}{\sigma_s^2} + \frac{1}{\sigma_s} \right) \frac{\cos[q(R + \sigma_s)]}{q^4} \right. \\
& + \left(\frac{R}{\sigma_s^2} - \frac{1}{\sigma_s} \right) \frac{\cos[q(R - \sigma_s)]}{q^4} - \frac{3 \sin[q(R + \sigma_s)]}{q^5 \sigma_s^2} \\
& \left. - \frac{3 \sin[q(R - \sigma_s)]}{q^5 \sigma_s^2} - \frac{2R \cos(qR)}{q^4 \sigma_s^2} + \frac{6 \sin(qR)}{q^5 \sigma_s^2} \right]
\end{aligned} \tag{B.3}$$

with the normalization factor

$$V_n = \frac{R^3}{3} + \frac{R\sigma_s^2}{6} \tag{B.4}$$

Note that in Berndt et al.^[3] there is a misprint in Eq. B.3. Finally, the form factor of a fuzzy sphere is the square of the Fourier transform of the particle density profile

$$P(q) = [\Phi(q, R, \sigma_s)]^2 \tag{B.5}$$

Bibliography

- [1] J. S. Pedersen, *Advances in Colloid and Interface Science*, 1997, **70**, 171–210.
- [2] O. Glatter, *Neutrons, X-rays and Light: Scattering Methods Applied to Soft Condensed Matter*, Amsterdam: North Holland Delta Series, 2002.
- [3] I. Berndt, J. S. Pedersen, P. Lindner and W. Richtering, *Langmuir*, 2006, **22**, 459–468.

Acknowledgement

I would like to thank several people who have helped and supported me during the project.

First and foremost I want to thank Walter for the guidance, supervision and discussion, as well as freedom and facilities to carry out the work. His insight and contributions have greatly improved the end result.

Second, I want to thank Sara for her invaluable ability to put things in perspective and occasional necessary pushes to keep the train rolling. Her presence has put my soul in peace.

I would like to thank Andrij for fruitful discussion and productive collaboration. Special thanks to Dominik for willingness to discuss tough problems; his support with the 2015 MCP paper was crucial to remove mental blocks and get the manuscript finished.

Aurel has been a great help with KWS-2 related challenges; we would have never been able to finish the demanding experiments and subsequent data analysis without his help. Ahmed's competence with all things AFM was inspiring to look at, and also the deciding factor for getting the 2016 SM paper accepted.

I greatly enjoyed discussions with Felix, Steffi, Thomas E. & Dima and Larisa, who always had sound and interesting perspectives that I would not have thought of/believed by myself.

I would like to thank my colleagues Arjan, Adonis, Camille, Stefan, Olga and Thomas L. & comrades for the nice atmosphere at the group as well as providing feedback and keeping me at check in certain situations. Pascal and Captain Corny deserve a special mention for all the computer related fun and discussion of theoretical and computational aspects of the work. Janine I would like to thank for her great help in getting started and demonstrating the right attitude to get things done.

Special thanks goes to my motivated, eager and hard-working students Helmi and Monia. Their careful work made it possible to publish several papers. Thanks to Thomas L., Samina, Corinna for the help with translating the abstract to German.

Julian, Michael and Andrea have been great help with accomplishing demanding work and demonstrated tough character under difficult circumstances. The other Andrea I would like to thank for tips on good Italian coffee.

Many thanks to my family in Finland for continuous support and the prerequisites necessary to accomplish this work.

Publications

Virtanen, O. L. J., & Richtering, W. (2014) Kinetics and particle size control in non-stirred precipitation polymerization of N-isopropylacrylamide. *Colloid and Polymer Science*, 292(8), 1743–1756.

<http://doi.org/10.1007/s00396-014-3208-x>

Virtanen, O. L. J., Ala-Mutka, H. M., & Richtering, W. (2015) Can the Reaction Mechanism of Radical Solution Polymerization Explain the Microgel Final Particle Volume in Precipitation Polymerization of N-Isopropylacryl-amide? *Macromolecular Chemistry and Physics*, 216(13), 1431–1440.

<http://doi.org/10.1002/macp.201500118>

Virtanen, O. L. J., Mourran, A., Pinard, P. T., & Richtering, W. (2016) Persulfate initiated ultra-low cross-linked poly (N-isopropylacrylamide) microgels possess an unusual inverted cross-linking structure. *Soft Matter*, 12(12), 3919 –3928.

<http://doi.org/10.1039/C6SM00140H>

Virtanen, O. L. J., Brugnoni, M., Kather, M., Pich, A., & Richtering, W. (2016) The next step in precipitation polymerization of N-isopropylacrylamide: Particle number density modulation by monochain globule surface charge control. *Polymer Chemistry*. <http://doi.org/DOI: 10.1039/c6py01195k>

Virtanen, O. L. J., Purohit, A., Brugnoni, M., Wöll, D. & Richtering, W. (2016) Synthesis and fluorescence tracking of highly uniform poly(N-iso-propylacrylamide) microgels. *Journal of Visualized Experiments*, accepted

Conference contributions

Quantification of Precipitation Polymerization of *N*-isopropylacrylamide by Scattering Methods. Poster presentation, Biennial Meeting of the German Colloid Society, 2013.

Manipulation of the poly(*N*-isopropylacrylamide) microgel particle size by temperature-programmed synthesis. Oral presentation, European Student Colloid Conference, 2013.

Insights into the particle formation mechanism in precipitation polymerization of *N*-isopropylacrylamide. Oral presentation, European Polymer Federation Confer-

ence 2015.

Insights into particle nucleation mechanism and late reaction multiplet formation in precipitation polymerization of *N*-isopropylacrylamide. Oral presentation, Conference of the European Colloid and Interface Society, 2015.

Supervised students

René Büttgen, Controlled synthesis of poly(*N*-isopropylacrylamide) and poly(*N,N*-diethylacrylamide) homopolymers and copolymer. Bachelor thesis, 2013.

Helmi-Maria Ala-Mutka, Effect of cross-linker and initiator concentration on the final particle volume in non-stirred precipitation polymerization of *N*-isopropylacrylamide. Research project, 2015.

Monia Brugnoli, Effect of chain transfer and inhibition on the final particle volume of poly(*N*-isopropylacrylamide) microgels in the collapsed state. Research project, 2015.

Monia Brugnoli, Number density and structure of particles in non-stirred precipitation polymerization of *N*-isopropylacrylamide. Student assistant, six months, 2015.

Co-supervisor:

Monia Brugnoli, Synthesis and characterization of thermoresponsive core-shell, core-double-shell and hollow microgels. Master's thesis, 2016.

Courses

Fundamentals of Colloids and Interfaces by the European Colloid and Interface Society and European Cooperation in Science and Technology
June 10th 2013, Potsdam-Golm, Germany

5th European Short Course on Time-resolved Microscopy and Correlation Spectroscopy by PicoQuant GmbH
February 10 - 21, 2013, Berlin, Germany

12th European Summer School on Scattering Methods Applied to Soft Condensed
Matter by Institut Laue-Langevin
May 16 - 23, 2014, Bombannes, France

Procter & Gamble R&D Ph.D. Seminar 2015
April 19 - 23, 2015, Brussels, Belgium

Curriculum Vitae

Personal Data

Name	Otto Lauri Johannes Virtanen
Date of birth	18.12.1987
Nationality	Finnish
Family status	Single

Education

2012 - present	PhD candidate RWTH Aachen University, Germany
2011 - 2012	M.Sc. Polymer chemistry University of Helsinki, Finland
2007 - 2011	B.Sc. Chemistry (Minor: Computer science) University of Helsinki, Finland
2006	Finnish matriculation examination Kuopion Lyseon lukio